ABSTRACT

Title of dissertation: GUIDED MIGRATION AND COLLECTIVE BEHAVIOR: CELL DYNAMICS DURING CANCER PROGRESSION

Rachel Mary Lee, Doctor of Philosophy, 2016

Dissertation directed by: Professor Wolfgang Losert
Department of Physics

This dissertation focuses on gaining understanding of cell migration and collective behavior through a combination of experiment, analysis, and modeling techniques. Cell migration is a ubiquitous process that plays an important role during embryonic development and wound healing as well as in diseases like cancer, which is a particular focus of this work. As cancer cells become increasingly malignant, they acquire the ability to migrate away from the primary tumor and spread throughout the body to form metastatic tumors. During this process, changes in gene expression and the surrounding tumor environment can lead to changes in cell migration characteristics. In this thesis, I analyze how cells are guided by the texture of their environment and how cells cooperate with their neighbors to move collectively. The emergent properties of collectively moving groups are a particular focus of this work as collective cell dynamics are known to change in diseases such as cancer.

The internal machinery for cell migration involves polymerization of the actin cytoskeleton to create protrusions that—in coordination with retraction of the rear

of the cell—lead to cell motion. This actin machinery has been previously shown to respond to the topography of the surrounding surface, leading to guided migration of amoeboid cells. Here we show that epithelial cells on nanoscale ridge structures also show changes in the morphology of their cytoskeletons; actin is found to align with the ridge structures. The migration of the cells is also guided preferentially along the ridge length. These ridge structures are on length scales similar to those found in tumor microenvironments and as such provide a system for studying the response of the cells' internal migration machinery to physiologically relevant topographical cues.

In addition to sensing surface topography, individual cells can also be influenced by the pushing and pulling of neighboring cells. The emergent properties of collectively migrating cells show interesting dynamics and are relevant for cancer progression, but have been less studied than the motion of individual cells. We use Particle Image Velocimetry (PIV) to extract the motion of a collectively migrating cell sheet from time lapse images. The resulting flow fields allow us to analyze collective behavior over multiple length and time scales.

To analyze the connection between individual cell properties and collective migration behavior, we compare experimental flow fields with the migration of simulated cell groups. Our collective migration metrics allow for a quantitative comparison between experimental and simulated results. This comparison shows that tissue-scale decreases in collective behavior can result from changes in individual cell activity without the need to postulate the existence of subpopulations of leader cells or global gradients.

In addition to tissue-scale trends in collective behavior, the migration of cell groups includes localized dynamic features such as cell rearrangements. An individual cell may smoothly follow the motion of its neighbors (affine motion) or move in a more individualistic manner (non-affine motion). By decomposing individual motion into both affine and non-affine components, we measure cell rearrangements within a collective sheet. Finally, finite-time Lyapunov exponent (FTLE) values capture the stretching of the flow field and reflect its chaotic character.

Applying collective migration analysis techniques to experimental data on both malignant and non-malignant human breast epithelial cells reveals differences in collective behavior that are not found from analyzing migration speeds alone. Non-malignant cells show increased cooperative motion on long time scales whereas malignant cells remain uncooperative as time progresses. Combining multiple analysis techniques also shows that these two cell types differ in their response to a perturbation of cell-cell adhesion through the molecule E-cadherin. Non-malignant MCF10A cells use E-cadherin for short time coordination of collective motion, yet even with decreased E-cadherin expression, the cells remain coordinated over long time scales. In contrast, the migration behavior of malignant and invasive MCF10CA1a cells, which already shows decreased collective dynamics on both time scales, is insensitive to the change in E-cadherin expression.

GUIDED MIGRATION AND COLLECTIVE BEHAVIOR: CELL DYNAMICS DURING CANCER PROGRESSION

by

Rachel Mary Lee

Dissertation submitted to the Faculty of the Graduate School of the
University of Maryland, College Park in partial fulfillment
of the requirements for the degree of
Doctor of Philosophy
2016

Advisory Committee:
Professor Wolfgang Losert, Chair
Professor Jose Helim Aranda-Espinoza
Professor John T. Fourkas, Dean's Representative
Professor Michelle Girvan
Adjunct Professor Carole A. Parent

Acknowledgments

I would like to express my thanks to my advisor, Dr. Wolfgang Losert, who first showed me movies of migrating cells and got me hooked on this project. I am thankful for all the opportunities he has given me to pursue interesting projects, to attend exciting conferences, and to grow as a researcher. I would also like to thank Dr. Carole Parent for letting a physics student into her lab. I have appreciated the hands-on opportunity to learn about cell biology. I am grateful to the other members of my committee, Drs. Jose Helim Aranda-Espinoza, John Fourkas, and Michelle Girvan for their feedback and guidance.

For the past three years, my work has been supported by the Metro Washington Chapter of the Achievement Rewards for College Scientists (ARCS) Foundation. I appreciate the opportunities I have had to meet their members and other students in the program. I am especially thankful to Jim and Cheryl MacGuidwin of the JCM Foundation for sponsoring my fellowship and for taking an interest in my work.

I would like to thank everyone in the Losert lab. I would especially like to thank Megan Driscoll, Matt Harrington, and Lenny Campanello for making MATLAB boot camp fun every year. Peter Kordell helped me get oriented in the lab and contributed to our analysis code. Ava Omidvar kept the lab running and was always willing to lend a hand. I appreciate the advice I received from Kerstin Nordstrom and Mitch Mailman. Thank you to Can Guven and Josh Parker for always asking me difficult questions. My discussions with Chenlu Wang and Matt Hourwitz always helped me clarify ideas. I appreciate both the serious conversations and the laughter

I have shared with everyone in the lab.

I owe many thanks to everyone in the Parent lab at the National Institutes of Health; they gave me a second lab to call home during graduate school. I would especially like to thank Michael Weiger for letting me ask him constant questions and for teaching me the basics of cell culture. I always enjoyed the conversations I had with Paul Kriebel, Ritankar Majumdar, and Philippe Afonso. Christina Stuelten created some of the cell lines I worked with in this thesis and shared cell culture work with me. I would also like to thank Alex Szatmary for asking good questions and for his appreciation of perceptual color maps.

I wish to thank Drs. John and Gay Stewart, who helped convince me to first take an extra physics class as an elective, to then declare physics as a second major, and to eventually attend graduate school in physics. I would also like to thank the faculty in the University of Arkansas Chemical Engineering department for giving me a strong foundation in problem-solving.

My classmates Jack Hellerstedt, John Biddle, and Josh Wood were always willing to argue with me while studying for our qualifying exams. Their friendship remained a source of support throughout graduate school. The Women in Physics group at the University of Maryland was also a source of friendship and support.

I am grateful to my family for their continual support. The phone calls from my parents, Dan and Cindy Lee, to ask me how my cells were doing always cheered me up, even when the cells were not doing so well. I also owe many thanks to Johnathan Conley for his support, for making me leave the lab sometimes, and for his never-ending patience with my grammar questions while I was writing this thesis.

Table of Contents

List of Tables vii

List of Figures viii

1 Introduction 1

2 Background 6
2.1 Mechanisms of Cell Migration 6
2.2 Migration and Forces during Cancer Progression 8
2.3 Cell Interactions with Physical Properties of the Environment 12
2.4 Dynamics of Collective Cell Migration 14
2.5 Physical Models of Collective Migration 17
2.6 Quantifying Collective Migration Dynamics 22
2.7 Cell-Cell Adhesion Forces during Collective Dynamics 28

3 Guidance of Individual Cells by the Underlying Surface 31
3.1 Overview 31
3.2 Background 32
3.3 Results 34
3.3.1 Epithelial Cells Exhibit Microthigmotaxis on Nanoridges . . . 34
3.3.2 Cells Show Persistent Elongated Morphology on the Nanoridges 36
3.3.3 Nanoridges Promote Esotaxis 37
3.4 Discussion 38
3.5 Materials and Methods 40
3.5.1 Cell Preparation and Imaging 40
3.5.2 Surface Fabrication 41
3.5.3 Measuring Microthigmotaxis 41

4 Guidance of Individual Cells by their Neighbors 43
4.1 Overview 43
4.2 Background 44
4.3 Results 46
4.4 Discussion 55

4.5 Materials and Methods . . . 57
4.5.1 MCF10A Data Set . . . 57
4.5.2 Migration Analysis . . . 57
4.5.3 Simulations . . . 59

5 Metrics for Understanding Collective Migration 64
5.1 Overview . . . 64
5.2 Background . . . 65
5.3 Results . . . 68
5.3.1 Finite-time Lyapunov Exponents . . . 70
5.3.2 Non-affine Motion . . . 73
5.3.3 Density Effects . . . 74
5.4 Discussion . . . 79
5.5 Materials and Methods . . . 81
5.5.1 Cell Culture and Microscopy . . . 81
5.5.2 Image Analysis . . . 82
5.5.3 Field of View Reconstruction . . . 83
5.5.4 Finite-time Lyapunov Exponents . . . 84
5.5.5 Non-affine Motion . . . 85

6 Cell-Cell Adhesion and Long Time-Scale Collective Dynamics 86
6.1 Overview . . . 86
6.2 Background . . . 87
6.3 Results . . . 89
6.3.1 E-cadherin and Collective Dynamics . . . 95
6.3.1.1 M1 E-cadherin shRNA Cell Lines . . . 99
6.3.1.2 M4 E-cadherin shRNA Cell Lines . . . 102
6.4 Discussion . . . 104
6.5 Materials and Methods . . . 110
6.5.1 Cell Culture . . . 110
6.5.2 Western Blots . . . 111
6.5.3 Immunofluorescence . . . 111
6.5.4 Migration Assay and Microscopy . . . 112
6.5.5 Image Analysis: Particle Image Velocimetry . . . 114
6.5.6 Migration Analysis . . . 115

7 Outlook 119
7.1 Analysis Applications . . . 120
7.2 Connecting Individual and Collective Migration . . . 123
7.2.1 Polarity . . . 123
7.2.2 Collective Migration and Contact Guidance . . . 125

A Particle Image Velocimetry Software Guide 128
A.1 Overview and Basic Use . . . 129
A.1.1 Running the Batch Script . . . 130
A.2 PIV Calculations . . . 132
A.3 PIV Filtering . . . 135
A.4 Edge Detection . . . 138
A.5 FTLE Calculations . . . 140
A.6 Interpreting the Filter Check Output . . . 140
A.7 Analysis Sections of the Batch Script . . . 141
A.7.1 Basic Analytics . . . 141
A.7.2 PIV Time Analytics . . . 146
A.7.3 FTLE Analytics . . . 146
A.7.4 Coarse Graining . . . 148
A.8 Other Analysis Scripts . . . 151
A.8.1 Distribution Figures . . . 151
A.8.2 Spatial Correlations . . . 153

Bibliography 155

List of Tables

4.1 Standard Value of Simulation Parameters 60

List of Figures

2.1 Actin-dependent Cell Crawling 7
2.2 Metastatic Progression 10
2.3 Collective Cancer Invasion 15
2.4 Modeling Perspectives in Collective Migration 19
2.5 Schematic Phase Diagrams of Jamming 20
2.6 Image Analysis Methods for Quantifying Collective Migration 23
2.7 Schematic of Traction Force Microscopy 26
2.8 Schematic of Non-Affine Motion 27

3.1 Microthigmotaxis of Epithelial MCF10A Cells on Nanoridge Surfaces 35
3.2 Aspect Ratio of Cells on Nanoridge Surfaces 36
3.3 Actin Morphology on Ridge Surfaces 37
3.4 Actin Dynamics on Ridge Surfaces 38

4.1 Experimental Data on Large Scale Migration Patterns 47
4.2 Simulation Model and Leader Cells 49
4.3 Migration Patterns and Proliferation Rate 50
4.4 Disassociation of the Cell Monolayer at Low Proliferation Rate 51
4.5 Migration Patterns and Wake Rate 52
4.6 Migration Patterns and Velocity-Motility Coupling 53
4.7 Correlated Migration Behavior 54
4.8 Comparison of Monolayer Growth in Experiments and Simulations . . 63
4.9 Simulation Time Scale and Monolayer Size 63

5.1 Migration Assay and Image Analysis 69
5.2 Comparison of Tracking and PIV Speeds 71
5.3 FTLE Values versus Deformation Time 72
5.4 FTLE Distributions Across Cell Experiments 73
5.5 Cell Rearrangements Measured Through D^2_{min} 75
5.6 Migration Trends versus Radial Location 77
5.7 Density Effects in Speed and Cell Rearrangements 78

6.1 Migration Comparison between M1 and M4 Cells 90

6.2 Angular and FTLE Distributions for M1 and M4 Cells 92
6.3 Migration Trends Over Time for M1 and M4 Cells 94
6.4 Characteristic Time Scales of Flow Fluctuations in M1 and M4 Cells 95
6.5 Spatial Correlations for M1 and M4 Cells 96
6.6 Comparison between M1 Cells and shRNA Control Cells 97
6.7 Comparison between M4 Cells and shRNA Control Cells 98
6.8 Migration Comparison for M1 E-cadherin shRNA Cells 99
6.9 Angle and FTLE Distributions for M1 E-cadherin shRNA Cells . . . 100
6.10 Migration Analysis of M1 E-cadherin shRNA Cells 101
6.11 Characteristic time scales for M1 E-cadherin shRNA cells 102
6.12 Migration Comparison for M4 E-cadherin shRNA Cells 103
6.13 Angle and FTLE Distributions for M4 E-cadherin shRNA Cells . . . 104
6.14 Migration Analysis of M4 E-cadherin shRNA Cells 105
6.15 Characteristic Time Scales for M4 E-cadherin shRNA Cells 106
6.16 Western Blot Showing E-cadherin Knockdown Cell Lines 112
6.17 Immunofluorescence Images of E-cadherin in M1 Cells 113
6.18 Immunofluorescence Images of E-cadherin in M4 Cells 113
6.19 Edge Detection Method and Analysis 115
6.20 Variability in Spatial Correlations for M1 and M4 Cells 118

7.1 Preliminary Data on Edge Dynamics 122
7.2 Preliminary Data on Corneal Epithelium Collective Migration 122
7.3 Preliminary Data on Collective Migration Contact Guidance 126

A.1 Plotting PIV flow fields 137
A.2 Edge Detection and PIV Filtering Verification 139
A.3 Example Output of the PIV Analytics Code 144
A.4 Example Output of the PIV Time Analytics Code 147
A.5 Example Output of the FTLE Analytics Code 149
A.6 Example Output of the Coarse Graining Code 150
A.7 Example Output of Distribution Batch Scripts 152
A.8 Example Output of Correlation Batch Script 154

Chapter 1: Introduction

From single-celled organisms migrating along the forest floor to groups of cells moving to their proper position during embryonic development, cell migration is essential for many biological systems. Cell migration also plays an important role during cancer, which is a complex set of diseases. As research into treatment of cancer has progressed, understanding the underlying mechanisms of these diseases has quickly become a multidisciplinary problem requiring combined clinical, biological, and physical approaches.

As a cancer progresses, its growth and ability to spread throughout the body are dependent on cell migration. The growth of secondary tumors in new regions of the body, known as metastasis, is often the cause of death for cancer patients [1, 2]. Indeed, when cancers are detected early and consist of only a primary tumor location, a cure is often possible. Understanding migration is thus important for the clinical problem of treating patients when localized treatments such as surgery or radiation are no longer effective options.

During the process of metastasis, cells undergo genetic and biochemical changes that allow them to migrate and grow in abnormal locations of the body. There has been much research into the molecular mechanisms of metastasis [2], but there is a

corresponding physical problem of understanding cell-scale migration behavior over time, which will be of particular interest in this thesis. Cell-scale dynamics can be interestingly compared to dynamic systems, such as flowing fluids, that have been frequently studied in the physical sciences. Combining the physical sciences perspective with the vast body of clinical and biological research on cancer is likely to help fight the disease. Indeed, there is a growing recognition that physical science tools and ideas can make valuable contributions to cancer studies [3–5].

Cell migration also provides an interesting experimental system for physics research on active dynamics. Although the migration of cells can be compared to systems such as fluid flows [6], cell behavior often shows distinct differences from inanimate systems. The emergent behavior of collective cell groups is particularly interesting; it is non-trivial to predict the dynamical behavior of migrating cell sheets or clusters from the properties of individual cells. This thesis will discuss the properties of individual cells that can guide cell migration and the dynamical features that are found when cells migrate collectively. A discussion of previous work linking the biology of cell migration to the physical properties of cells and their environment is provided in Chapter 2.

During cancer progression, cells leaving the primary tumor encounter a variety of environments. To move forward, cells must generate traction forces on the local environment. As will be further discussed in Chapter 2, many studies have shown that physical properties of the substrate influence cell migration. Surface stiffness has been shown to guide motion in inanimate systems and water droplets have been seen to move toward softer substrates [7]. Multiple cell types, however, have shown a

preference for stiff substrates [8,9], which suggests that further physical mechanisms are at play in their active migration. Chapter 3 will discuss another physical feature of the environment—the topography of the surface on which cells migrate. There are indications that the structure of collagen around a tumor plays a clinical role in the migration and spread of tumor cells [10, 11]. The work discussed in Chapter 3 shows that simple ridge structures with features on the scale of collagen fibers are capable of guiding cell migration in human breast epithelial cells. Chapter 3 will also discuss guidance of the internal actin machinery that propels cell movement.

Although physical properties of the substrate influence a cell's behavior, the migration environment also includes surrounding cells that exert forces that affect migration dynamics. A particularly interesting system is the case in which multiple cells migrate together as a sheet or cluster. This form of collective migration has been observed in mice models of cancer progression [12, 13], and recent studies have suggested that cell groups may be more dangerous to cancer patients than are individually migrating cells [14,15]. We have developed tools that allow us to extract motion information from time lapse images to investigate the dynamics of migrating cell sheets; our implementation of one such technique, particle image velocimetry (PIV), is discussed in Appendix A.

In Chapter 4, we compare experimental data on migrating cell sheets to a previously published model of cell groups [16]. Using this comparison, we investigate the emergent behavior that results from many individual cells migrating together as a sheet. We find that large-scale migration behaviors that encompass hundreds or thousands of cells can be related to changes in individual cell properties. These

changes do not require the existence of a subpopulation of leader cells or large scale features. In Chapter 4, we find that the activity of cells and their individual polarity strength can influence the collective properties of the migrating group, which provides direction for future studies on this system.

We further explore the emergent behavior of cell sheets by comparing experimental cell sheet data to previous research on inanimate systems. In Chapter 5, we compare cell sheets to granular systems to extract information about individual cell rearrangements within the sheet. We find increases in rearrangements at high cell densities, in contrast to the expected behavior of inanimate systems. Again, this result suggests interesting active behavior in the cell sheet system. In Chapter 5, we also make a comparison between the motion of the entire sheet and a flowing fluid by calculating finite-time Lyapunov exponent (FTLE) values to explore the chaotic character of the cells' collective dynamics. This technique allowed us to quantify differences in migration behavior near the edge of the cell sheet.

Collective migration in many systems relies on the ability of cells to adhere to their surroundings and neighboring cells. Misregulation of cell-cell adhesion has been implicated in some forms of cancer, which has increased research interest in its role during cell migration [17, 18]. Using the techniques developed in the previous chapters, Chapter 6 describes the difference in sheet migration between a non-malignant cell type which is unable to form tumors in mice and a malignant cell type which is able to form tumors and can spread to the lungs of mice. We find that the non-malignant cells are more cooperative than the malignant cells and that the non-malignant cells also show increasing collective behavior over time. We

then perturb E-cadherin, an important cell-cell adhesion molecule, and find that it regulates only part of the migration phenotype. Decreased E-cadherin expression decreases cooperativity on short time scales, but the non-malignant cells still show increasing coordination over time.

The tools we have developed for studying the dynamics of cell migration have the potential to be applied to other systems, such as studies on surface guidance during collective migration. In Chapter 7, I discuss the dynamical systems studied in this thesis and present an outlook on future studies of these migration models.

Chapter 2: Background

2.1 Mechanisms of Cell Migration

Cell migration is ubiquitous in biological systems. Single-celled amoebae must move towards food sources [19], whereas multicellular organisms use cell migration during development [20, 21] and wound healing [22]. Migration is also exhibited during immune responses [23] and in pathological conditions including cancer [24].

Although cells have a wide range of purposes and exist in a variety of environments, they often use similar mechanisms of migration. One of the most commonly studied forms of migration is actin-dependent crawling, which is illustrated in Figure 2.1 as it is described in [25]. In this form of migration, motility begins with an actin-based protrusion at the leading edge of the cell. This protrusion can then form new adhesions with the underlying substrate. The cell body is pulled forward through contractile forces based on actomyosin and finally the rear of the cell retracts, leading to the overall forward motion of the cell. Under certain environmental conditions, cells also migrate via additional mechanisms, such as blebbing [26] and directed water permeation [27].

Migration based on actin protrusions is of particular interest in this thesis, as it plays a role in the ability of cells to sense surfaces [28]. Actin forms a poly-

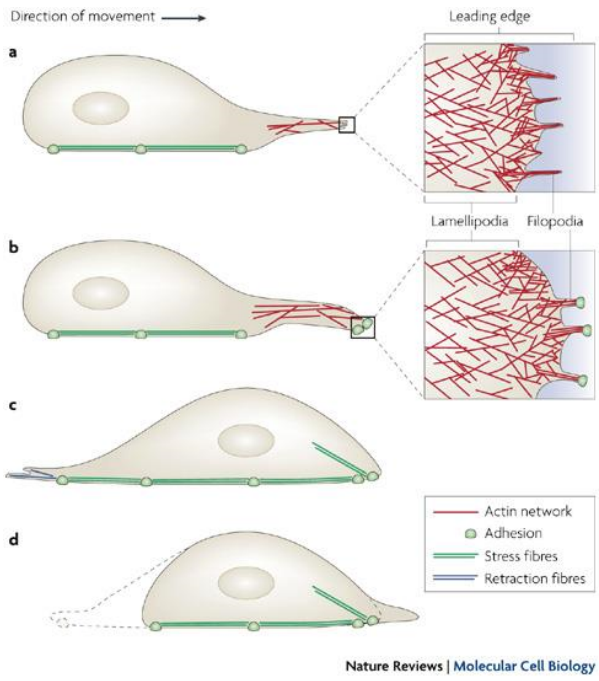

Figure 2.1: Actin-dependent cell crawling begins with a protrusion at the leading edge of the cell (a), which is followed by the creation of new adhesions with surface (b). Contractile forces at the rear of the cell move the nucleus and cell body forward (c) and adhesions at the rear disassemble, allowing the trailing edge to retract (d). (This figure was reproduced from [25] with a license from Nature Publishing Group.)

mer network that, along with microtubules and intermediate filaments, forms the cytoskeleton that controls the shape and movement of cells [29]. Actin polymerizes spontaneously into long, stable filaments that are polar due to the orientation of its subunits [30]. One end of the filaments, known as the barbed end, grows rapidly. Depending on interactions with surrounding factors, the barbed end can form a variety of larger structures, including parallel bundles of fibers in filopodia or branched networks associated with lamellipodia [25]. The growth of each actin filament produces piconewton forces that can push the cell front forward and facilitate

migration [30].

In addition to its role during crawling, actin is known to have a wide variety of dynamic behaviors, including traveling waves [31], as shown in Figure 2.1. The complex behavior of actin polymerization leads to a variety of cell-level dynamics, which will be a particular focus of this thesis. Actin flows have been shown to influence the persistence of cell migration [32] and guide cells along fibrous matrices [33]. Actin dynamics also play a role in the collective migration of many cells and have been shown to coordinate activities such as wound healing [34].

2.2 Migration and Forces during Cancer Progression

Cancer is a set of complex diseases that are predicted to lead to 595,690 fatalities in the United States during 2016, making it the country's second most common cause of death [1]. This set of diseases is associated with genetic instability that leads to cellular changes such as sustained proliferation signals and resistance to cell death [18]. The surrounding microenvironment also plays a role in these diseases, either through signals from surrounding cells [18] or, as is being increasingly recognized, through the physical properties of the tumor cell environment (discussed further in Section 2.3). Cell migration can be affected by all of these factors, and thus plays a role throughout the disease, including at the earlier stage of tumor growth [35]. Cell migration is most commonly discussed, however, at later stages of cancer progression, when the tumor cells spread throughout the body.

The process of a primary tumor spreading throughout the body, known as

metastasis, is illustrated in Figure 2.2. In this schematic, the process of metastasis is illustrated for an epithelial tissue tumor, known as a carcinoma. This type of tumor accounts for approximately 80% of life-threatening cancers [2] and begins with a mass of tumor cells growing in one location of the body. At some point in the growth of the tumor, a cell or a group of cells leaves the primary tumor to invade the surrounding healthy tissue. In addition to requiring cell migration, this step requires cells to interact with the cells of the surrounding tissue and possibly move past barriers such as the basement membrane. Cancer cells that migrate far enough to reach a blood vessel have the opportunity to squeeze into the vasculature (known as intravasation), where they can then circulate throughout the body. Cells that survive the circulation are then caught in a capillary bed or otherwise find a way to adhere to the side of a blood vessel. If the cells are then able to leave the circulatory system (known as extravasation), they can find their way to a new tissue location in the body, where they form what is known as a micrometastasis. If the cancer cells are able to survive and grow in this region, they will form a larger group of cells that will eventually become large enough to be clinically detectable, at which point this secondary location is known as a metastatic tumor [2].

The process of metastasis requires cells to be able to survive in multiple environments and to respond to varied chemical cues. Metastasis also subjects cancer cells to a variety of physical forces. Cells that are able to enter the blood stream must be able to survive unattached to a substrate, or they will undergo a form of cell death known as anoikis. The cells must also survive the shear stresses caused by blood flow, which can stress or kill the cells directly and can also make them

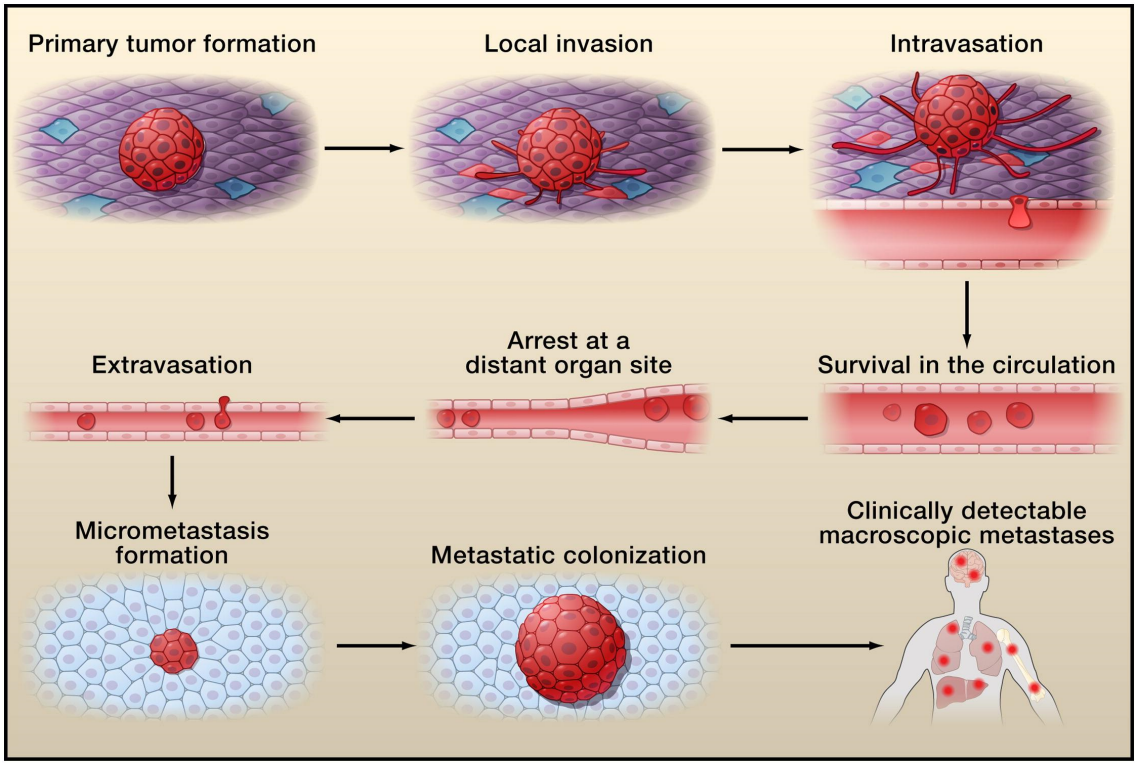

Figure 2.2: Cells from a primary tumor invade the locally surrounding tissue, enter the blood stream (intravasation), circulate throughout the body, leave the circulation (extravasation), survive in a new location (micrometastasis), and grow to form secondary tumors (metastatic colonization) during metastatic progression. (This figure was reproduced from [2] with a license from Elsevier.)

more susceptible to chemotherapeutic agents [36]. To survive and grow in a secondary location, cells must also thrive in a new environment that may vary from the primary tumor location, including changes in the behavior of surrounding cells and the physical stiffness of the environment. The steps to metastasis are difficult to survive and some estimates suggest that over 99.9% of those cells that leave the primary tumor do not succeed in metastatic colonization [2]. Yet, tumors that have spread are associated with decreased survival rates and are difficult to treat, making

the cells that do survive a clinically relevant problem [1, 2].

During the early stages of the metastatic process, cells must migrate away from the primary tumor location. Cells have been shown to adopt different migration behaviors to accomplish this task, including rounded amoeboid motion, elongated mesenchymal crawling, and multi-cell collective migration [13]. There has been much interest in how cells switch between these modes of migration, and in particular how cancers that begin in epithelial tissues (carcinomas) can become mesenchymal metastatic cells. This epithelial to mesenchymal transition (EMT) is characterized by both the expression of biomarkers and changes in the cells' shape and migration phenotypes [17]. Cells must also transition between epithelial and mesenchymal migration modes during development and wound healing. A commonly studied model system for EMT is the delamination and migration of neural crest cells during embryonic development, which displays many similarities to the transitions seen in cancer [21]. Modeling of the genetic networks that have been observed during development has suggested that cancer cells will indeed transition between epithelial and mesenchymal states, but will also exist in hybrid states that may give cancer cells additional advantages during the metastatic process [37]. Indeed, experimental studies have seen evidence for this phenotypic plasticity [38, 39]. For example, a squamous-cell carcinoma mouse model has shown that although EMT is used to leave the primary tumor, a mesenchymal to epithelial transition (MET) is used during the later stages of metastasis to allow the secondary tumor to retain epithelial characteristics during growth [40].

This thesis work focuses on the migration of human breast epithelial cells.

Understanding the mechanisms of migration and metastasis in breast cancer would provide clear clinical benefit. Between 2005 and 2011, the five-year relative survival rate for local breast tumors was 99%, but was 26% for cancers that had spread to distant regions [1]. A particular focus of this research will be the MCF10A cell line. This cell line was spontaneously immortalized from a benign tissue sample from a patient with fibrocystic disease [41] and is commonly used as a non-tumorgenic control cell line for breast cancer studies. The MCF10A cell line was used as the starting point for a series of cell lines developed by H-ras oncogene transfection and subsequent xenograft passaging [42, 43]. As this series of cell lines share a common genetic background, they have been used in studies of the genetic and proteomic changes that cells undergo during cancer progression [44, 45]. In addition to the MCF10A cell line, Chapter 6 will discuss the migration behavior of the xenograft-derived MCF10CA1a cell line, which is capable of forming lung metastases when injected into a mouse tail vein [46].

2.3 Cell Interactions with Physical Properties of the Environment

In addition to changes in migration behavior caused by internal differences between cell types, cells can adapt and change their migration phenotype based on their surrounding environment. Features such as the rigidity of the underlying surface, confining structures, cell-surface adhesion, and surface topology have all been shown to play a role in cell migration [8]. There is evidence that cells can sense and respond to the stiffness of the underlying substrate with clear changes observed

in adhesion pathways and cytoskeletal behavior [9]. A gradient in surface stiffness has been shown to induce cells to migrate, a process known as durotaxis [8, 9], and changes in surrounding stiffness have also been shown to change the morphology of breast epithelial structures in three-dimensional cell cultures [47]. The adhesion of cells to their surroundings can also influence migration behavior. In work by Bergert et al. this adhesion effect was strong enough to switch carcinosarcoma cells between amoeboid and mesenchymal migration modes [26].

The role that environmental topography plays in cell migration is of particular interest in the work presented in this thesis. During the process of metastasis, cancer cells encounter a variety of structures and environmental features. The extracellular matrix (ECM) that surrounds cells *in vivo* is a highly dynamic structure consisting of many macromolecules that provide both chemical and physical signals to the cells [48]. Like other properties of the surrounding environment, the geometry of the ECM can lead to changes in cell migration [49]. Data from *ex vivo* tissue sections suggests that cancer cells can used aligned collagen in the ECM for local invasion [10]. There is also evidence from biopsied tissue sections that bundled collagen aligned away from the primary tumor is a prognostic signature of poor outcomes for breast cancer patients [11].

To investigate the influence of topography on migration futher, several *in vitro* systems have been developed to provide distinct topography to migrating cells. In experiments that place cells on singular fibers (so-called one-dimensional migration), migration exhibits many similarities to three-dimensional migration that have not been observed in traditional two-dimensional planar cell culture [50]. Cell migration

on fibrillar structures has been linked to actin-based protrusions [33], and there is evidence that septins, a component of the cytoskeleton, can respond to the micron-scale curvatures encountered on such fibers [51]. Previous work by the Losert and Fourkas labs has shown that amoeboid *Dictyostelium discoideum* cells are guided by parallel nanoridges, both in overall cell motion and actin dynamics [52]. Human breast epithelial cells show similar behavior, as will be discussed in Chapter 3. Additional work has shown that asymmetric nanostructures are capable of unidirectional guidance of both *Dictyostelium discoideum* and neutrophil-like HL60 cells [28].

2.4 Dynamics of Collective Cell Migration

In addition to the ECM, a migrating cell is often surrounded by other cells that may also influence migration behavior. In some cases, groups of cells may migrate together and the emergent behavior of this collectively moving group is an interesting dynamical system. It is also a relevant system; despite schematics of metastasis like Figure 2.2, which frequently depict single malignant cells, there is increasing evidence that groups of cells play a role in metastatic progression [12, 13]. Intravital imaging of tumors in mice, as illustrated in Figure 2.3, has shown that whereas individual cells do leave primary tumors, collective strands and sheets of cells also invade healthy tissue [53]. To invade successfully but remain a collective group, cancer cells must carefully balance the transition to a mesenchymal mode of migration with the epithelial features that give the collective an advantage [38, 54]. Experiments in mouse models have also suggested that clusters of tumor cells in the

circulation are more likely to lead to full colonized metastases than are circulating individual cells [14]. Interesting work with mixed-color tumors followed metastatic progression in mice and provided evidence that collective invasion leading to tumor cell clusters is a frequent mechanism for metastasis [15].

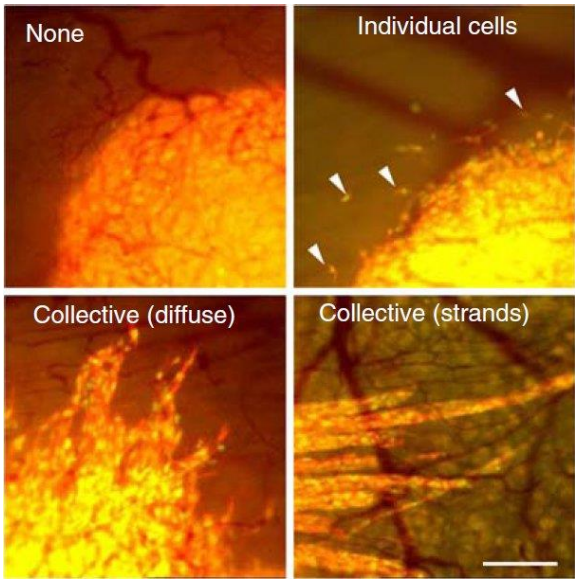

Figure 2.3: Intravital imaging of tumors in mice (tumor cells shown in yellow) shows different patterns of local invasion. In the upper left panel, no cells have left the primary tumor, whereas in the upper right panel, individual cells are invading the surrounding tissue. In the bottom two panels, collective groups of cells migrate away from the primary tumor. (This figure was reproduced from [53] with a license from Springer.)

Collective migration is also studied in a variety of *in vitro* environments. A common assay for collective migration is the scratch assay, in which a confluent sheet of cells is wounded by creating a scratch in the monolayer [55]. The cells then migrate to fill the wounded area, and can be monitored using fluorescent or phase-contrast microscopy. This method both injures the cells in the monolayer and exposes the cells at the leading edge to empty space. Alternative methods to avoid

wounding were developed to study the relative influence of these two stimuli [56], and have been widely adopted by those interested primarily in the collective dynamics of cell sheets. A popular method is to create molds or structures in which cells are grown until confluent, at which point the outer structure is removed, exposing the cells to the surrounding empty space [57, 58]. The experimental work in Chapters 4, 5, and 6 used a similar technique in which a small volume of cells first adhere to a surface before a larger volume of cell medium is added, giving the cells additional space in which to grow. This technique has the advantage of not requiring a mold structure, which may affect the cells or the migration surface upon removal.

These assays all measure quasi-two-dimensional migration. Although there is some movement in the direction perpendicular to the migration surface, the assays are designed such that the initial cell density leads to monolayers of cells. At higher cell densities, it is possible for the cells to form multiple layers or three-dimensional clusters which are more difficult to image. There are drawbacks to the monolayer approach in that tumors and metastasizing cells are found in three-dimensional environments, and several studies have found differences in two- and three-dimensional cell migration [50, 59]. However, there are *in vivo* environments in which cells may follow quasi-two-dimensional structures during migration [12]. Because of their experimental simplicity, monolayer assays can be used not just in fundamental research, but also in the pharmaceutical industry for large-scale assays and in the clinic for patient diagnosis.

In many cases, motion in these monolayer assays incorporates both active cell migration and the forces due to proliferation. The effect of proliferation can

be reduced by conducting the assays in starvation conditions or by introducing drugs that inhibit proliferation. In one study, Mitomycin C was used to inhibit proliferation, but did not change the overall monolayer edge displacement in the migration assay [57]. Other studies have seen similar effects and have put forth the hypothesis that proliferation allows the cell monolayer to fill gaps left by migrating cells rather than being used as a mechanism to induce cell motion [60, 61]. In some cases, the contribution of proliferation to the cell monolayer motion may be desirable, as it is a component of real motion within growing *in vivo* tumors.

In addition to influencing the migration of individual cells, as discussed in Section 2.3, the underlying migration surface can also change collective migration behavior. Cells have been shown to transmit forces through deformable substrates, which allows for the organization of collective behavior [62]. The shape of the substrate on which a group of cells is allowed to adhere can change the behavior of cells near the edge [63] or can lead to collective rotational motion [64]. There is also evidence that ridge structures similar to those discussed previously can also guide the migration of cell sheets [65].

2.5 Physical Models of Collective Migration

A variety of modeling techniques have been developed to explore the mechanisms and forces involved in collective migration [66]. The techniques and cellular properties studied range from lattice-based cellular Potts models of cell sorting [67] to phase-field models of deformable cell collisions [68]. Other work has investigated

the experimentally observed instabilities in the interface between a cell sheet and empty space [69], compared the effects on a cell sheet of signals originating from wounds versus empty space [70], and the quantified mechanical constraints induced by cell division [71].

These models reflect different perspectives on collective migration. As shown in Figure 2.1, crawling cells have active protrusions, change shape as they migrate, and must interact with their environment. , Due to the complexity of the systems involved, models of collective migration often focus on only some of these features, but treat the others as perturbations. The work discussed in Chapter 4 will expand on a previously published particle-based model of cell migration in which individual cell motion is modeled by active particles, each with its own force balance [16]. In this model, collective behavior arises from the simulated cells' ability to align their velocity with a preferred direction of motion that is implemented by a motility force, as shown in Figure 2.4(a). An alternative perspective, shown in Figure 2.4(b), is to model the cells using the forces they exert on each other and their substrate. This approach is often paired with experimental techniques to probe the interaction of cell groups with the substrate [72]; this will be discussed further in Section 2.6. Yet another perspective on collective behavior focuses on the shapes that a cell takes within a group; as shown in Figure 2.4(c), cell shape is a function of cell features such as adhesion and cortical tension coming from the cytoskeleton. As discussed further below, such cell-shape models have found transitions in migration behavior similar to those seem in inanimate systems [73].

Comparison of collective migration models and experimental results have led

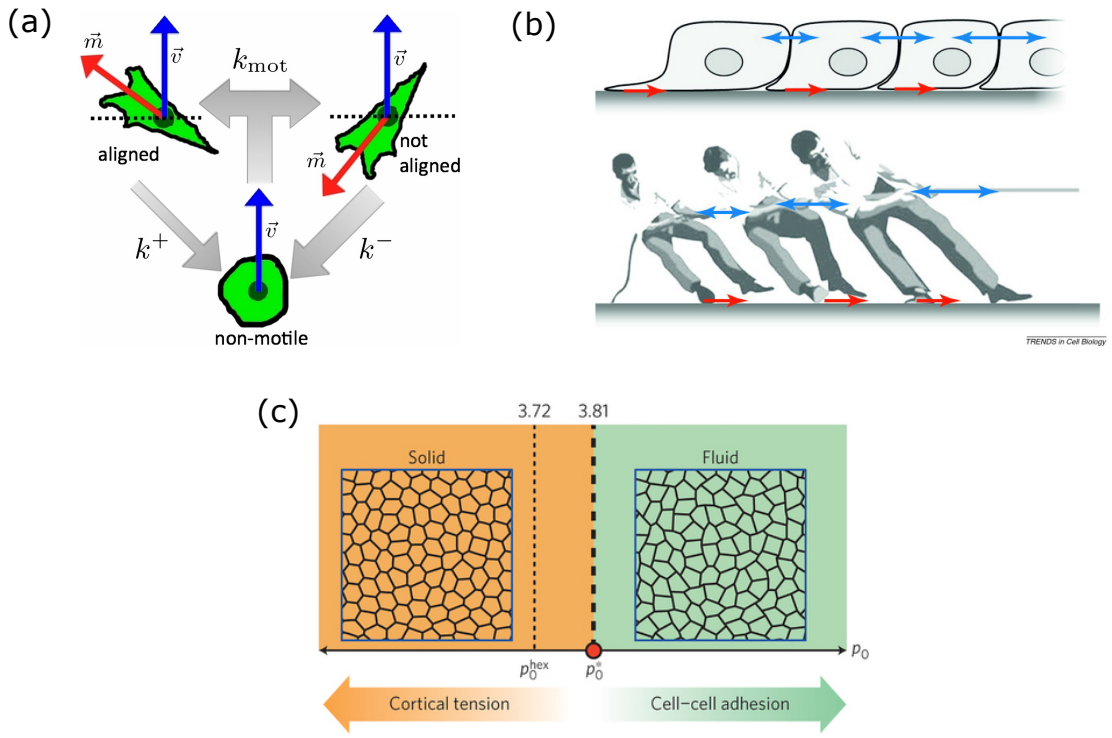

Figure 2.4: **Modeling Perspectives in Collective Migration** (*a*) In a model by Basan et al. [16], collective motion arises from the interaction of cells each responding to forces in their environment. Collective behavior arises from a coupling between the cells' velocity and preferred direction of motion (labeled as the motility force, $\vec{m}$). (This figure was reproduced from [16] as allowed by the Rights and Permissions Policy of the National Academy of Sciences.) (*b*) Trepat et al. [72] model collective migration as a 'tug of war' in which cells pull on each other and the underlying substrate to migrate. (This figure was reproduced from [72] with a license from Elsevier.) (*c*) Bi et al. [73] model collective migration by determining the shapes that cells take within the monolayer. Cells undergo a jamming transition at a critical value of $p_0 = P/\sqrt{A}$ (This figure was reproduced from [73] with a license from Nature Publishing Group.)

to an interesting analogy between cellular motion and the behaviors seen during jamming in inanimate systems. A schematic phase diagram for jamming is illustrated in Figure 2.5(a), and shows possible transitions between a fluid-like state and

jammed, solid-like state. In the case of liquid systems, a decrease in temperature can lead to a glass transition in which the system forms a disordered solid. Analogously, a system such as sand can form a constrained state when density is increased [74]. A comparable transition to a 'jammed' state has been hypothesized for collective cell migration. In the schematic proposed by Sadati et al. (Figure 2.5(b)), cell-cell adhesion, cell density, and motility influence collective cell behavior [75]. At higher densities and increased adhesion strength, cells are jammed and unable to move, whereas cells in low-density or low-adhesion conditions exist in a more fluid-like state [75].

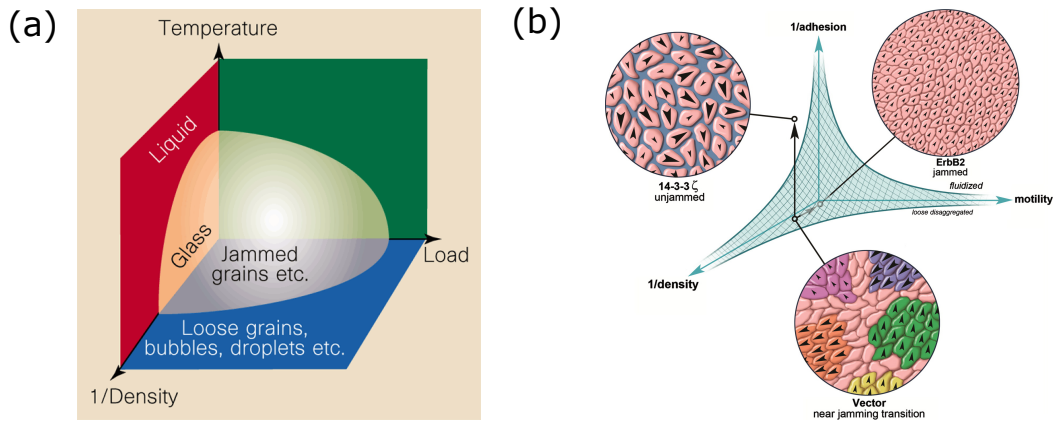

Figure 2.5: (*a*) A schematic of the jamming transition in inanimate systems. (This figure was reproduced from [74] with a license from Nature Publishing Group.) (*b*) A proposed analogous schematic phase diagram for collective cell migration (This figure was reproduced from [75] with a license from Elsevier.)

Evidence for a cellular jamming transition has been observed experimentally in elongated fibroblast cells, in which regions of ordered alignment increased and motility decreased as cell density increased due to proliferation [76]. In experiments with

Madin-Darby canine kidney (MDCK) cells, increased density led to slower migration accompanied by growing domains of the fastest moving cells, a feature reminiscent of the glass transition [77]. Human bronchial epithelial cells also show decreased migration speed associated with growing dynamic heterogeneities, which has been related by a combination of experimental and modeling work to the strengthening and maturation of cell-cell adhesion contacts in the system [78].

The jamming transition in cell monolayers has also been linked to cell-shape dynamics. In work with primary bronchial epithelial cells from asthmatic and non-asthmatic patients, Park et al. found a transition to a jammed state with *decreased* adhesion [79], in contrast to the intuitive assumption of increased adhesion during jamming shown in Figure 2.5. Unlike inanimate systems such as jammed sand grains, in an epithelial cell system, cell-cell adhesion is actively coupled to other features of cell behavior which may also change migration behavior. Park et al. suggest that competition between cell-cell adhesion and cortical tension within the cell leads to shape changes that ultimately control the observed cell jamming [79]. These two forces lead to a competition between cell stiffness and membrane line tension, which leads to a preferred shape of the cell. The preferred cell shape can be parameterized as $p = P/\sqrt{A}$, where P is the cell perimeter and A is the cell area (in the case of a circular cell, $p \approx 3.54$). Experimentally, the cells were shown to experience a jamming transition at a critical value of this shape parameter, $p_0 \approx 3.8$ [79]. This idea was further explored in a vertex model by Bi et al. that calculates the energy a cell within a monolayer based on the cell's elasticity, contractile forces within the cell, and the interfacial tension that develops due to cortical tension

and cell-cell adhesion [73]. At shape parameters less than the critical value, $p_0 \approx 3.8$, the cells experience finite energy barriers to rearrangement, and the system behaves as a solid, as shown in Figure 2.4(c). As p is increased, the energy barriers decrease and the system is able to rearrange fluidly, leading to a rigidity transition that shows some resemblance to the jamming transition observed during density changes in inanimate systems [73]. Recent work has combined this non-motile vertex model with a self-propelled particle model, together identifying three parameters to control the transition between solid and fluid-like behaviors in cell monolayers: the speed of individual cells, the persistence time for motion of individual cells, and the previously-described shape parameter $P/\sqrt{A}$ [80]. This work suggests that the phase transition schematics shown in Figure 2.5 need to be adapted further to capture the complex motion of cell monolayers fully.

2.6 Quantifying Collective Migration Dynamics

Experimental studies on cell monolayers often rely on time lapse imaging. These images can be analyzed for information about the dynamics of collective migration. In a commonly used technique, individual cells within the monolayer are tracked, often by using a fluorescent tag within the cell, such as labeled nuclei (see the bottom of Figure 2.6). An alternative technique, which has quickly become popular in the collective migration field, is particle image velocimetry (PIV). PIV provides information about the flow of the entire monolayer (see the top of Figure 2.6). PIV has been heavily used in the field of fluid dynamics, and a large litera-

ture exists on its implementation [81]. Essentially, this technique divides time-lapse images into gridded pixel regions and calculates correlations to determine how features in one frame have moved to the next. Details on how PIV was implemented for this thesis work are provided in Appendix A. Although developed for use in studies of fluid flows, PIV has been successfully used on cell monolayers by many research groups. An alternative implementation to the one described in this thesis is presented in [82]. PIV has gained popularity since it does not require fluorescent markers. Unlike cell tracking, PIV does not provide information about the motion of individual cells, but it does capture motion within the sheet that would not be captured by simply tracking cell nuclei. Thus, the two techniques provide complementary information about collective migration.

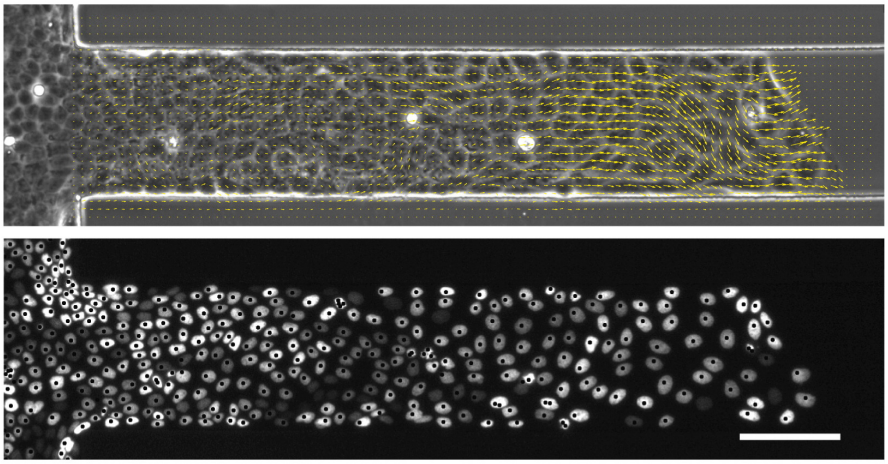

Figure 2.6: Two different images are taken of a cell monolayer migrating within a confined channel. In the top panel, the bright-field image is overlaid with the velocity vectors from PIV analysis. In the bottom panel, the fluorescent nuclei are marked by the centers found for tracking. (This figure was reproduced from [83] with a license from Elsevier.)

Studies using cell tracking have found correlated streams of cell motion in cell sheets [84], followed the mechanical interactions that guide cell sheets on ridged substrates [65], and followed the bursting motion of soft cancer cells in a sheet of stiff healthy cells [85]. Image analysis using PIV has also been used to look for long range correlations in monolayer motion [61]. PIV-based correlations have investigated changes across cell types and found changes in migration related to cell density [86]. Fluctuations in cell density have been related to diverging and converging regions of the PIV flow field, leading to interesting observations of fluid transfer between cells within a monolayer [87]. PIV has also been used to distinguish the behavior of healthy and malignant cell lines. In these studies directionality was found to be a better marker for changes in collective migration than monolayer speed [57].

Researchers have also identified migration differences in cell monolayers of different sizes. Cells migrating within large channels show large-scale vortices in their PIV flow, whereas monolayers confined to small channels have been shown to use a contraction-relaxation motion to move forward [88]. Work combining PIV flow analysis with fluorescent nucleus tracking has shown that monolayer flow in these channels allows cells to rearrange more often than would be seen in a resting tissue (Figure 2.6) [83]. Cell division within the monolayer has also been investigated using a combination of both image analysis techniques, leading to observations of the division axis aligning with the flow [89].

Other work has used PIV and tracking to show that three-dimensional spheres of cells spread on flat surfaces much like water drops. This spreading was found to be

sensitive to substrate stiffness [90]. Other studies have used time-lapse image analysis to show that substrate stiffness can influence speed, persistence, directionality, and coordination within cell monolayers, with cells on stiffer substrates exhibiting behavior that is more collective [91]. PIV has also been combined with techniques that investigate the interaction of cell monolayers with the underlying substrate. A study that placed cell monolayers on flexible micropillars showed that cells throughout the monolayer (i.e., not just those at the leading edge) were actively contributing to the observed migration and resulting PIV flow field [88]. A technique known as traction force microscopy uses fluorescent tracers embedded in the underlying substrate to measure surface deformations [92]. This technique has been used along with PIV to investigate density effects and vorticity within cell sheets [62]. Traction force microscopy has also been used to show that cells prefer to migrate and remodel the cell sheet so as to maintain minimal intercellular stress (plithotaxis) [93] and that cells generate traction forces into unfilled spaced (kenotaxis) [94]. A combination of PIV and traction force microscopy has also been used to investigate the role that cell-cell adhesion plays in collective migration [95]. Cell-cell adhesion will be discussed further in Section 2.7.

Quantitative image analysis has also been used to facilitate the comparison between cell monolayers and the jamming transition. PIV was used to show that dynamic heterogeneities grow whereas speed decreases with cell density in a cell monolayer in a manner that is similar to that seen in the glass transition [77]. The flow fields derived from PIV also suggest that jammed cell monolayers retain strong leading-edge borders upon collision with another monolayer [96]. The work discussed

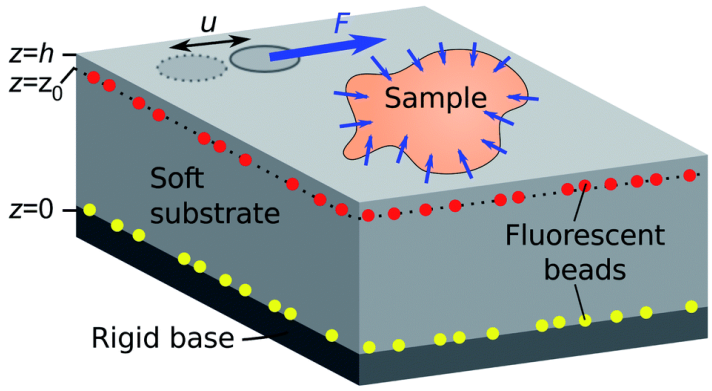

Figure 2.7: This schematic of traction force microscopy shows beads embedded within a deformable substrate. The forces from a sample, such as a cell monolayer, move the soft substrate and the embedded beads; the forces exerted can be calculated from the imaged displacements of the beads. (Figure reproduced from [92] with permission from The Royal Society of Chemistry.)

in Section 2.5 on jamming transitions during asthma [79] and maturation of cell-cell contacts [78] was also based on PIV analysis.

The comparison between cell monolayers and jamming systems also provides tools for understanding cell rearrangements. The concept of non-affine motion has been used to investigate dynamics in a variety of systems, including granular systems [97] and polymer hydrogels [98]. It has also been used in simulations of dense tissues, where cell rearrangements were found to depend on the number of neighbors [99]. A schematic of non-affine motion is illustrated in Figure 2.8. Affine motion corresponds to the smooth motion of the system, whereas the non-affine components correspond to the remaining irreversible components of motion. Chapter 5 will discuss a metric, D^2_{min}, that quantifies the non-affine motion in a system of particles, and will use this metric to extract information about cell rearrangements from nuclear tracks.

The metric D^2_{min} has also been used to quantify non-affine motion in supercooled colloidal liquids [100], in sheared colloidal glasses [101], and in granular convection under microgravity conditions [102].

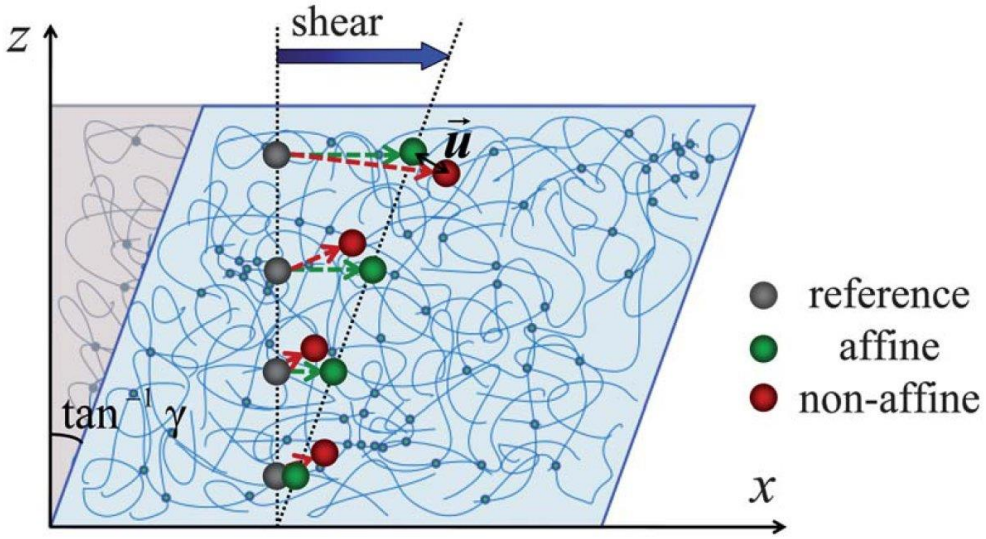

Figure 2.8: If all motion with the illustrated polymer hydrogel were affine, then upon the application of stress the tracer beads would smoothly move to from the gray to the green marked positions. Because the bead motion also includes a non-affine component, the beads actually moved to the red indicated positions. (Figure reproduced from [98] with permission from The Royal Society of Chemistry.)

The motion of cell monolayers has also been compared to the motion of fluid flows, a comparison that is often facilitated by PIV measurements of the cellular flow. In addition to the PIV analysis techniques discussed previously, Zorn et al. review the ways in which cell flows have been compared to fluid flows [6]. A metric of particular interest in this thesis is the finite-time Lyapunov exponent (FTLE), which measures the divergence of tracer particles in a fluid flow. We experimentally measure this divergence over a finite time period in which it asymptotically

approaches the divergence value associated with the Lyapunov exponent [103]. This metric has been used to provide a measure of mixing in fluid flows [104], and ridges of the FTLE flow field have been shown to provide almost complete barriers to mixing [103]. The metric's ability to describe mixing has made it of use in a wide variety of systems, including during predictions of the environmental outcome when contaminants are introduced to a system [105]. Chapter 5 will discuss the application of this technique to cellular flows and FTLE values will be used as metric for understanding collective behavior in Chapter 6.

2.7 Cell-Cell Adhesion Forces during Collective Dynamics

In many collective cell migration systems, particularly epithelial sheets, cells are known to adhere to each other using a variety of adhesion molecules. These adhesions have been shown to induce similar changes in the actin cytoskeleton as those seen in cell-surface adhesion [106], and can thus similarly influence cell migration (the role of surface adhesion is discussed in Section 2.3). Indeed, as early as the 1960s adhesion molecules were suggested to play a role in the rearrangement of cells in three-dimensional tissues [107]. This work led to the Differential Adhesion Hypothesis (DAH), which proposes that cell aggregates sort and separate due to liquid-like surface tensions. Simple experiments with cell aggregates expressing varying levels of adhesion molecules seem to support the DAH [108], but newer work has suggested that the DAH leaves out important contributions from the contractility of the cell cytoskeleton [109]. Indeed, in some cases, adhesion molecule density is incapable of

predicting the sorting of cell aggregates [110], although a functional surface tension based on many components of the cell may still provide a useful tool for predicting cell behavior. A similar balance of forces has also been reported in two-dimensional monolayers, where the balance between cell-cell adhesion and myosin contractility was found to be important for the coordination of cell movements [91].

Many types of adhesion exist in epithelial layers: adherens junctions, tight junctions, desmosomes, and gap junctions may all play a role in collective migration behavior [95]. Adherens junctions encompass the cadherin family of adhesion molecules and are known to facilitate force transmission across cells [95, 111]. The cadherin family is composed of many types, including E-cadherin, P-cadherin, and N-cadherin. Although these molecules are named after the tissue in which they were first found (epithelial, placental, and neural, respectively) [112], they have all since been found in a variety of tissue types, including epithelial sheets such as those discussed in this thesis [95]. During migration, cadherins play a role in adhesion based lowering of the interfacial tension between cell contacts, as well as the lowering of tension due to rearrangement of the cytoskeleton, and are also able to stabilize contacts by responding to mechanical forces exerted on cell-cell contacts [111].

As it was first found in epithelial tissues, E-cadherin has been a focus of study in cell sheet migration. This calcium-dependent adhesion molecule has been shown to play a role in both tissue formation and the suppression of cancer [113]. Indeed, E-cadherin is a classical epithelial marker during EMT [17], and has been associated with the activation of invasion and metastasis [18]. Decreased or negative expression of E-cadherin has also been associated with higher-grade tumors and

metastasis in patient samples [114, 115] and may in some cases be useful as as prognostic marker [116]. Despite these associations, the role that E-cadherin plays during cancer progression is unclear. Indeed, studies suggest that circulating tumor cells may be able to retain E-cadherin expression in clusters [14] or re-express the protein upon metastatic colonization [40]. Experiments with epithelial sheets have also suggested a complex role for E-cadherin in migration. In one study using knockdown of adhesion molecules (i.e., a decrease but not deletion of expression of proteins in the cell), E-cadherin was found to be a good predictor of the build-up of intracellular tension, but P-cadherin was a better predictor of the final magnitude of tension [95]. The ability of E-cadherin to regulate some but not all properties of collective migration will be further described in Chapter 6.

Chapter 3: Guidance of Individual Cells by the Underlying Surface

Matt J. Hourwitz and Xiaoyu Sun prepared the nanotopography surfaces. Ava Omidvar, Johnathan Holtmann, and Mario Denzler hand-tracked and traced cells. Rachel Lee performed the MCF10A migration experiments and analyzed the migration data.

3.1 Overview

Many types of cells are known to exhibit contact guidance, which is the ability to sense and follow the texture of their environment. Simple contact with topographical features such as collagen fibers can lead to persistent directional migration without the need to coordinate the spatial and temporal dynamics of guidance cues such as gradients in chemical concentration (i.e., chemotaxis). In previous studies, we have shown that actin polymerization in fast-migrating *Dictyostelium discoideum* cells can be guided by ridged topographical features [28, 52], leading to directed cell migration. In this work, we show that the migration of epithelial MCF10A cells is also influenced by contact with these surface textures, which have micro- and nano-scale features similar to those of collagen fibers. In contrast to *Dictyostelium* cells, which migrate with a speed of approximately $10\,\mu m/\,min$ [52], MCF10A cells

move with a speed on the order of $0.5\,\mu\text{m}/\,\text{min}$ [117]. We observe esotaxis, the preferential nucleation and guidance of actin waves by nanotopography [28], in the MCF10A cells. The cells also show both alignment of their shape with the ridged surface and increased directional persistence. The existence of esotaxis across phyla and in cell types with migration speeds that differ by an order of magnitude suggests that cytoskeletal dynamics play an important role in texture sensing and directional cell migration.

3.2 Background

Cell migration is a ubiquitous phenomenon in a wide range of cell types and can take on a variety of modes depending on the environmental context. Individual neutrophils migrate in response to tissue damage [23], whereas *Dictyostelium discoideum* cells aggregate in response to lack of nutrients [118]. Epithelial cells move collectively both during development [20, 21] and during wound closure [22]. Disruption of normal migration behavior—either a lack of migration or migration to inappropriate sites—can lead to a variety of health problems, including diseases such as metastatic cancer [24]. Increased understanding of the mechanisms that trigger and guide cell motion may lead to new therapies for migration-related diseases.

One important mechanism that is not well understood is the guidance of cells by environmental texture cues. Because such cues are missing in the flat environments used in standard cell culture, the importance of texture for cell migration has often been overlooked. The topography of *in vivo* microenvironments includes

many cues with micro- and nanoscale features. The structure of the surrounding microenvironment can influence cell migration [119]. Cells may also remodel their environment, leading to further changes in migration behavior [119]. This texture may include oriented fibers such as those present in collagen or the shapes of adjacent cells within the surrounding tissue. Such topography has been shown to play a role in some diseases. For example, tissue microenvironments that contain aligned collagen fibers have been associated with poor survival rates for breast carcinoma patients [11].

Contact guidance has been shown in many experimental systems through static images of cells aligning with fibers or ridge-like structures [120–122]. Recently, micro- and nanoscale ridges and grooves have been used to show both cell alignment and guided cell migration parallel to these fiber-like features [52, 65, 123]. However, the cellular mechanism for sensing such topography has remained unclear. Although there is some evidence that BAR-domain proteins are involved in inducing and recognizing nanometer-scale membrane curvature [124], it is unlikely that single proteins with a size on the nanometer scale can sense the curvature of textures that are on the hundreds of nanometers scale.

Recent work has suggested that the cytoskeleton plays a role in topography sensing. Fibroblasts have been shown to align not only their cell body but also actin stress fibers to oriented fibronectin fibers [50]. We have previously shown that fast-migrating *Dictyostelium* cells align to ridged topographies that have features on the scale of hundreds of nanometers and exhibit guided polymerization of actin along the ridge structures [52]. The observed actin waves have a width comparable

to that of the topography [52]. These two studies show that the natural, wave-like dynamics of the actin cytoskeleton can be guided by appropriate topographic structures, a process known as esotaxis [28]. The guided polymerization of actin may then result in guidance of cell migration by the topography, a process known as microthigmotaxis [28]. Previous work has also shown that surface textures that are asymmetric on the nanoscale can lead to unidirectional guidance of both actin polymerization and cell migration [28].

In this study, we measure the dynamics of migration and actin polymerization in epithelial MCF10A cells which, in contrast to the previously studied *Dictyostelium* cells, exhibit slow, adhesion-dependent migration. Despite the distinct behavior of these two cell types, we observe that esotaxis and microthigmotaxis are also present in the MCF10A cells. The fact that these features of contact guidance are seen in both soil-living amoeba and human epithelial cells supports the ubiquitous nature of topography in influencing cell migration.

3.3 Results

3.3.1 Epithelial Cells Exhibit Microthigmotaxis on Nanoridges

Epithelial MCF10A cells were plated on parallel nanoridges. The ridges, which were coated with collagen IV, had a 1.5 µm spacing. After adhering overnight, the cells were imaged every three minutes for fifteen hours (Figures 3.1(a) and 3.1(b)). Tracks from a representative movie show that individual cells on a flat surface migrate in all directions (Figure 3.1(c)). Tracks of cells on the nanotopographic surface

are preferentially guided along the nanoridges (Figure 3.1(d)). The distribution of directions of motion from all tracked movies shows the same trend: on flat surfaces, cells move in all directions, but on nanotopographies, the MCF10A cells are biased to move parallel to the nanoridges (Figure 3.1(e)). The time it takes cells to travel a given distance is also longer on the flat surfaces, as shown by the mean first-passage times in Figure 3.1(f). The mean first-passage diverges between the two cases as distance increases, suggesting increased migration persistence on the ridged surfaces.

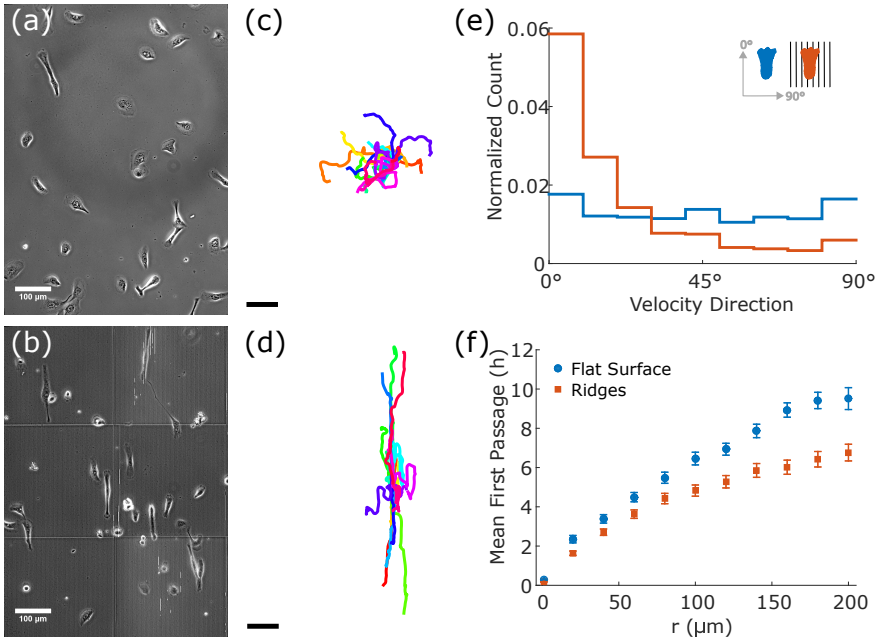

Figure 3.1: Analysis of cell tracks on a flat surface and on 1.5 µm spaced nanoridges shows contact guidance of MCF10A cells. Phase-contrast images of the cells with a scale bar of 100 µm (a,b). Cell tracks from a representative movie are shown over 10 h with scale bar 100 µm (c,d). The normalized velocity direction distribution is shown for all cells in all frames over all movies (e). The mean first-passage time to reach a displacement r is shown in (f); error bars indicate standard error of the mean across cells. In (e,f), there are n = 150 cells on the flat surface and n = 141 cells on the ridged surface from N = 2 days of experiments.

3.3.2 Cells Show Persistent Elongated Morphology on the Nanoridges

In previous work with *Dictyostelium discoideum* cells, cells that moved parallel to the ridges were found to elongate along the ridges [52]. Here we investigate the shape dynamics of MCF10A cells on flat and nanoridged surfaces. Figure 3.2 shows that cells migrating on nanoridges have a more polarized phenotype than cells on a flat surface. Figure 3.2(a) shows the eccentricity of a representative cell migrating on a flat surface compared to that of a cell on a ridged surface. As shown by the measurement of the aspect ratio of these representative cell shapes over time (Figure 3.2(b)), cells tend to remain elongated and polarized over longer periods on the ridged surface than they do on a flat surface. The cells thus exhibit a higher aspect ratio on ridges than on flat surfaces (Figure 3.2(c)).

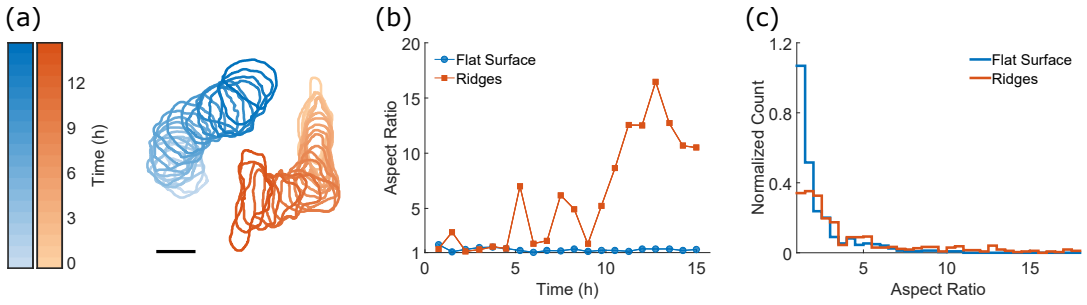

Figure 3.2: Representative shapes of cells on a flat (blue) and a ridged surface (orange) show differences in polarization over time (*a*). Light-colored outlines transition to dark-colored outlines over an experimental time of 15 h (*a*, scale bar is 50 µm). The aspect ratio of the representative cells over time shows persistent polarization on the ridged surface, whereas the cells on the flat surface remain circular (*b*). Distributions of aspect ratio are shown for for n = 31 cells on the flat surface and n = 30 cells on the ridged surface from N = 2 days of experiments (*c*).

3.3.3 Nanoridges Promote Esotaxis

To investigate esotaxis on nanoridges, we monitored cells migrating on sets of ridges with a spacing of 0.8 µm or 1.5 µm. These spacings are of the magnitude (1 to 2 µm) found to promote esotaxis efficiently in a prior study of *Dictyostelium* cells [52]. We used MCF10A cells expressing F-Tractin GFP to visualize actin polymerization waves and reveal the dynamics of esotaxis. Our preliminary data suggest that the morphology of actin on the ridged surfaces is distinct from that on flat surfaces (Figure 3.3(a)). On both the 0.8 µm and 1.5 µm spaced ridges, the actin shows streaks running parallel to the nanoridges (Figures 3.3(b) and 3.3(c), respectively).

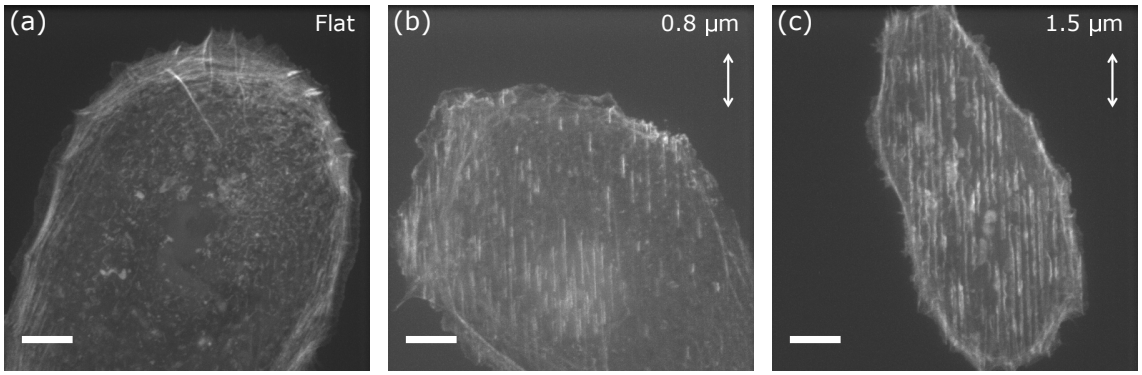

Figure 3.3: Actin shows distinct morphology on flat and ridged surfaces. Maximum-intensity projections are shown of MCF10A cells labeled with F-Tractin GFP on flat (*a*), 0.8 µm spaced ridges (*b*), and 1.5 µm spaced ridges (*c*). The white arrow indicates the direction of the ridges (*b*,*c*) and the scale bar is 10 µm in (*a*-*c*). Preliminary data from N = 1 day of experiments.

In addition to the changes in morphology, actin dynamics are also guided by the ridged surfaces. Figure 3.4 shows the actin dynamics of a cell that is positioned

half on a ridged surface and half on the surrounding flat surface. The distinction between the two surfaces is shown by the bright-field image in Figure 3.4(a). Time lapse imaging of F-Tractin GFP in this cell (Figure 3.4(b)) shows membrane ruffling on the flat surface. On the ridged surface, actin propagates along the ridge direction, as shown by the kymographs in Figure 3.4(c). In each case, the actin streaks indicated by the regions in Figure 3.4(b) grow along the ridge direction, as shown by the kymographs over a time scale of 20 min in Figure 3.4(c).

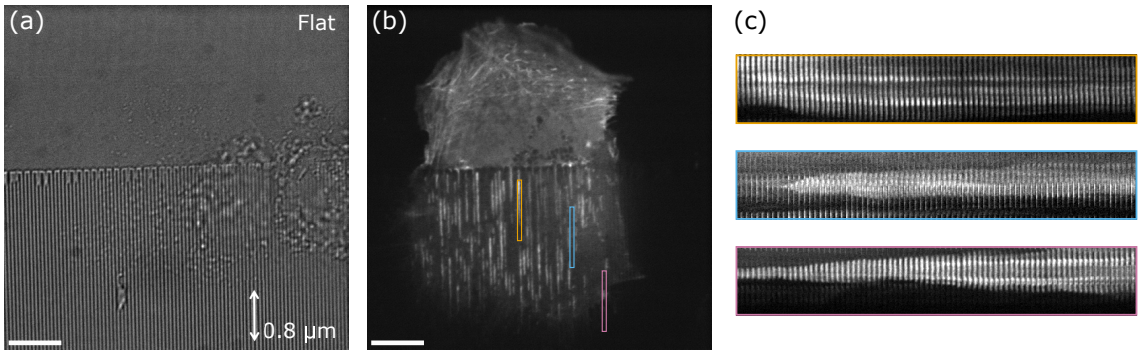

Figure 3.4: A cell is shown half on a flat surface and half on a 0.8 µm spaced ridge surface in bright-field (a) and F-Tractin GFP (b). The images in (a,b) show a single z-slice. The white arrow indicates the ridge direction and the scale bar is 10 µm. The regions marked in (b) are shown over time in (c). Each kymograph in (c) has a height of 12.6 µm and the horizontal axis shows a total time of 20 min. Each image in the kymograph was taken 16 s apart. Preliminary data from N = 1 day of experiments.

3.4 Discussion

Despite the ubiquitous nature of cell migration in a variety of biological systems, such as embryonic development [20, 21] and cancer [24], the mechanisms by

which cells interpret physical signals from their environment are not well understood. Here we have shown that ridged structures with features on the scale of collagen fibers, such as those that would be in found in *in vivo* microenvironments, are capable of promoting directional migration and guiding cytoskeletal dynamics. Strong similarities are seen between the migration of MCF10A cells presented here and previously published work on *Dictyostelium* cells [52].

Live-cell, time-lapse imaging of MCF10A cells revealed persistent directional migration parallel to nanoridges. Our preliminary data suggest that actin polymerization also follows the ridge direction. These dynamic measurements provide insight into the mechanisms of contact guidance. Along with the previous measurements of *Dictyostelium* cells [28,52], these results suggest that esotaxis may polarize cells and lead to persistent directional motion. One exciting prediction that arises from the similarity is that using asymmetric structures, the dynamic nature of esotaxis may also be used to promote unidirectional cell motion [28]. Thus, micro- and nanoscale topography in the cell environment could be an important regulator of cell migration in both normal and pathological processes which rely on cell migration, such as wound healing [22] or metastasis [2].

In vivo contact guidance signals in the microenvironment must be integrated with other cues such as large-scale, external gradients in chemical concentration (chemotaxis) [19] or gradients in substrate rigidity (durotaxis) [8,9]. These gradient-based mechanisms provide clear directional signals to cells, but they are limited to finite distances by the ranges over which cells can sense both concentration and concentration gradients. The esotactic mechanism of contact guidance described in

this work does not require large-scale gradient sensing and thus can complement these gradient-based mechanisms for directed migration. The conservation of esotaxis across cell types and phyla suggests that it can be used to guide migration in many different biological processes. Thus, the esotactic mechanism of contact guidance is an important contribution to the cellular tool set for directed migration.

3.5 Materials and Methods

3.5.1 Cell Preparation and Imaging

MCF10A cells were cultured in DMEM/F12 media supplemented with 5% horse serum, $10\,\mu g\,mL^{-1}$ insulin (Invitrogen), $10\,ng\,mL^{-1}$ EGF (Peprotech, Rocky Hill, NJ), $0.5\,\mu g\,mL^{-1}$ hydrocortisone (Sigma, St Louis, MO), and $100\,ng\,mL^{-1}$ cholera toxin (Sigma, St Louis, MO). Before imaging, cells were plated on a nanoridge surface coated with collagen IV and were allowed to adhere to the surface overnight. Cells were then imaged for 15 h on an incubated microscope kept at 37 °C and 5% CO_2 (Zeiss Observer.Z1, Zeiss, Goettingen, Germany). Phase-contrast images of the cells were acquired at 3 min intervals using a 10× objective. In additional experiments, cells plated on nanoridges were transiently transfected using Effectene reagent (Qiagen, CA) with an F-tractin GFP plasmid (a gift from Dr. Clare Waterman's group). Actin dynamics were studied using confocal fluorescence and bright-field time-lapse imaging using a Perkin-Elmer spinning disk confocal microscope. F-tractin images were taken every 4 seconds with a 100× objective.

3.5.2 Surface Fabrication

Sets of parallel ridges were fabricated as previously described [28, 52]. Migration experiments were performed on ridges 900 µm long with a spacing of 1.5 µm, whereas the actin dynamics experiments were performed on 300 µm long ridges with a spacing of 0.8 µm or 1.5 µm. Cells were also imaged on the flat surface surrounding the ridge structures.

Replicas of ridges were created by placing a drop of acrylate resin between the mold and an acrylate-functionalized coverslip and then UV curing at 365 nm. The nanoridge surfaces were cured under UV for 5 minutes and soaked in UltraPure™ Distilled Water (Invitrogen) overnight. The surfaces were coated with 3.25 µg cm^{-2} collagen IV (mouse, Corning) in 0.05 M HCl for 1 h. Subsequently, the collagen was removed and the surface was rinsed twice with UltraPure™ Distilled Water.

3.5.3 Measuring Microthigmotaxis

A variety of measures were used to assess the extent of microthigmotaxis. The MCF10A cells were manually tracked using the MTrackJ plugin [125] for ImageJ software (NIH). Tracks less than 20 frames in length were discarded. The resulting tracks were analyzed for speed and directionality using custom MATLAB scripts. Velocity direction distributions are normalized such that the area under the curve is one. Mean first-passage time was calculated from cell tracks by determining the time required for a cell to reach a displacement greater than or equal to a given distance r. This value was calculated starting from each frame of the track and

averaged over starting frames to create a mean value for each cell.

To determine the aspect ratio of cells migrating on ridges, shapes of migrating cells were manually extracted from phase contrast time-lapse movies. The aspect ratio is the ratio of the major and minor axis lengths of the cells, which were determined using the built-in `regionprops` function in MATLAB. A cell with a high aspect ratio has a more polarized shape than does a cell with a low aspect ratio (a circular cell would have an aspect ratio of one).

Chapter 4: Guidance of Individual Cells by their Neighbors

This chapter is adapted from Lee, Yue, Rappel, and Losert (submitted). Haicen Yue performed the simulations. Rachel Lee performed the migration analysis.

4.1 Overview

Cell migration plays an important role in a wide variety of biological processes and can incorporate both individual cell motion and collective behavior. The emergent properties of collective migration are receiving increasing attention as collective motion's role in diseases such as metastatic cancer becomes clear. Yet, how individual cell behavior influences large-scale, multi-cell collective motion remains unclear. In this study, we provide insight into the mechanisms behind collective migration by studying cell migration in a spreading monolayer of epithelial MCF10A cells. We quantify migration using particle image velocimetry and find that cell groups have features of motion that span multiple length scales. Comparing our experimental results to a model of collective cell migration, we find that cell migration within the monolayer can be affected in qualitatively different ways by cell motion at the boundary, yet it is not necessary to introduce leader cells at the boundary or to

specify other large-scale features to recapitulate this large-scale phenotype in simulations. Instead, in our model, collective motion can be enhanced by increasing the overall activity of the cells or by giving the cells a stronger coupling between their motion and polarity. This finding suggests that investigating the activity and polarity persistence of individual cells will add insight into the collective migration phenotypes observed during development and disease.

4.2 Background

Collective cell migration is an important biological phenotype used in many biomedical assays. For example, in a wound healing assay, the speed at which two monolayers of cells migrate toward each other is often measured to determine a cell migration response to drug treatments. The use of collective migration as a biomedical phenotype stems from its important role in many biological processes. Collective migration is essential for development [20,21] and wound healing [22,126], but its misregulation plays a role in diseases such as metastatic cancer [12, 54]. It is nontrivial, however, to infer single-cell migration behaviors from metrics such as the monolayer boundary displacement. Despite many studies of the behavior of individual cells, which have looked at features of migration such as the influence of the surrounding microenvironment [8, 50, 127] or the flow of actin within a migrating cell [31, 32], the connection between properties of individual cell and collective behavior remains unclear.

To infer single-cell phenotypes from collective migration behavior requires ad-

ditional information beyond that provided by metrics such as time to wound closure. Particle image velocimetry (PIV) allows us to extract not only boundary motion from time-lapse imaging data, but also the entire flow field of cell motion, which includes features at the scale of single cells or smaller. Since their introduction into cell migration research several years ago, PIV flow fields have rapidly emerged as a powerful tool and have been used to analyze a wide variety of collective cell behaviors, including vortices [62], patterns of stresses within the cell sheet [58], and changes to collective migration during malignancy [57].

Here we link detailed metrics of collective behavior derived from PIV data with simulations of collective cell motion that explicitly model the behavior of individual cells. By linking experiments and simulations, we can infer likely single-cell behavior from collective motion phenotypes. Collective cell migration has been studied using a wide variety of modeling techniques [16, 66–68]. These modeling techniques have been used to explore a variety of factors involved in collective migration that are difficult to access experimentally, including the effect of matrix geometry on migration strategies [49] and the maturation of cell contacts within a monolayer [78].

Our work links previously published experimental observations on collective migration of MCF10A breast epithelial cells [117] and a previously published model of collective migration [16, 128, 129] to elucidate which properties of individual cells are most consistent with the observed multi-cell collective migration behavior. The experimental data show changes in collective behavior on large length scales that span the cell monolayer. We show that these changes in large-scale migration patterns can be recreated in our model without requiring large-scale gradients or leader

cells (a subpopulation of cells at the edge of the monolayer that has different properties than cells within the bulk of the monolayer). Our modeling results suggest that the experimentally observed changes in collective behavior are consistent with simply decreasing the activity of individual cells as long as the cells have a strong coupling between their velocity and preferred motility direction.

4.3 Results

To study large-spatial-scale migration patterns in epithelial MCF10A cells, we analyze a previously published set of time-lapse images of a circular cell monolayer. The cells were imaged near the edge (Figure 4.1(a)) and in the center of the monolayer; a schematic of the imaging fields of view is shown in Figure 4.1(b). The multiple fields of view allow us to investigate migration behavior as a function of location within the monolayer. Figure 4.1(c) shows a representative kymograph of speed within a monolayer. There are heterogeneities in speed over both the sixteen-hour time course and approximately 4 mm spatial scale of the cell sheet, yet there is a trend towards higher speed at the edge of the monolayer. This trend can be seen in the time-averaged speed curves in Figure 4.1(d).

Although the cell speed increases near the edge in all experiments, there are changes in the overall speed depending on the media dilution (1:1 vs 1:5) and day-to-day variability in the experiments. In addition to measuring speed, which indicates how active the cells are, we also determine the radial velocity as a measure of how well the cells' motion contributes to the overall expansion of the cell sheet. As

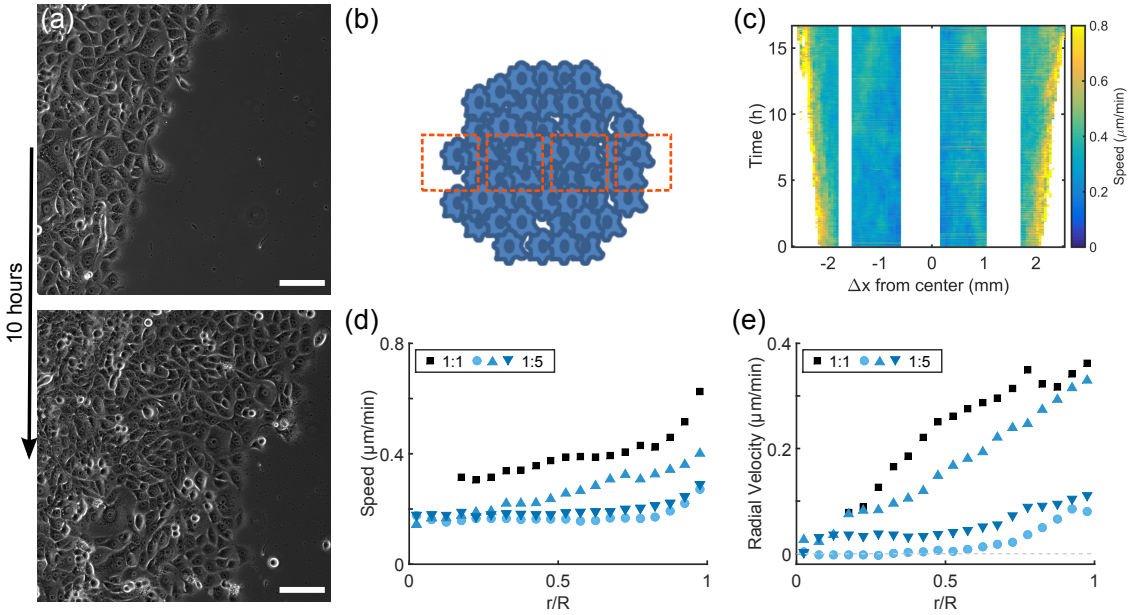

Figure 4.1: MCF10A cell sheets migrate collectively over ten hours (a, scale bar 100 µm). The cells are plated in a circular monolayer and multiple fields of view scanning the diameter are imaged (b). Over time, these regions show different speed profiles with larger speeds seen near the edge of the cell sheet (c). The experiments show variability in overall speed, but cells near the edge remain faster (d). In low speed cases, the radial velocity decreases but also qualitatively changes pattern (e). Each curve in (d,e) represents the average over four technical replicates performed on the same day in full media (1:1) or diluted media (1:5).

shown in Figure 4.1(e), when the overall motion is slow, we see a decreased radial velocity, as would be expected. In addition to this quantitative change, however, we also see a qualitative change in which some experiments exhibit a concave curve (black squares in Figure 4.1(e)) whereas others—those with lower cell speeds—show a convex curve (blue circles in Figure 4.1(e)). Since radial velocity is the component of cell motion that contributes to the collective expansion of the monolayer, the change in curve shape suggests changes in the collective behavior of the cell sheet. In those cases with lower overall cell speed, the cells near the center of the monolayer

move in all directions. Since radial velocity can be positive or negative, these values average out to near zero in the center region. In the cases with higher overall speed, however, cells throughout large regions of the cell monolayer contribute to the overall expansion.

To explore how individual cell properties affect the qualitative, large-scale changes seen in this data set, we compare the experimental results to simulations using a previously published model [16, 128, 129]. In this model, each cell is represented by two particles that move according to the forces acting upon them (shown schematically in Figure 4.2(a)). These forces, further detailed in the Methods section, include friction forces, motility forces, cell-cell interaction forces, and a force representing cell growth. Cell division is initiated once the distance between the particles exceeds a threshold. Cells can be either motile or non-motile, and the transition rate between these two states is chosen such that motile cells tend to align their motility force (the force that pushes a cell in a preferred direction) with their velocity.

Simulated monolayers in this model using the standard parameters (see Section 4.5.3) and in the absence of leader cells show a radial expansion similar to the MCF10A experimental system, and have increased speed near the edge of the monolayer (see Figure 4.2(b), black curve). Simulations with the standard parameter set also show an increased radial velocity near the leading edge of the cell sheet and a concave radial velocity profile in the center of the cell monolayer (Figure 4.2(c), black curve), similar to the experimental results with faster cells (Figure 4.1(c), black curve).

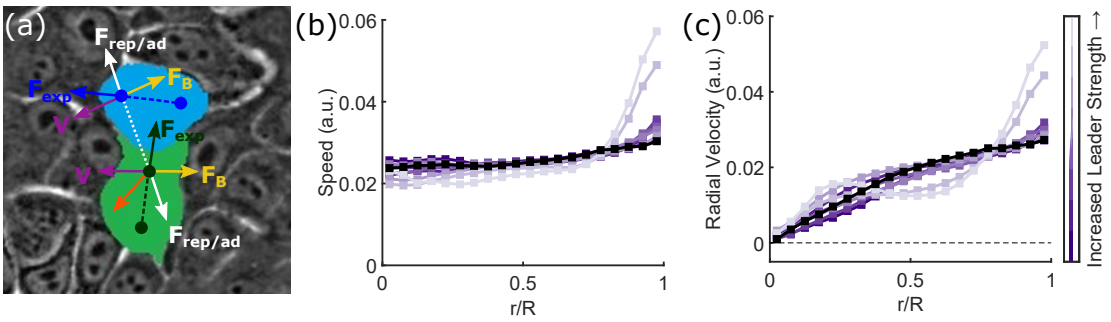

Figure 4.2: Multiple forces act on the simulated cells (a). Each cell is composed of two particles, which feel a cell expansion force (F_{exp}). The particles also have a velocity (V) and experience friction between the cell and substrate (F_B). Cells interact through a force that is repulsive at short distances and attractive at intermediate distances ($F_{rep/ad}$). Cells may be in a sleep state (a, blue cell) or awake state (a, green cell). Only awake cells experience a motility force (m) that provides a preferred direction of motion. Particles also experience friction and noise forces that are not shown. Simulated cells show a similar speed profile to the experimental results; the addition of leader cells increases the speed at the edge of the monolayer (b). Simulated leader cells increase radial velocity but do not cause the qualitative change in radial velocity seen experimentally (c). From dark purple to light purple, k_{Rm}—which controls the leader cell strength—is set to 0.01, 0.05, 0.1, 0.25, 0.5, 1, 5, 10, whereas the black curve represents the standard simulation set in with no leader cells, $k_{Rm} = 0$ (b,c).

In a first computational test, we explore whether introducing an active subpopulation of cells near the edge, leader cells, may be sufficient to cause the experimentally observed change in velocity profile shown in Figure 4.1. These leader cells are included by making the transition rate between the motile and non-motile state of motion dependent on the spatial location of the cell (see Section 4.5.3). As seen in Figure 4.2(b), increasing the strength of this leader cell effect can lead to increased speeds near the monolayer edge. However, this increase is not accompanied by a qualitative change from concave to convex radial velocity profiles (Figure 4.2(c)),

suggesting that another mechanism is responsible for the experimentally observed change in the radial velocity profiles. At high leader cell strengths, the profile does qualitatively change in that it shows a flat profile in part of the sheet, but this is due to an instability of the boundary shape which forms fingering structures at the leading edge.

We next hypothesized that the proliferation rate may affect the phenotype. Changing proliferation rates in our simulations, however, does not change the simulated speed profile (Figure 4.3(b)) or radial velocity profile (Figure 4.3(c)). We should note that for low proliferation rates (less than 10% of the standard parameter value for division) the monolayer begins to break apart (see Figure 4.4). In this case, the cell sheet can no longer be fit to a circle for radial analysis. The dissociation of the monolayer at low proliferation rates agrees with a hypothesis that cell proliferation is used to fill in the gaps left by a migrating monolayer rather than as a mechanism for pushing migration forward [60, 61].

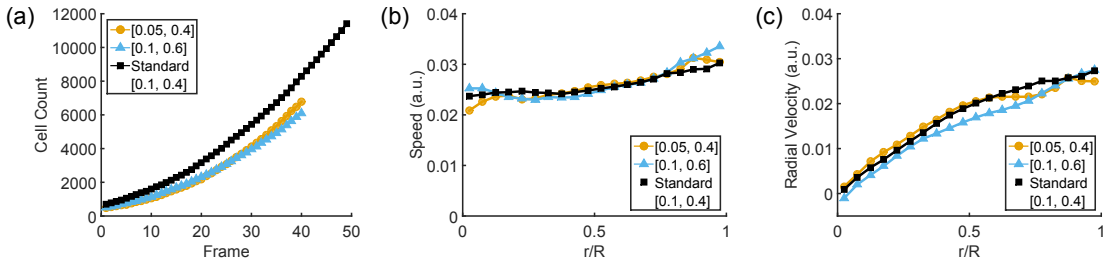

Figure 4.3: Changing the proliferation rate leads to a slower increase in cell number (a), but does not have a clear effect on speed (b) or qualitatively change the radial velocity profile (c). Legend pairs indicate $[k_{div}, R_{div}]$ parameter values.

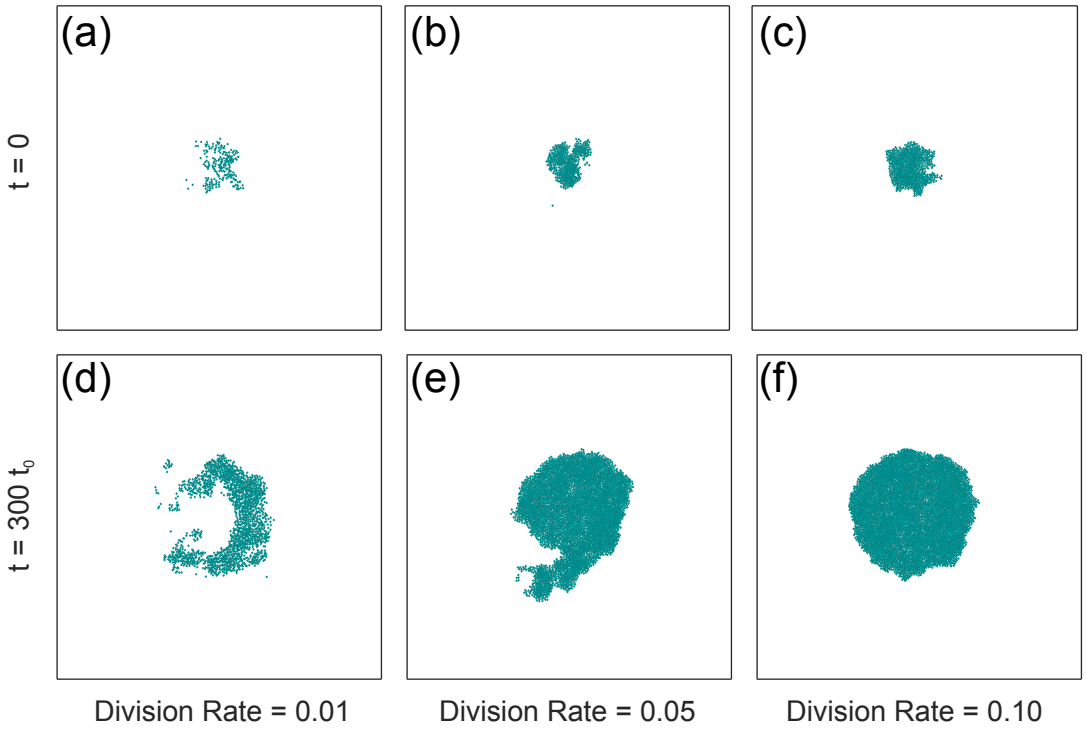

Figure 4.4: Snapshots of simulated cell monolayers at frame 0 (a-c) and frame 200 (d-f) of the motion analyzed frames of the simulation. The columns from left to right show increasing division rates with (c,f) corresponding to the standard division rate of 0.1. At the lowest rate of 0.01, the monolayer no longer remains circular or confluent.

In a third set of computational trials, we determined how changes in the 'wake rate' parameter, which controls how often cells become motile, affect velocity profiles. It may be expected that cases of reduced speed in the experimental data correspond to decreased activity in the cells. Our simulations reveal that decreasing the wake rate leads to an overall lower speed (Figure 4.5(b)) and, as shown in Figure 4.5(c), a qualitatively different radial velocity profile. Specifically, decreasing the wake rate leads to a transition from behavior in which cells across the radius of the monolayer move outward, showing radially expanding motion, to a state in

which only those cells near the edge move cooperatively outward. As a result of this transition, the radial velocity profile changes from a concave one to a convex one consistent with the experimentally observed changes in radial velocity.

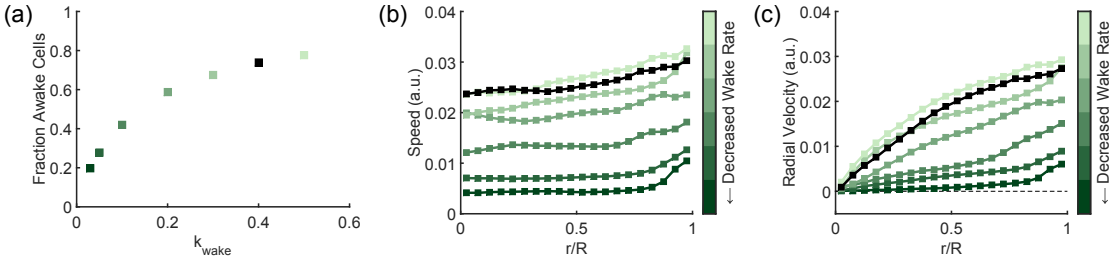

Figure 4.5: Changing the wake rate parameter (k_{wake}) decreases the fraction of the cell sheet that is awake at any given time (a) and decreases the overall mean speed while maintaining a similarly shaped curve (b). Decreasing the rate at which non-motile cells wake causes a transition from a concave to a convex radial velocity curve (b). Wake rate parameter values (k_{wake}) are 0.03, 0.05, 0.1, 0.2, 0.3, 0.5 from dark green to light green, with the standard wake rate of 0.4 shown in black.

We next determined how the coupling between the cells' velocity and motility force, parameterized by k_{mv}, affects the velocity profiles. This alignment coupling leads to higher sleep rates for cells that have velocity and motility forces pointing in opposing directions. Interestingly, if the coupling between the motility force and velocity is removed the simulations always show convex radial velocity profiles, even for large values of the wake rate (Figure 4.6(b)). This finding suggests the strength of this coupling may also play a role in the migration. Indeed, using otherwise standard parameters but decreasing the strength of the coupling between velocity and motility can cause a transition from a concave to a convex radial velocity curve (Figure 4.6(d)). Thus, causing each cell to have strong alignment between its

motility direction and its current velocity leads to more active behavior, whereas motility that is not strongly coupled leads to velocity profiles similar to those seen in the less active experiments.

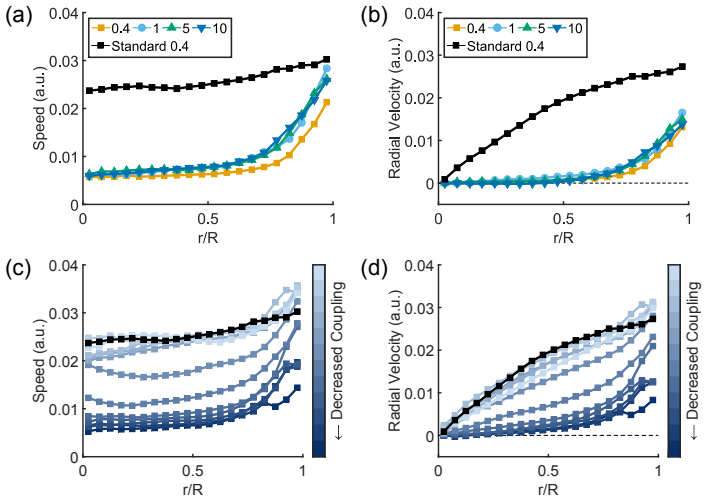

Figure 4.6: If velocity-motility coupling is removed, changing the wake rate cannot capture the experimentally seen results. Speed profiles are shown in (a) and radial velocity profiles in (b) with the k_{wake} value shown in the legend. The standard parameter set with $k_{wake} = 0.4$ and motility coupling implemented is shown in black. Speed increases (c) and radial velocity (d) undergoes a qualitative change as the coupling is increased which is similar to the change seen in the MCF10A experiments; from dark blue to light blue the coupling parameter k_{mv} is set to 0.1, 0.05, 0.04, 0.035, 0.03, 0.025, 0.02, 0.015, 0.01, 0.005, 0.001, and 0.0001. The standard k_{mv} value of 0.00001 is shown in black. Smaller values of k_{mv} indicate a stronger coupling strength.

To probe further the changes in collective behavior that may accompany the observed changes in radial velocity, we calculate velocity correlations in the region between the center and the edge of the monolayer ($0.5 < r/R < 0.75$). This range was chosen to correspond to the region in which we see experimental changes in the radial velocity profile. As shown in Figure 4.7(a), those conditions with

decreased speed and convex radial velocity correspond to cases of less correlated motion within the cell sheet. To determine whether this result is consistent with our model, we compute the spatial correlation in our simulated trials. We focus on the perturbations—reducing the wake rate and decreasing the motility-velocity coupling—that are able to reproduce the qualitative change in radial velocity profiles. We find that both decreasing the wake rate (Figure 4.7(b)) and decreasing the coupling (Figure 4.7(c)) results in a reduction of the spatial correlation that is consistent with the experimental results.

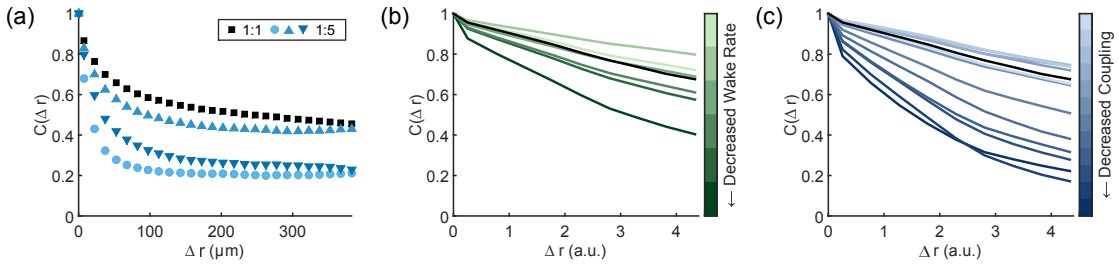

Figure 4.7: In the case of decreased experimental speed (a), decreased wake rate (b), and decreased coupling (c), the cells are less correlated in their motion. All figures show time-averaged velocity correlations (see Section 4.5.2) in the transition region, defined as $0.5 < r/R < 0.75$. Wake rate parameter values (k_{wake}) in (b) are 0.03, 0.05, 0.1, 0.2, 0.3, and 0.5 from dark green to light green. From dark blue to light blue in (c), the coupling parameter k_{mv} is set to 0.1, 0.05, 0.04, 0.035, 0.03, 0.025, 0.02, 0.015, 0.01, 0.005, 0.001, and 0.0001. Smaller values indicate a stronger coupling strength. The standard parameter set ($k_{wake} = 0.4$ and $k_{mv} = 0.00001$) is shown in black in (b,c).

4.4 Discussion

Here we provide insight into the single-cell behavior underlying collective migration by comparing experimental data to a model of collective migration. The emergent behavior of collective cell sheets that results from changing the properties of individual cells is difficult to predict and to probe experimentally. To investigate the connection between individual and collective behavior, we use PIV-based migration data to measure motion that spans a wide variety of scales. The length scales studied vary from that of a single cell to a monolayer composed of thousands of cells. By comparing simulation and experiment across these scales, we provide insight into collective behavior changes observed in epithelial MCF10A cells. Cells moving at higher speeds show a larger region of radial expansive motion than do slowly moving cells (Figure 4.1), suggesting changes in collective behavior.

Although leader cells may play an important role in epithelial sheet migration, we show here that they are not necessary to recapture large-scale changes in collective migration (Figure 2). We also show that changes in proliferation are unlikely to be the cause of the observed large-scale changes (Figure 4.3). Experimental changes in activity can be compared to the wake rate in the simulations. This parameter is related to the simulated cells' ability to switch between a non-motile and motile state. Here we find that changes in the wake rate can lead to the experimentally observed changes in collective behavior (Figure 4.5).

Interestingly, changing the wake rate has no effect without implementing alignment coupling between the cells' motility and velocity (Figure 4.6). In this model,

alignment coupling is implemented such that cells with misaligned motility and velocity vectors are more likely to transition to a non-motile state. The motility force gives the cells a preferred direction of motion, and in that sense, it can be viewed as a biomechanical cell polarity. The ability to align this biomechanical polarity with the direction of motion of a cell indicates that a cell is able to sense resistance to motion and adapt its biomechanical machinery to push in a direction in which the cell is actually able to move. Thus, the strength of this coupling indicates how sensitive a cell is to its mechanical environment, and it is not surprising that changing this motility to velocity coupling changes the collective behavior of the cells (Figure 4.6). We further find that the increased region of radial expansion found for higher cell speeds is accompanied by increased correlations (Figure 4.7).

Ultimately, the motility coupling strength provides a simple sensor of the surrounding tissue and leads to cells that are best able to follow a path of least resistance, because increased motion along the path of least resistance will lead to feedback with alignment of the motility force. Changing this coupling strength can cause large-scale changes in cell migration without explicitly changing the interactions between neighboring cells or invoking leader cells. Increasing activity within the cell sheet has a similar effect since it gives the cells more opportunities to be motile at the same time and thus follow other cells on paths of least resistance. When combined with a strong sense of polarity, this activity can then lead to increasing cooperativity over time because the cells have more opportunities to align their motion.

We thus find in our simulations that the emergent behavior of a simple model

system can explain large-scale changes in collective behavior without the need to specify large-scale features explicitly. We identify cell activity and the coupling between biomechanical polarity and motion as two interesting features of individual cell behavior that can lead to large-scale collective behaviors. Our study demonstrated that PIV measurements may be used in conjunction with simulations to infer detailed biomechanical single cell phenotypes from the types of collective migration assays that are commonly used in drug discovery and cancer research.

4.5 Materials and Methods

4.5.1 MCF10A Data Set

We analyze a previously published set of time-lapse images of MCF10A (breast epithelial cells) migrating in collective sheets [117]. These cells migrate on a glass surface coated with collagen IV, and phase-contrast images were taken every three minutes for a total of 1000 minutes (16.6 hours). The data set includes cells migrating in normal cell-culture medium (referred to as 1:1) and cells migrating in a dilution of this culture medium (referred to as 1:5). This change decreases the horse serum, insulin, EGF, hydrocortisone, and cholera toxin concentrations to 20% of their full media values (e.g. horse serum at a concentration of 1% instead of 5%).

4.5.2 Migration Analysis

Phase-contrast images were analyzed with Particle Image Velocimetry (PIV) using the MatPIV toolbox (J. Kristian Sveen, GNU general public license) for MAT-

LAB (MathWorks, Inc.). Multiple iterations of interrogation window sizes were used: two iterations of 64 x 64 pixel windows were followed by two iterations using 32 x 32 pixel windows. At each interrogation step a 50% overlap was used; outliers were detected using a signal-to-noise threshold of 1.3.

Custom MATLAB segmentation code was used to find the leading front of the cell monolayer. The phase-contrast images were Sobel filtered followed by median filtering and morphological opening to clean the binary image before finding the perimeter of the objects in the image. The edge coordinates were then found using a MATLAB implementation of Dijkstra's algorithm ("dijsktra path finder" by Sebastien PARIS, available on the MATLAB File Exchange at mathworks.com). In combination with the microscope stage positions, this edge was used to fit the cell monolayer to a circle. The effective radius of the monolayer and the center position were used to define regions of the cell monolayer for later migration analysis. Speed and radial velocity values were averaged over theta to create radial profiles of motion.

Velocity correlations were calculated as:

$$C(\Delta r) = \frac{< \vec{v}(r) \cdot \vec{v}(r + \Delta r) >}{< v(r) >< v(r + \Delta r) >} \tag{4.1}$$

In this case $\vec{v}(r)$ is the velocity at a location r within the cell sheet. The correlation values are averaged over all r within the region $0.5 < r/R < 0.75$. In this equation and throughout, r refers to the location within the cell monolayer with respect to the monolayer center and R refers to the size of the monolayer.

4.5.3 Simulations

Our model is based on earlier work [16, 129] and includes cell growth and division, motility forces, friction forces, and volume exclusion and adhesion between neighboring cells, as shown in Figure 4.2(a). In the model, two point particles represent a single cell with a size given by the inter-particle distance r. The equation for motion for each particle is given by

$$\frac{d\vec{p}}{dt} = \vec{m} + \vec{F}_{exp} + \vec{F}_{int} + \vec{F}_B + \sum_{r \leq R_{cc}} (\vec{F}_{rep/ad} + \vec{F}_{df}) \tag{4.2}$$

Here, $\vec{m}$ is the motility force (discussed further below) and its value, along with all other parameter values, is given in Table 4.1. Cell growth is simulated through a repulsion force $\vec{F}_{exp} = -B/(r+1)^2\hat{r}$ where B is an expansion factor and $\hat{r}$ is the unit vector parallel to the line connecting the two particles. Cell division is incorporated as follows: after the cell size reaches a threshold R_{div}, it divides at a constant rate k_{div}, after which two new particles are placed a distance r_{div} away from the particles constituting the old cell. $\vec{F}_{int}$ represents the intracellular friction force between particles constituting the same cell and is determined by the coefficient ξ_{int}. Cell-substrate friction is assumed to be proportional to the cell velocity, resulting in $\vec{F}_B = -\xi_B\vec{v}$. The last two forces in the equation of motion act only within a distance of $r \leq R_{CC}$ and represent volume exclusion and adhesion of cells ($\vec{F}_{rep/ad}$) and friction forces that oppose the relative motion of cells with a friction coefficient ξ_{df} ($\vec{F}_{df}$). Details of the latter can be found in Basan et al. [129]. The former has two terms: a short-range repulsive term, which prevents cell-cell overlap and is

Table 4.1: Standard Value of Simulation Parameters

Parameter	Value	Unit	Description
m	1.2	$p_0 l_0^2$	Magnitude of motility forces
k_1	0.1	t_0^{-1}	Minimal transition rate to non-motile state
k_0	0.3	t_0^{-1}	Maximal transition rate to non-motile state
k_{wake}	0.4	t_0^{-1}	Transition rate to motile state
f_0	2.4	$p_0 l_0^2$	Repulsive cell-cell potential coefficient
f_1	1.0	$p_0 l_0^2$	Attractive cell-cell potential coefficient
R_{CC}	1.0	l_0	Range of pair potentials and dissipative forces
B	5.0	$p_0 l_0^4$	Cellular expansion coefficient
R_{exp}	0.8	l_0	Range of intracellular expansion force
R_{div}	0.4	l_0	Threshold distance for cell division
r_{div}	0.01	l_0	Distance of new particles after division
k_{div}	0.1	t_0^{-1}	Division rate for cells surpassing size threshold
ξ_{int}	50.0	$p_0 l_0 t_0$	Intracellular dissipation
ξ_{df}	50.0	$p_0 l_0 t_0$	Intercellular dissipation
ξ_B	10.0	$p_0 l_0 t_0$	Background friction coefficient
M	1.0	$p_0 l_0 t_0^2$	Mass of particles
τ	5.0	t_0	Relaxation time for velocity averaging
k_{mv}	10^-5	$p_0 l_0^3 t_0^{-1}$	Sharpness of k_{sleep} dependence on alignment
k_{Rm}	0	$p_0^{-1} l_0^{-3}$	Strength of leading cells at the edge

parameterized by f_0, and a long-range adhesive force with a strength determined by f_1. The equation for volume exclusion and adhesion is of the form:

$$\vec{F}_{rep/ad} = -(f_0(1/r - 1) - f_1)\hat{r} \tag{4.3}$$

The orientation of the motility force $\vec{m}$ is such that it tends to align with the cell's velocity $\vec{v}$. Specifically, this motility-velocity alignment coupling is implemented by assuming two states of the cell: a motile state and a non-motile state. Cells in the non-motile state exert no motility force while cells in the motile state generate a motility force with a fixed magnitude in a random direction. The transition from the non-motile state to the motile state is determined by a constant rate k_{wake} by generating a motility force with a fixed magnitude in a random direction.

The transition rate from the motile state back to the non-motile state depends on the motility-velocity alignment, quantified by $\vec{m} \cdot \vec{v}$. In Basan et al. [16] this transition rate could take on only two values: low for aligned cells ($\vec{m} \cdot \vec{v} > 0$) or high for non-aligned cells ($\vec{m} \cdot \vec{v} < 0$). This bias results in a higher ratio of aligned cells versus non-aligned cells in the motile state and provides an alignment mechanism. In this study, we use a continuous form of the transition rate to the non-motile state that depends on the degree of alignment:

$$k^{'}_{sleep} = (k_0 - k_1)(1 + \tanh(-(\vec{m} \cdot \vec{v})/k_{mv}))/2 + k_1 \tag{4.4}$$

This rate ranges from k_1 for aligned cells to k_0 for non-aligned cells while the transition between these two rates is determined by k_{mv}; when $k_{mv} << |\vec{m}||\vec{v}|$ the transition rate approaches the aligned and not-aligned binary case of Basan et al. [16].

Our transition rate was further modified to account for the effect of leader cells, i.e., cells near the edge of the colony that preferentially move outward. To this end, we multiplied the above transition rate by a spatially-dependent prefactor, so that the final form for particle i is $k_{sleep} = \exp(k_{Rm}\vec{m}_i \cdot \vec{R}_i)k^{'}_{sleep}$. Here $\vec{R}_i$ is a spatial average of the particles neighbors: $\vec{R}_i = \sum_{neighbors} \vec{r}_{ij}$, where $\vec{r}_{ij} = \vec{r}_j - \vec{r}_i$ is the relative position of cells i and j. The parameter k_{Rm} determines the strength of the leader cell effect. Neighbor cells are defined as cells within the range of nonzero cell interactions, i.e., $r \leq R_{CC}$. Cells far from the edge are surrounded by other cells such that $R \approx 0$ and the prefactor is close to one. Cells near the edge, however, have only neighbors inside the colony, resulting in a value of $\vec{R}$ that points inward. Consequently, k_{sleep} is smaller for cells near the edge that have their motility vector

pointing outwards, leading to "leader" cells that move outward. In the standard set of parameters (see Table 4.1) , $k_{Rm} = 0$ and there is no leader cell effect.

Simulations were initiated with 100 cells and the first ten frames of the simulated data were discarded before migration analysis to remove artifacts from low cell number monolayers. Particle positions and velocities were interpolated to a grid to compare to experimental PIV results. The edge of the simulated monolayer was found based on the particle positions and fit to a circle. As with the experimental results, this edge was used to define radial regions of the monolayer and to create profiles of speed and radial velocity. Migration analysis was then carried out in the same manner as previously described for the experimental data.

We should note that the length scale of the model, l_0, can be related to experimental values by comparing it to the experimental division size. In our simulations, we choose the threshold distance for cell division to be $0.4l_0$. This distance should be of the same order of magnitude as the average cell size, which is approximately $40\,\mu m$, resulting in $l_0 \approx 100\,\mu m$. The simulation time can then be determined by comparing the mean speed of cells in the simulation ($\approx 0.025 l_0/t_0 = 2.5\,\mu m/t_0$) to the mean speed in the experiment ($\approx 0.25\,\mu m/\,min$) which leads to $t_0 \approx 10\,min$. We can then verify that the relative growth rate in the simulation is consistent with the relative growth rate observed in the experiments, as shown in Figure 4.8.

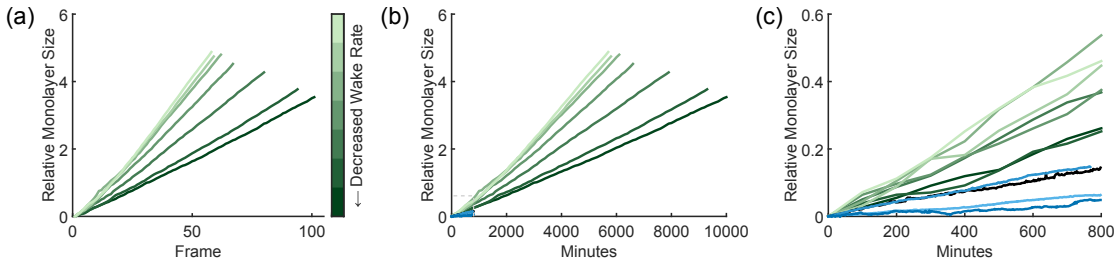

Figure 4.8: Monolayer size is plotted with respect to the initial frame ($R_{relative}(t) = (R(t) - R(0))/R(0)$). The simulated monolayers (a) grow linearly as time increases. Each frame of the experiment is two minutes long; the frames of the simulation are $10t_0$ (see Figure 4.9), which can be converted to a time scale of approximately 100 min. The monolayer growth in both experiment and simulations is shown in a (b); the region indicated by a dashed gray line is enlarged in (c). Wake rate parameter values are 0.03, 0.05, 0.1, 0.2, 0.3, 0.4, and 0.5 from dark to light green.

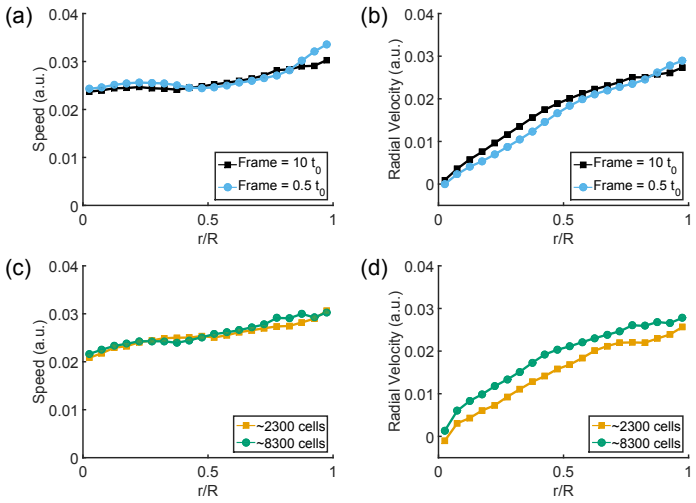

Figure 4.9: In Section 4.3, the simulation output is saved every $10t_0$. To look at motion on a smaller time scale, we show speed (a) and radial velocity (b) for data recorded every $0.5t_0$, which shows the same qualitative curve shape. To compare the effect of monolayer size, we compare curves considering 10 frames of data at different cell numbers. Speed (c) and radial velocity (d) are shown for time ranges with an average of 2300 and 8300 cells, which show similar curves.

Chapter 5: Metrics for Understanding Collective Migration

This chapter is adapted from Lee, Kelley, Nordstrom, Ouellette, and Losert [117]. Text and figures are reproduced here with permission. Douglas Kelley performed the finite-time Lyapunov analysis, and Kerstin Nordstrom performed the D^2_{min} analysis. Rachel Lee performed the MCF10A experiments and the rest of the data analysis.

5.1 Overview

Although understanding the collective migration of cells, such as that seen in epithelial sheets, is essential for understanding diseases including metastatic cancer, this motion is not yet as well-characterized as individual cell migration. Here we adapt quantitative metrics used to characterize the flow and deformation of soft matter to contrast different types of motion within a migrating sheet of cells. Using a finite-time Lyapunov exponent (FTLE) analysis, we find that in spite of large fluctuations, the flow field of an epithelial cell sheet is not chaotic. Stretching of a sheet of cells (i.e., positive FTLE) localizes at the leading edge of migration and increases when the cells are more highly stimulated. By decomposing the motion of the cells into affine and non-affine components, we quantify local plastic rearrangements and

describe the motion of a group of cells in a novel way. We find an increase in plastic rearrangements with increasing cell densities, whereas inanimate systems tend to exhibit less non-affine rearrangements with increasing particle density.

5.2 Background

Collective motion at the cellular level plays an important role in many biological processes. From development [20, 130] to wound healing [61, 69, 131], cells must cooperate to create complex structures. Faulty regulation of collective behavior can disrupt development or lead to diseases such as metastatic cancer [24, 47, 132, 133]. Despite the abundance of collective migration in biological systems, such migration is not yet as well-characterized as individual cell movement.

One way to begin to understand how collective behavior emerges from individual motion is to make analogies to non-biological physical systems. For instance, the migration of a group of cells calls to mind images of flowing fluids or sheared solids. Cells' active properties, however, allow the group to move in ways that are distinct from inanimate physical systems. Current research has begun to look for similarities and differences between active cells and passive physical systems by exploring the stresses the cells experience [72, 93, 132, 134–136] and the cell-cell/cell-matrix adhesions that hold sheets of epithelial cells together [131, 133, 137–140]. The changes seen in migration as cells reach different densities [71, 141] have also motivated comparisons to kinetic phase transitions [77, 142]. Continued application of physical tools to groups of cells will undoubtedly reveal interesting features of migration—

both those that are shared with inanimate systems and those that are unique to active, living matter.

One particularly interesting physical feature of collectively migrating cells is their velocity field. Velocity fields have long been studied in physical systems such as fluid flows or granular systems. By applying techniques developed to study physical velocity fields to the information present in live-cell imaging, we have developed tools to quantify the speed, density, and rearrangement of epithelial sheets during collective cell migration.

One way to extract velocity information from live-cell images is particle image velocimetry (PIV). This technique—originally developed to study fluid flows—has started to see use in biological systems (see for example the work by Petitjean et al. [86]). PIV estimates the average flow field from one image to the next by correlating the two images, but unlike cell tracking, does not provide information about individual cell motion. PIV analysis is easy to carry out on phase-contrast images and provides a smoothed flow field that describes the overall motion of the migrating sheet. Because PIV assesses the average motion of all features visible in an image, it takes into account all components in the cell. A second common technique for extracting velocity information is tracking each cell's nucleus. Although PIV can be applied to both fluorescent and phase-contrast images, tracking generally relies on fluorescent images. Techniques for tracking objects in phase-contrast images, however, are steadily developing [143].

To determine the stretching rate of the flow field determined using PIV analysis, we use finite-time Lyapunov exponents. The FTLE is a measure of how much

two points initially near each other in the flow field separate after a given time interval [103, 104, 144]. Similar to the traditional Lyapunov exponent, which quantifies separation on an asymptotic time scale, the average FTLE reflects how chaotic the flow is within a finite time (in our case, we choose a time scale over which the cells move roughly one cell length). Measuring an FTLE field reveals spatial information regarding which regions are more or less chaotic. This information allows us to assess whether the chaotic features of the flow field are correlated with a cell's distance from the leading migration edge or with other spatially localized features.

The tracks give information about individual cells; by combining PIV data with individual cell tracks we can consider the motion and flow of the migrating epithelial sheet. To parameterize an individual cell's deviation from the motion predicted by the average flow field, we use the previously defined parameter D^2_{min} [97, 100, 102, 145, 146], which quantifies the non-affine deformation around a given cell. A cell with a high value of D^2_{min} moves in a distinct manner compared to what is predicted by the smooth local flow field. Regions in the sheet with high D^2_{min} can be considered regions of high rearrangement.

To illustrate the use of these two metrics, we analyze a migrating two-dimensional culture of epithelial cells. We find that statistics such as average speed vary from experiment to experiment even under the same conditions. By considering our metrics for rearrangement and stretching, however, we are able to quantify trends that hold across different experiments. We find that despite the radial migration of our monolayer, most of the stretching of the sheet is limited to a small region near the leading migration edge. We also find that localized rearrangements within our cell

sheet increase as the local cell number density increases, which is a surprising trend that could be used to isolate active properties of the migrating cells. These results suggest that D^2_{min} and FTLE data will be useful in distinguishing and classifying how cells migrate collectively in many different systems under varying conditions, which make this analysis a promising tool for future cancer studies.

5.3 Results

Cells were added to collagen-coated coverslips so as to form a roughly circular monolayer of cells (see Figure 5.1 for a schematic of the assay). Time-lapse images were acquired at multiple locations of the dot; some were within the bulk, and others were at the leading edge. Both PIV and tracking of cell nuclei showed significantly higher speeds for cells near the leading edge of the monolayer, as shown in Figure 5.2(a). That the tracking shows a slight increase in mean speed compared to PIV is to be expected from the properties of the methods. PIV gives a smoothed velocity field that suppresses the contribution of isolated fast motion to the overall mean speed. PIV also measures all motion between two frames, including membrane and cytoplasm fluctuations in addition to the nuclear motion; this randomly directed motion may lead to smaller average speeds. Nuclear tracking, however, follows each cell's nucleus individually and retains information about isolated outliers. The two methods capture different aspects of the system and thus provide slightly different information.

In the case of PIV, dividing cells and the few visible dead cells are included

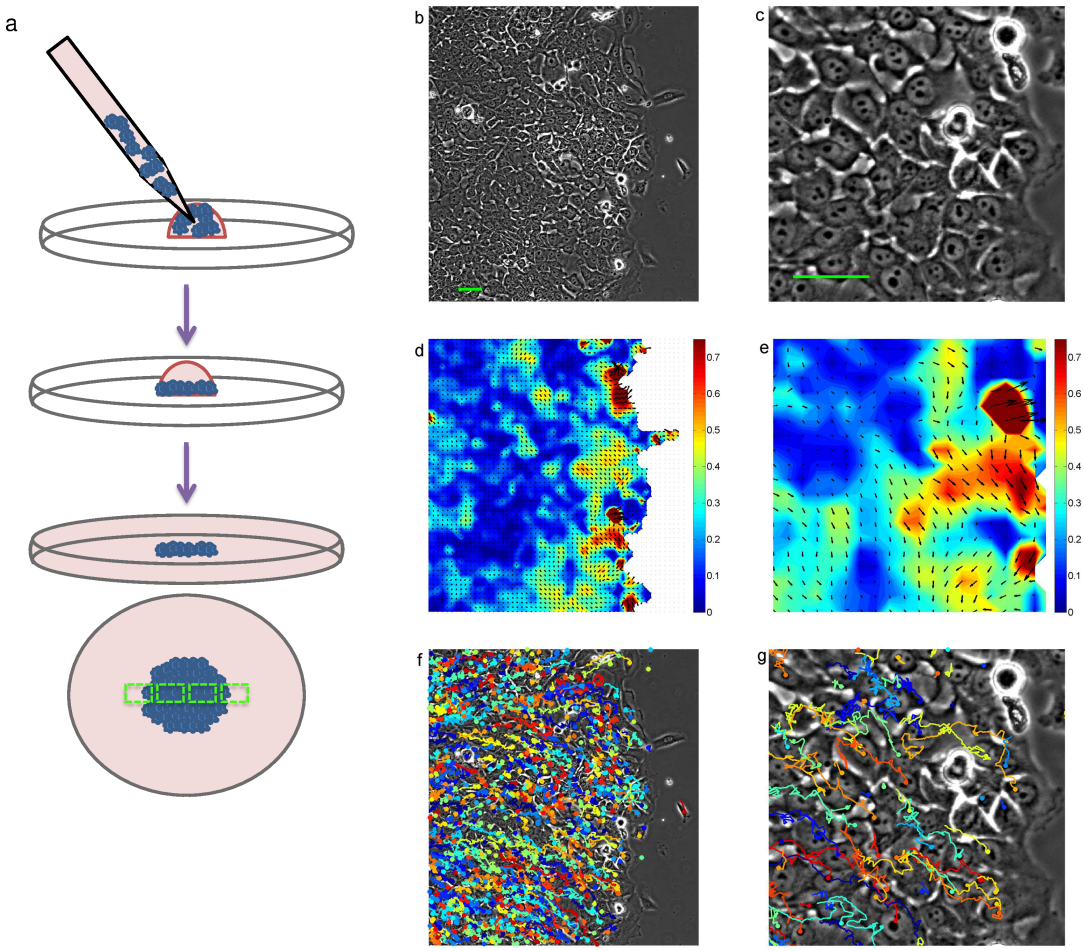

Figure 5.1: (a) Cartoon of migration assay. Cells were plated in a 2 µl drop and allowed to adhere the collagen surface before the well was filled with medium. (b, c) Phase-contrast image of leading edge of cell migration (scale bar, 50 µm). (d, e) Velocity field from PIV analysis. The color map represents the speed (µm/ min) and is overlaid with velocity vectors. (f, g) Example of particle tracking overlaid on phase contrast image. Current particle positions are marked with a circle and the previous positions of the cell are marked by a track of the same color.

in the velocity information. In contrast, tracking does not include dead cells and is only able to measure dividing cells while the tracked features (nucleoli) are visible during the beginning and end of the division process. In a subset of movies, cell divisions were tracked and showed no correlation with changes in either speed metric (data not shown).

Despite the agreement among all experiments on the overall trend between edge and bulk, a wide variation in speeds was observed from day to day. As shown in Figure 5.2(b), the mean speeds from one experiment are significantly higher than the other two experiments. Although all three experiments show a significant increase in that day's edge speed compared to the same day's bulk speed, the bulk cells from experiment C move as quickly as the edge cells from experiments A and B. The variation in speed could result from sensitivity to initial conditions such as small differences in the coating of a microscope slide. The authors' experience with migration assays suggests that small variations in these parameters and variation in speeds are frequently observed. The results shown in Figure 5.2(b) emphasize that it is important to be careful when comparing experiments performed on different days and suggest the need for additional quantitative metrics when comparing the dynamics of epithelial sheet migration.

5.3.1 Finite-time Lyapunov Exponents

Figure 5.3 shows an example snapshot of FTLE values. We find that the spatial average of FTLEs is negative in all cases and that it approaches zero as

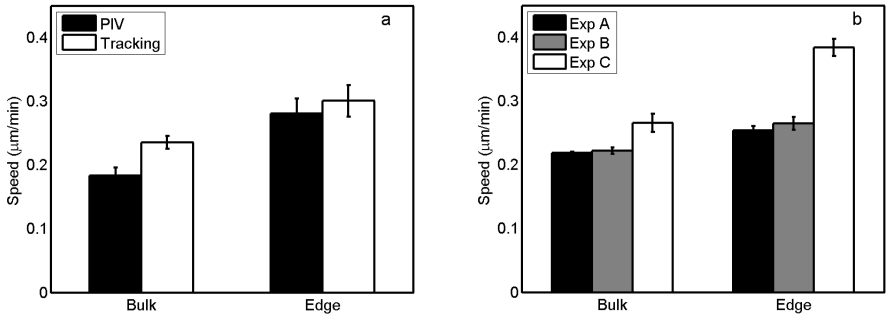

Figure 5.2: (*a*) A comparison of the mean speeds between the bulk and edge movies highlighting the distinction between PIV and nuclear tracking (composite data from three experiments). (*b*) A comparison of the mean speeds from tracking highlighting the variability between experiments. Error bars represent 95% confidence intervals.

the deformation time T increases. Negative FTLEs imply that the flow is not chaotic and that neighboring regions tend to separate only slowly as time passes. Slow separation is consistent with the fact that the majority of our observations show bulk cells surrounded by many neighbors, so their relative motion is highly constrained. The resolution of our data, however, prevents the FTLE calculations from accounting for length scales smaller than the PIV grid; the flow may be chaotic at these small scales.

By fixing the deformation time at $T = 80$ min we can consider FTLE fields in more detail as shown in Figure 5.4. Distributions of FTLE magnitude show that local values can vary substantially from the mean and are occasionally greater than zero. Positive FTLEs are more common in data sets recorded at the advancing edge of a cell culture than those recorded in the bulk, as indicated both by distributions and by snapshots—the edge experiences large stretching. This observation is borne

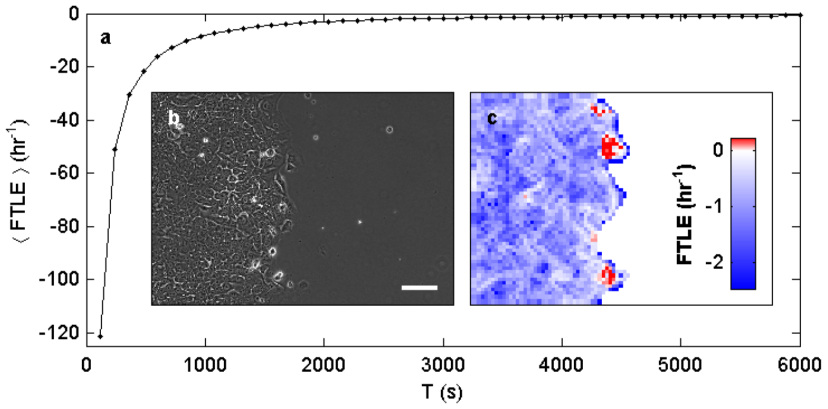

Figure 5.3: (a) Spatial mean of the FTLE field, varying with deformation time T. (b) A single phase-contrast image, along with (c) the corresponding FTLE field. The scale bar is 100 µm.

out in FTLE statistics conditioned on the normalized radius r/R (as shown in Figure 5.6(c)).

Many simple flows are chaotic, regardless of the flow speed [103, 104], so the lack of chaotic motion is not solely due to the relatively slow speed of the migrating sheet. In fact, the chaos measured in the sheet is changed with modifications to the migration environment, as shown by the 5% serum data in Figure 5.4. Serum contains many compounds, including growth factors and other stimulants, which can change the sheet's mode of migration. The change in migration activity is seen in the shift toward more chaotic motion in the bulk FTLE distributions (Figure 5.4(a)) and even more dramatically in the distribution of edge FTLE values (Figure 5.4(b)). Although in all cases the mean FTLE remains negative, and thus not chaotic, in the spatial information provided by the FTLE field we find instances of positive values, i.e., chaotic motion. Although the speed of the sheet was moderately increased by

the addition of serum (Figure 5.6(b)), the relative number of positive values was increased many-fold in migration at higher concentrations of serum (Figure 5.4(c)). The more active motion provided by the stimulation at 5% serum is reflected in the increased instances of chaotic motion.

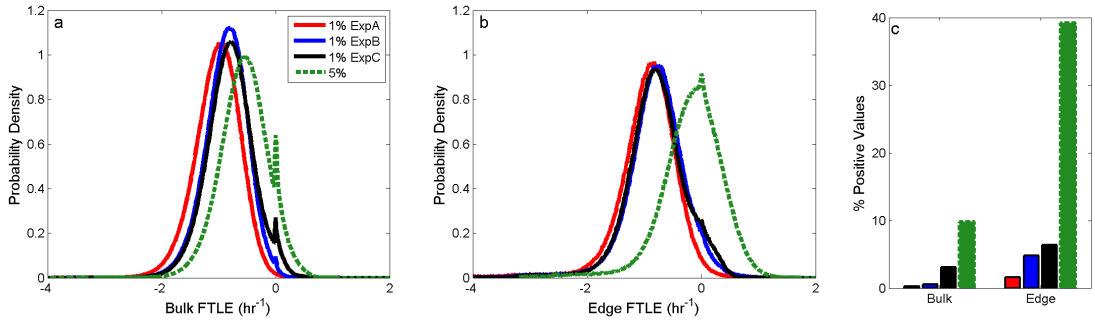

Figure 5.4: Probability densities of FTLE fields for measurements in the bulk (a) and at the edge (b), with multiple solid lines representing average results from 3 different days of experiments with 1% horse serum compared to the more chaotic distributions seen in a set of migration experiments at 5% horse serum (dashed line). (c) Fraction of FTLE values which were positive (i.e., chaotic) for 4 different days of experiments. A higher concentration of horse serum corresponds to an increased instance of chaotic regions.

5.3.2 Non-affine Motion

D^2_{min} is a spatially and temporally heterogeneous quantity; 'hot spots' of plastic rearrangements appear and die out after the rearrangement is complete. Figure 5.5(a) shows these hot spots in one frame of a bulk movie. We look at the differences in D^2_{min} between the edge and bulk in Figure 5.5(b). D^2_{min} is normalized by the mean-squared displacement so that the magnitude of D^2_{min} is not dependent on the macroscopic flow speed. Clearly, cells in the bulk undergo more plastic

rearrangements than on the edge, and this trend holds for different experiments.

To investigate this result further, we also look at the probability density of D^2_{min} values for several different experiments, shown in Figure 5.5(c). D^2_{min} has units of area, so we have translated the x-axis into the corresponding length. We see two characteristic peaks in the distribution, one near 2 µm and one near 10 µm. The peak at longer lengths grows for the bulk data sets, suggesting that the primary mode of rearrangements changes in the bulk. The length scale associated with this peak is comparable to the cell size, suggesting that these are actual position-switching deformations.

We also stitch together data from the bulk and the edge to tease out the dependence of D^2_{min} on distance from the center, as shown in Figure 5.6(d). The basic trend shows that non-affine motion increases into the bulk and eventually plateaus. Because the cell density changes from bulk to edge, we next consider the dependence of D^2_{min} on density.

5.3.3 Density Effects

After measuring consistent bulk-versus-edge trends in our metrics and yet seeing a clear variability between experiments, we looked to the original images for variation in factors other than speed. We find apparent differences in the edge densities between experiments, prompting the comparison of our metrics to the local cell density. We calculated local cell density by counting the number of neighboring nuclei contained within a 40 µm radius of the cell nuclear location.

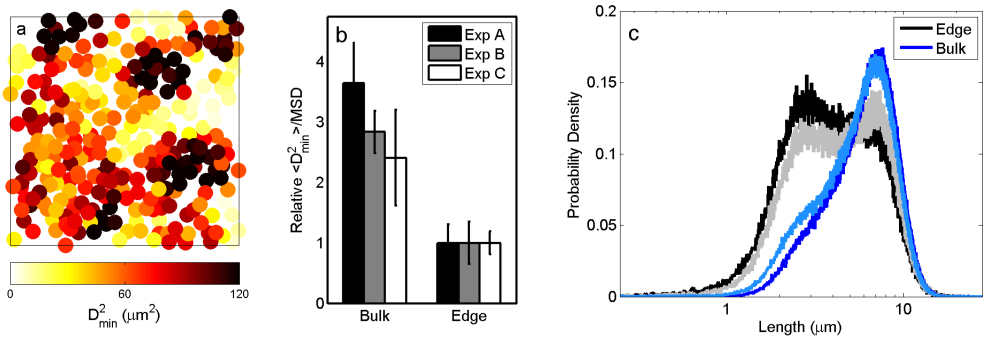

Figure 5.5: (a) A snapshot of individually tracked cells in the bulk, with each cell's value of D^2_{min} represented by the color. Regions of high rearrangement ('hot spots') are seen. (b) A comparison of mean D^2_{min} values between edge and bulk with values normalized by the mean square displacement. The variability between experiments is also shown. Error bars represent 95% confidence intervals. (c) A probability distribution of D^2_{min} values for two representative edge movies and two corresponding bulk movies. The relative weight placed on the two different peaks suggests a difference in the modes of rearrangement seen at the edge and in the bulk.

As seen in Figure 5.6(a), there is a clear distinction between the local neighbor count profiles for each experiment. These density differences are accompanied by variation in the radial speed profiles as seen in Figure 5.6(b). Within each day of experiments, four migration assays were performed. The density and speed trends were consistent across all four assays on a single day—speed decreased as density increased. For two of the days, a clear decrease in number density was seen near the leading edge of the migrating cells. This decreased is accompanied by a smooth speed profile, as shown by a nearly constant speed in the center that quickly increases to faster speeds at (the lower density) edge. For the third day (experiment C in Figure 5.6), all four migration assays show a density profile that differs from the other two experiments. For these monolayers, a peak in density is found $\approx 0.1R$ away from

the leading edge. This different density profile is accompanied by a different speed profile—faster overall, and lacking a constant speed in the center, as seen in Figure 5.6(b). This set of experiments also shows a perturbation in stretching (Figure 5.6(c)) and rearrangements (Figure 5.6(d)) near the relative position of the density perturbation.

Intrigued by the differences near this perturbation, we further investigated the relationship between our metrics and the local number density. To avoid including edge effects in our investigation of number density, we restricted our analysis to bulk movies. The number of neighbors within a radius of 40 µm of each cell is used as a measure of the local cell density. Figure 5.7(a) shows the relationship between cell speed and number density for three characteristic bulk movies. In all cases, although the magnitude of the speed varies from experiment to experiment, speed is a consistent function of density; cells in higher density regions are slower on average.

Although we investigated the relationship between FTLE values and local cell density, no strong trends were observed. As the FTLE analysis captures long-time deformation and stretching, it is not surprising that it does not show a significant relationship to short-time parameters such as the local cell density. Furthermore, because the stretching measured by the FTLE values is relative between cells, the dependence of average speed on local cell density does not imply a FTLE dependence on density. After all, even if all the cells are moving faster, they need not be separating more quickly. The FTLE analysis is similar to the affine motion of the cells [147], which does not have a clear relationship with density.

We also measured the non-affine component of the motion using the parameter

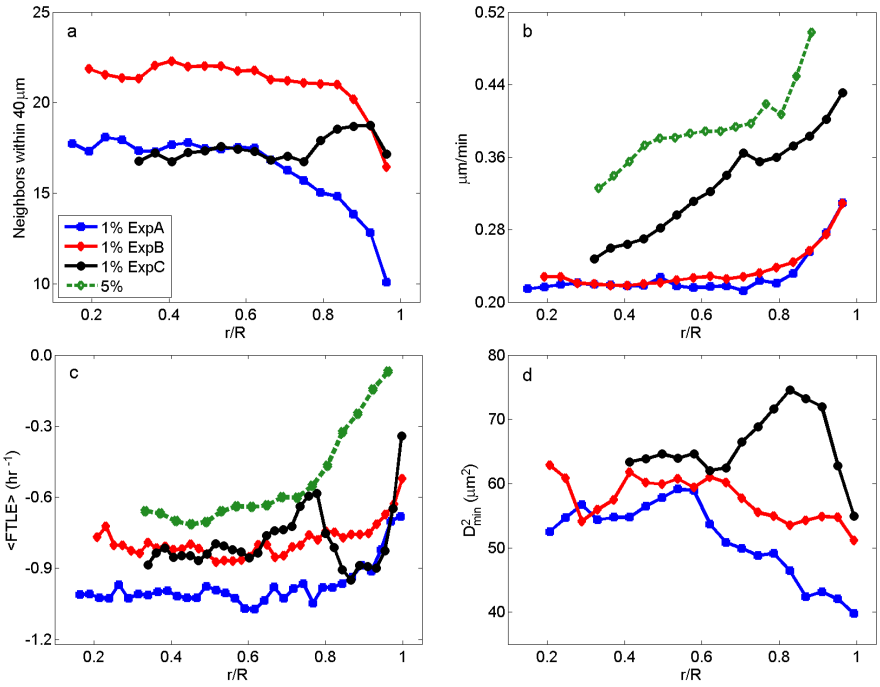

Figure 5.6: (a) Number density versus the normalized radius (r/R). In two cases, the density gradually decreases near the leading edge. In experiment C, a higher bump in density is seen near the leading edge. This is accompanied by a faster migration as seen in the speed profiles in (b). (c) FTLEs have a negative mean that approaches zero at long deformation times, showing that the flow is not chaotic. FTLEs are typically higher near advancing edges, where stretching is large. Higher FTLE values were observed when the cells were stimulated by higher concentrations of serum (5% serum compared to 1% serum). (d) D^2_{min} is in general higher near the center of the dot, with fewer rearrangements seen near the leading edge. In the case of the experiment C, a spike in D^2_{min} is seen which corresponds to the same region of higher density seen in (a). Each line represents the average over four different migration assays performed on the same day.

D^2_{min}. For each movie, for all frames and all cells, we determined D^2_{min} as a function of the local density, as shown in Figure 5.7(b). D^2_{min} is larger for higher densities in a consistent manner between experiments. This relationship points to the source of the difference in D^2_{min} for the edge and bulk data. The consistency between

experiments is reassuring, and the implications of the trend are intriguing. Non-affine motion increases as the density increases. This trend is the opposite of the one seen for a jammed system of soft particles [148]. In such jammed particulate systems, the probability of plastic deformations increases with decreasing density as more voids are created. In contrast, as cells get denser (more jammed), they rearrange more, suggesting active, individualistic motion. This active motion is a known feature of both healthy and cancerous cells; cells in epithelial sheets actively generate traction forces on the underlying substrate [72, 93, 134–136], and tumor cells are known to actively infiltrate surrounding tissues [133]. Cells are able to take advantage of forces generated by their cytoskeletal structures to migrate actively using structures such as lamellipodia and filopodia [69]. These same protrusive and contractive forces may contribute to cell rearrangements within a migrating sheet.

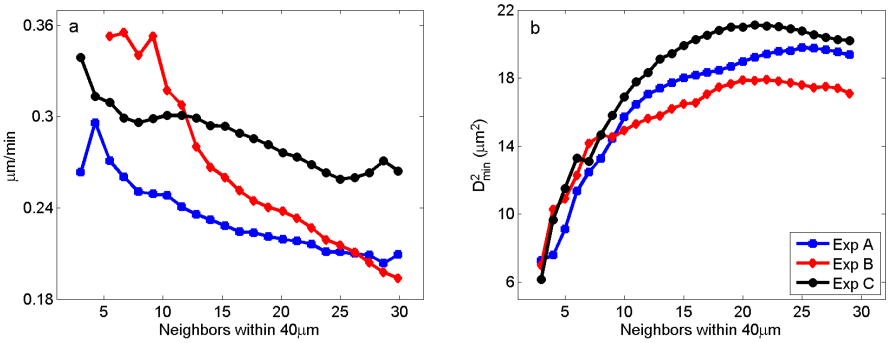

Figure 5.7: Speed and rearrangements can depend on cell density, even in the bulk movies in which there is no free edge. (a) Although the magnitude of the speed is dependent on the variation between experiments, in all cases, speed decreases at higher cell densities. (b) D^2_{min} shows a clear dependence on density with rearrangements increasing as number density increases. Each line is calculated from one representative bulk movie from each day of experiments.

5.4 Discussion

Using image analysis to extract velocity information from phase-contrast images of cells, we were able to quantify the migration of epithelial sheets. Looking only at the simple metric of speed, we distinguished different migration activity in the center and at the edge of the radially migrating monolayer. However, we also found significant variability from experiment to experiment due to the biological variability of our migration assay. These differences, accompanied by the evidence that smoothed velocity techniques like PIV capture elements of the system different from what is measured by commonly used nuclear tracking, provide motivation for precise quantitative metrics of the cell motion.

As a suggestion for one such metric, we presented FTLE fields for the migrating sheet. This analysis provided insight into the stretching of the cell flow field. Despite the wide variety of motion within the sheet, we found that its flow is not chaotic, because mean values of the FTLE were less than zero. Although we do expect stretching within the monolayer, because our assay is based on a radially expanding sheet of cells, our FTLE measurements indicate that the stretching is not exponential in time. Positive FTLE values are most commonly seen near the edge of the migrating sheet. Thus, the most rapid radial stretching is found in a small region close to the leading edge. We also find that increased stimulation through higher concentrations of serum leads to more instances of chaotic motion. Although the FTLE metric does not provide insight into the migration mechanism, these results suggest that FTLE values could be of use in quantifying future studies

on more specific sources of stimulation.

Approaching the migrating sheet as a collection of particles instead of a flowing continuum allowed us to address another aspect of the epithelial sheet motion — rearrangement. Using D^2_{min} as a parameterization of the non-affine motion within the monolayer, we found an increase in rearrangements when moving from the leading edge of the sheet to the center. Using non-affine motion as a metric for rearrangements provides more specific information than do other metrics such as pair separation distance (see for example the work by Ng et al. [91]). Pair separation distance describes the motion of two cells away from each other over time. Although this separation could be a sign of cell mixing, it could also signal motions such as smooth spreading. Considering D^2_{min} as a measure of non-affine motion allows us to separate smooth spreading from actual cell rearrangements, and it also allows us to retain information about the smooth motion of the sheet (such as spreading or translation) to compare to the non-affine individualistic motion seen in individual cells.

Looking only at the variation of rearrangements in comparison to radial position within the monolayer, we saw the same variation in properties seen when looking at simpler metrics such as speed. Motivated by similar trends seen in local cell number density, we compared the rearrangements to the number of neighbors around each cell. We found a clear relationship between the number density and rearrangements despite the day-to-day variability seen in other metrics. Although this finding motivated the study of non-affine motion within cell sheets, even more compelling is that an increase in local number density was accompanied by an in-

crease in rearrangements. This trend opposes the trends seen in current research on inanimate objects [148], and may therefore be a uniquely active property of the cell system.

Our analysis of the monolayer migration in this simple radial assay provides quantitative methods and metrics that could be of use in other migration assays. Because migration assays are widely used in drug studies and in determination of metastatic potential, our metrics could be readily introduced in the study of cancer to investigate differences in migration between cell lines of differing metastatic potential. Quantitative measurement of stretching and rearrangement could also be used to distinguish between the effects of various treatments designed to combat aggressive tumor cells. As migration studies become increasingly complex in an attempt to combat the wide variety of phenotypes seen in cancer and other diseases, quantitative measures such as these will become increasingly important.

5.5 Materials and Methods

5.5.1 Cell Culture and Microscopy

MCF10A cells were cultured in DMEM/F12 media supplemented with 5% horse serum, $10\,\mu g\,ml^{-1}$ insulin (Invitrogen), $10\,ng\,ml^{-1}$ EGF (Peprotech, Rocky Hill, NJ), $0.5\,\mu g\,ml^{-1}$ hydrocortisone and $100\,ng\,ml^{-1}$ cholera toxin (both Sigma, St Louis, MO). The cells were kept in a humidified atmosphere at 37 °C and 5% CO_2. For the migration assay, cells were plated in 12 well glass bottomed plates coated with collagen IV ($10\,\mu g\,ml^{-1}$ for approximately 3 days at 4 °C) and allowed to culture

overnight in DMEM/F12 containing 1% horse serum (unless otherwise noted to be 5% horse serum). Figure 5.1 provides an illustration of the plating technique. Cells were then imaged for 24h on an incubated microscope kept at 37 °C and 5% CO_2 (Zeiss Observer.Z1, Zeiss, Goettingen, Germany). Phase-contrast images of the cells were acquired at 2 minute intervals using a 10× objective.

5.5.2 Image Analysis

PIV analysis was performed using the MatPIV MATLAB toolbox (J Kristian Sveen, `http://folk.uio.no/jks/matpiv/`, GNU general public license). We used multiple iterations of interrogation window sizes, starting with two iterations of 64×64 pixel windows ($41.6\,\mu m \times 41.6\,\mu m$) and finishing with two iterations of 32×32 pixel windows ($20.8\,\mu m \times 20.8\,\mu m$). At each interrogation, 50% overlap was used and the windows are cross-correlated. After the final iteration, outliers were detected using a signal-to-noise filter. Vectors with a signal-to-noise ratio less than 1.3 were replaced by linearly interpolated values. In the case of movies involving a leading edge of the cell sheet, the edge of the sheet was segmented, and the detected edge was used to trim the PIV field to remove the zero-velocity contribution of the empty space from any further metrics.

We tracked individual nucleoli using an algorithm adapted from hydrodynamic turbulence studies, which is implemented in MATLAB and is available online [149]. We began by calculating each data set's mean image, which we took as the background. Wherever an individual image is sufficiently darker than the background

over a region of appropriate size, the algorithm identifies a dot (possible nucleolus), taking for its position the intensity-weighted centroid of the region. These dots were tracked with a predictive three-frame best-estimate algorithm [150], yielding the location of each dot over a range of frames. Because we are interested in the motion of cells, we then sought groups of dots that remained within a set distance of each other and replace those individuals with their centroid, approximating the motion of a cell's nucleus. We typically chose parameters that identified many dots, because we wanted to include as many real cells as possible and false positives produce short tracks with little statistical weight. In one example frame we hand-counted 674 dots in 372 cells, whereas our automated algorithm identified 817 dots, reducing that count to 504 after grouping. Automated tracking of dots in phase-contrast images gives us access to the individual motion of many more living cells than would be practical when counting by hand.

5.5.3 Field of View Reconstruction

For each of the circular monolayers of cells, four fields of view were recorded. In two of the image sequences, the field of view is entirely filled with cells and will be referred to as an image of the 'bulk.' In the other two image sequences — referred to as the 'edge' movies — the field of view included the leading edge of the cells and the empty space in front of the monolayer. Our initial analysis focused on the comparison of behaviors between these two sets of movies with no further spatial distinction. To probe the differences seen between edge and bulk migration behavior

in more detail, we performed a segmentation of the leading edge to obtain an outline of the monolayer over time. This segmented edge was then fit to a circle, allowing us to find an effective radius and center of the monolayer as a function of time. Each cell's position was converted into the radial distance from the center of the monolayer. The radial distance of a given cell from the center (r) normalized by the total radius of the monolayer (R) allowed us to compare cell motion to location within the sheet.

5.5.4 Finite-time Lyapunov Exponents

Working from PIV velocity fields, we calculated FTLEs, as shown in Figure 5.3. FTLEs were calculated by numerically advecting 'virtual' tracers through the measured, time-varying flow field. We initially seeded tracers on the PIV grid but subsequently allowed them to move off of the grid. We followed the tracer motion for a deformation time of 80 min. Because FTLEs asymptotically approach Lyapunov exponents, our results are not sensitive to the deformation time if it is reasonably long [103]. At the end of the deformation, we calculated the logarithm of the largest eigenvalue of the Cauchy-Green strain tensor for each cluster of four tracers that were initially neighbors; this is the local FTLE value. By measuring one FTLE value for each point on the PIV grid, we obtained the full FTLE field [104].

5.5.5 Non-affine Motion

To quantify rearrangements within the sheet, we looked at non-affine motion. Specifically, we measured relative motion at the single cell level—for each cell we looked at the relative displacements of its neighbors within a 40 µm radius. We then calculated the quantity $D^2_{min,i}$ [100, 145] which quantifies the non-affine deformation of the N neighbors (indexed by j) of cell i:

$$D^2_{min,i} = min\left(\frac{1}{N}\sum_j [\Delta\vec{d}_{ij} - E_i\vec{d}_{ij}]^2\right) \tag{5.1}$$

where the vector $\vec{d}_{ij}$ is the relative initial position of cells i and j, $\Delta\vec{d}_{ij}$ is their relative displacement, and the minimization is over all potential strain tensors E_i. In other words, we calculated the affine deformation field (E_i) that best describes the actual cell motion. If the motion around cell i were perfectly affine, $D^2_{min,i}$ would be zero; $D^2_{min,i}$ is larger for greater departures from purely affine motion. $D^2_{min,i}$ thus gives us the relative strength of non-affine motion, or plastic rearrangements, in the neighborhood of cell i.

Chapter 6: Cell-Cell Adhesion and Long Time-Scale Collective Dynamics

This chapter is adapted from Lee, Stuelten, Parent, and Losert [151]. Text and figures are reproduced here with permission. Rachel Lee performed the experiments and analyzed the data.

6.1 Overview

Migratory phenotypes of metastasizing tumor cells include single and collective cell migration. Although migration of tumor cells is generally less cooperative than that of normal epithelial cells, our understanding of precisely how they differ in long-time behavior is incomplete. We measure in a model system how cancer progression affects collective migration on long time scales and determine how perturbation of cell-cell adhesions—specifically reduced E-cadherin expression—affects the collective migration phenotype. Time-lapse imaging of cellular sheets and particle image velocimetry (PIV) are used to study quantitatively the dynamics of cell motion over ten hours. Long-time dynamics are measured via finite-time Lyapunov exponents (FTLE) and changes in FTLE values with time. We find that non-malignant MCF10A cells are distinguished from malignant MCF10CA1a cells by both short-

time (minutes) and long-time (hours) dynamics. In addition, short-time dynamics distinguish non-malignant E-cadherin knockdown cells from the control, but long-time dynamics and increasing spatial correlations remain unchanged. Epithelial sheet collective behavior includes long-time dynamics that cannot be captured by metrics that assess cooperativity based on short-time dynamics, such as instantaneous speed or directionality. The use of metrics incorporating migration data over hours instead of minutes allows us to describe more precisely how E-cadherin, a clinically relevant adhesion molecule, affects collective migration. We predict that the long-time scale metrics described here will be more robust and predictive of malignant behavior than analysis of instantaneous velocity fields alone.

6.2 Background

Cell migration has many implications for cancer progression [12,24,53,152] and tumor growth [35]. The collective behavior of cells is known to play an important role in biological processes ranging from embryonic development [20, 21] to wound healing [22, 60], but there is an incomplete understanding of how individual cell behaviors lead to emergent collective properties of cell groups.

A common method used to study collective migration in epithelial systems is the scratch assay [55], which allows for the imaging of large cell sheets over time. Recent studies have expanded this concept to include unconstrained migration assays that do not scratch the cells [57, 61] and unique microenvironments to induce collective migration [65,153]. As these experimental techniques have matured, there

has been an increasing need for a quantitative understanding of collective cell motion. Many groups have adopted cell tracking and particle image velocimetry (PIV) techniques to study correlations and swirls within the cell sheet [61, 86], the traction forces exerted by cells [94, 135], and a variety of other techniques comparing cell motion to fluid flows [6]. When applying these techniques to malignancy and metastasis, a single feature of collective motion may not provide enough information to understand the changes that cells undergo during cancer progression. As an example, although various cancer cell lines may show changes in speed, previous work has shown that additional metrics of migration, such as directionality, are needed to make distinctions between malignant and non-malignant cell lines [57]. Furthermore, even when considering multiple metrics, most prior work has been limited to analysis of short-term behavior, such as instantaneous speeds calculated on the scale of minutes. Here we argue that studying collective cell migration over multiple length and time scales provides additional information that is useful for distinguishing migration phenotypes. Although cell motion can occur on the time scale of minutes, cell division and metastatic invasion occur on time scales of hours or days. Thus, we expect that including long-time behavior over the course of hours into the collective motion phenotype may make the migration phenotype a better predictor of cancer metastasis.

In this work, we study the collective behavior of normal but immortal MCF10A cells (referred to as M1) and the invasive, lung colony forming MCF10CA1a cells (referred to as M4) in an unconstrained collective migration assay. Previously described short-time features of collective cell motion, such as directionality, are able to dis-

tinguish these two cell types [57]. We further explore the behavior of these cells, and find additional distinctions in metrics that describe long-time dynamics measured over hours. To assess the importance of long-time dynamics in understanding the migration phenotype, we present data on the perturbation of E-cadherin in these cell types. E-cadherin has been frequently studied in the context of cancer progression; its downregulation is considered a marker of the epithelial to mesenchymal transition (EMT) [17] and is often associated with a poor patient prognosis [115, 116]. Recent studies, however, have highlighted that the role of E-cadherin in cell-cell adhesion and collective migration is not simple [95, 110]. The long-time dynamics of E-cadherin knockdown cells presented here reinforce this complex role of adhesion and provide tools for future studies on the effect of cell-cell adhesion in cancer progression.

6.3 Results

To study the collective behavior of both the non-malignant M1 cells and the malignant M4 cells, we imaged circular confluent cell monolayers over a period of ten hours. Our imaging field of view, shown in Figure 6.1(a-d), records the leading edge of a larger monolayer (see Section 6.5.5). This assay, as well as similar techniques such as the scratch assay, are often used for assessing the collective migration of cells under a wide range of conditions. A common metric used to analyze these assays is displacement over a long time period [55], or in the case of our circular monolayers, the radial displacement over ten hours as shown in Figure 6.1(e). For

both cell types, the monolayer expands a few hundred microns over ten hours, and paired experiments show no difference in the displacement between the M1 and M4 cells (Figure 6.1(f)). By taking more frequent images of the monolayer and using PIV, we extract speed distributions within the monolayer, shown in Figure 6.1(g). These speed distributions reflect the motion of the monolayer on a time scale of three minutes. As expected from the radial displacement, the two cell types show a similar mean speed, but the long tail seen in the M4 distribution suggests that there are interesting differences in other migration dynamics features.

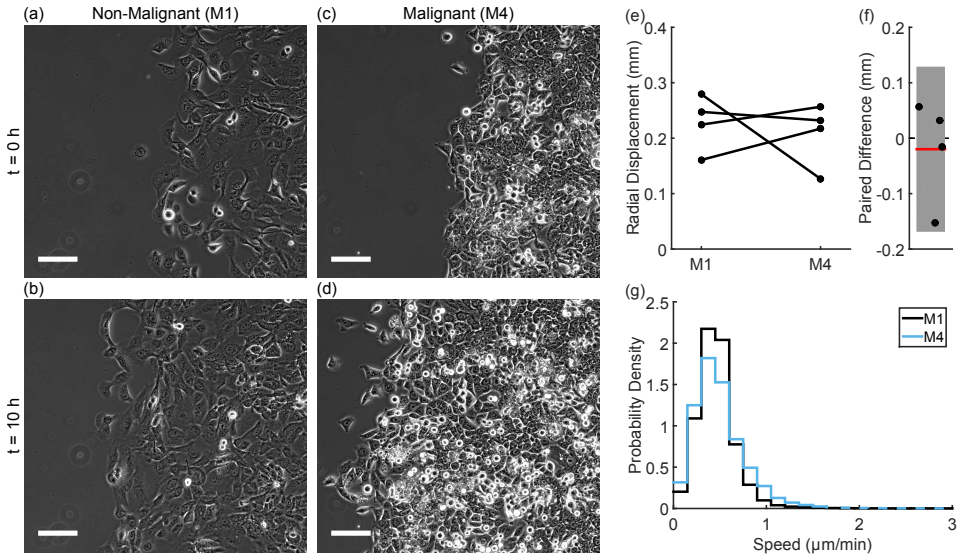

Figure 6.1: Phase-contrast images of the non-malignant M1 cells (a, b) and the malignant M4 cells (c, d) show the radial migration assay at $t = 0h$ (a, c) and $t = 10h$ (b, d). In all images, the scale bar indicates 100 µm. The absolute value of radial displacement varies (e), but paired experiments show no trend in the difference between M1 and M4 cells (f, error bar indicates 95% confidence interval). The speed distributions (cumulative over time and space) within the monolayer (cumulative from N = 4 experiments) show similar mean speeds, but the M4 distribution shows a longer high speed tail (g). Dashed lines indicate the region where the two curves overlap.

Our previous work has demonstrated that although M1 and M4 cells do not show a difference in mean speed, the M4 cells are less directional than the M1 cells [57]. The current data confirm this, as shown by the directional distributions in Figure 6.2(a). The M1 cells flow preferentially in the direction of radial expansion while the M4 cells show a much broader distribution of directions.

We have also previously demonstrated the use of finite-time Lyapunov exponent (FTLE) values for distinguishing collective behavior in cell monolayers [117]. Unlike the distributions of speed and velocity direction, which reflect short-time cell behavior on the time scale of imaging, FTLE values capture long-time behavior. Here we have shown distributions of speed and velocity direction that are cumulative over 10 hours of motion, but each individual value in the distribution was calculated by looking at cell motion from frame to frame (3 minutes). The FTLE values are calculated through the evolution of cell motion over many frames (2 hours) and thus inherently capture longer time behavior. Positive FTLE values are a signature of chaotic flows and, as shown by the distributions in Figure 6.2(b), the M4 cells show a shift towards higher FTLE values resulting in more regions of flow with positive FTLE values.

We further explore the long-time dynamics of collective migration by looking at the evolution of migration metrics over the duration of the experiment. Representative speed traces from a paired experiment show that the mean speed of the monolayer tends to decrease slightly over time (Figure 6.3(a)), with the M1 and M4 cells showing a similar trend over ten hours, which is consistent with the radial displacement profiles in Figure 6.1(e). Angular deviation—a measure of the spread

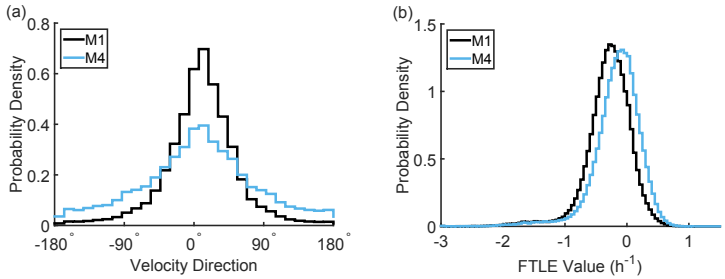

Figure 6.2: As shown by the angle distributions in (a), the M4 cells are less directional than the M1 cells. The M4 cells show more positive FTLE values than the M1 cells, as shown by the distributions in (b). Each distribution represents the cumulative data from N = 4 experiments and is cumulative over time and spatial location.

in velocity direction) shown in Figure 6.3(b)—consistently shows a broader distribution for the M4 cells, as was shown in Figure 6.2(a). Looking at this distribution over ten hours, however, provides added understanding of collective behavior by showing different long-time trends for angular deviation. In the paired experiment shown in Figure 6.3(b), the M4 cells maintain a broad distribution over time while the M1 cells become more directed over time. A similar trend is seen in the FTLE analysis; we use the fraction of the cell monolayer with positive FTLE values (Figure 6.3(c)) as one indication of the amount of chaotic motion in the sheet over time. It is clear that the M4 cells remain steadily chaotic over time while the M1 cells show decreasing positive FTLE values over ten hours.

To compare these trends on the same scale, we calculate the fractional change over time for each metric by linearly fitting the percent change over time and finding the slope in percent per hour (Figure 6.3(d-i)). As shown by the paired speed slopes in Figure 6.3(e), there is no difference in the long-time speed behavior between the

M1 and M4 cells. Yet, for each cell line, the slope of angular deviation over time is variable (Figure 6.3(f)), and paired experiments show that the M4 cells have a larger slope than the M1 cells. The M4 cells' angular distribution therefore broadens more over time than the distribution for the M1 cells (Figure 6.3(g)). The difference in long-time behavior is seen most clearly in the FTLE slopes. The M4 cells show stable fractions of chaos over time (approximately zero slope), while the M1 cells show decreasing amounts of positive FTLE values over time (Figure 6.3(h)) leading to a distinct paired difference on the order of 5-10% per hour (Figure 6.3(i)).

These results suggest that the M4 cells either remain disordered or become more disordered over time while the M1 cells tend to remain ordered or become more ordered over time. Another way of looking at this behavior is to investigate the fluctuations within the cell sheet. As previously described [83], averaging the cell flow field over increasing time intervals decreases the variance in velocity. In Figure 6.4 we investigate the rotational velocity of the cells, i.e., the motion in a direction orthogonal to the expanding monolayer. For both cell types, the variance decreases as the flow field is averaged over increasing time intervals and can be fit to an exponential to determine a characteristic time scale; representative examples of this fit are shown in Figure 6.4(a) and Figure 6.4(b) for the M1 and M4 cells, respectively. As shown in Figure 6.4(c), fluctuations in the M1 cells persist longer than in the M4 cells. That fluctuations in the M4 cells are more transient agrees with the trends seen in Figure 6.3; the M4 cells maintain a high angular deviation over time while also maintaining high FTLE values.

The trends in Figures 6.3 and 6.4 show that considering dynamics over a longer

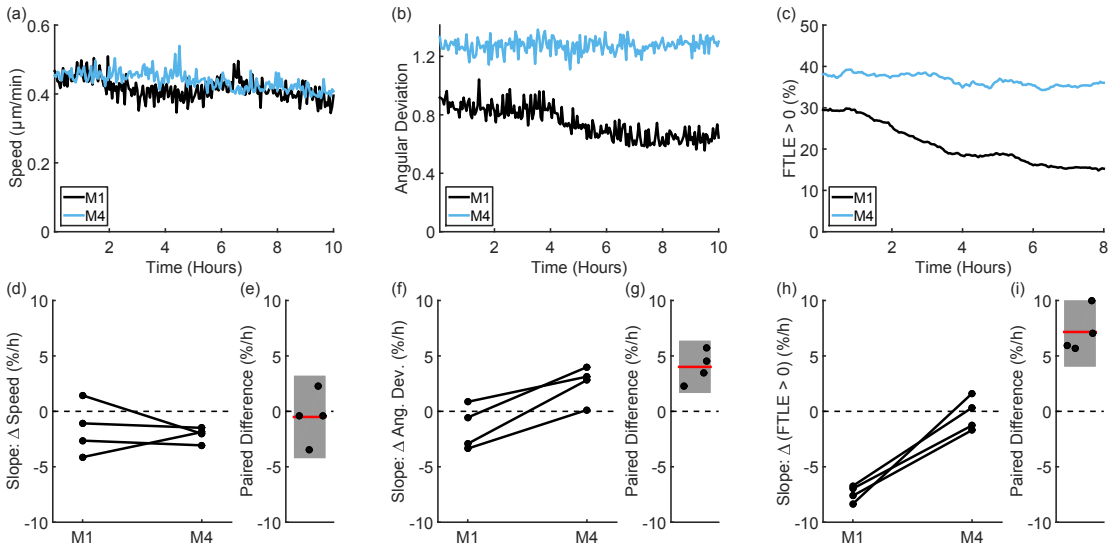

Figure 6.3: Representative time traces of speed (a), angular deviation (b), and FTLE values (c) from paired experiments show differences in the migration phenotypes of the M1 and M4 cells. As shown by looking at the slope of speed over time (d), there is no trend in the difference between the M1 and M4 cells (e). However, the slope of angular deviation over time (f) tends to be higher in the M4 cells than in the M1 cells (the paired difference is shown in (g)). This is consistent with the trend seen in the FTLE values (h), where the M1 cells show a negative slope over time, while the M4 cells hold a fairly constant FTLE value over time and show a strong difference from the M1 cells (i). Lines in (d, f, h) pair experiments performed on the same day and error bars in (e, g, i) indicate 95% confidence intervals.

time scale (i.e., hours instead of minutes) provides additional information about the collective migration phenotype. This long-time view can also be expanded to include spatial information by considering velocity correlations. Representative correlations for the M1 (Figure 6.5(a)) and the M4 (Figure 6.5(b)) radial velocities show that spatial correlations vary over time in these cell types. Both the M1 and M4 cells initially migrate in a similarly correlated fashion. Over the ten hour duration of the experiment, however, the M4 cells become less correlated, as shown in in Figure

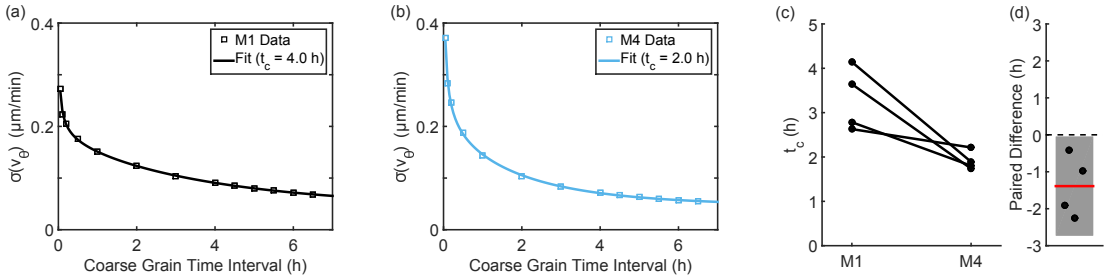

Figure 6.4: Representative examples of the velocity variance (σ) calculated during coarse graining (squares) along with an exponential fit (solid line) for the M1 cells (a) and for the M4 cells (b). As shown by the paired values, the M4 cells show a shorter characteristic time scale than the M1 cells (c, d). Lines in (c) pair experiments performed on the same day and the error bar in (d) indicates the 95% confidence interval.

6.5(c) by the sampling of the correlation function at a distance of approximately 100 μm (on the order of a few cells). The M1 cells either become more correlated or remain correlated, eventually reaching the same correlation value over ten hours. The variability in initial correlation values for the M1 cells may reflect transient changes in behavior due to the initial plating of the cells, but the long-time behavior confirms that the M1 cells move with correlations on the order of a few cells. The M1 cells thus organize their radial velocity over time while the M4 cells lose coordination even on short length scales.

6.3.1 E-cadherin and Collective Dynamics

E-cadherin plays an important role in cell-cell adhesion and is expressed in both M1 and M4 cells (see Section 6.5.2). To perturb the collective migration phenotype, we downregulated E-cadherin expression using shRNA in both the M1 and M4

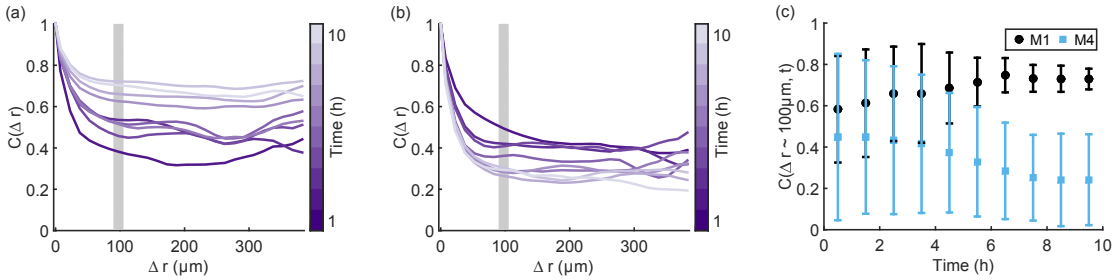

Figure 6.5: Representative spatial correlations for radial velocity of the M1 (a) and M4 (b) cell lines over time show two distinct migration phenotypes. Color in (a, b) indicates time with earlier hours in dark purple and the end of the experiment in light purple. The trend in the region $90\,\mu\text{m} < \Delta r < 105\,\mu\text{m}$ (marked by the gray rectangles in (a, b)) shows that the M1 cells remain correlated over 10 hours, while the M4 cells become decreasingly correlated (c). Error bars in (c) indicate 95% confidence intervals.

cells. The knockdown cell lines show decreased expression of E-cadherin at cell-cell junctions, as shown by immunofluorescence labeling (see Section 6.5.3), and we investigate how this change affects the long-time dynamics of collective migration. In the following, we compare the E-cadherin knockdown cell lines to a nonsense (NS) shRNA control. The speeds, angular deviation, and FTLE values measured for the NS control may vary from the previously shown figures as the absolute speed and positive FTLE values are sensitive to day-to-day variations and thus must be compared in paired experiments. However, the long-time dynamics we observe are robust to day-to-day variations and remain the same across our experiments. See Figures 6.6 and 6.7 for a paired comparison between the non-perturbed cells and NS control cells of the M1 and M4 cells, respectively.

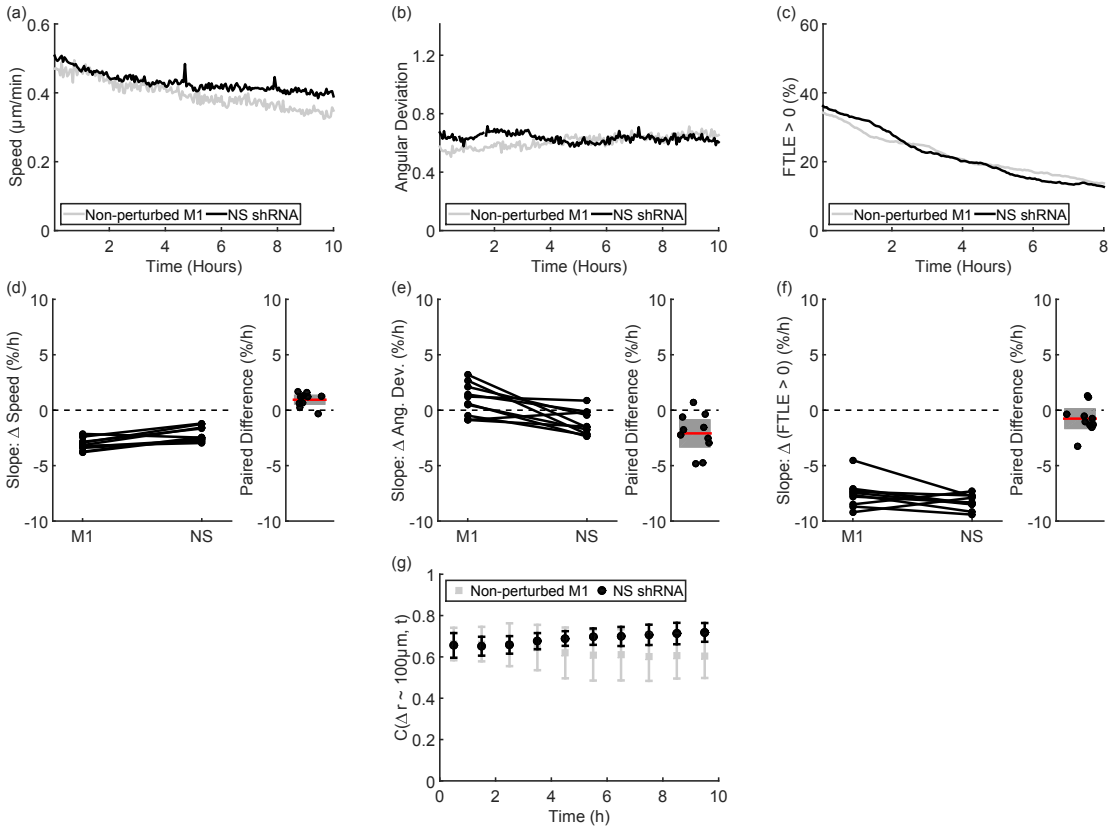

Figure 6.6: **Comparison between M1 cells and shRNA Control cells** Representative time traces of speed (a), angular deviation (b), and positive FTLE values (c) show no difference between the M1 cells and the nonsense (NS) shRNA control cells. As shown by the experimentally paired differences between non-perturbed and NS control in the slopes of speed (d), angular deviation (e), and FTLE values (f), there is no change in long time trends. The correlations remain high over time for both cell types, as shown by the correlations in the region $90\,\mu\text{m} < \Delta r < 105\,\mu\text{m}$ (g). Error bars in ($d - g$) indicate 95% confidence intervals.

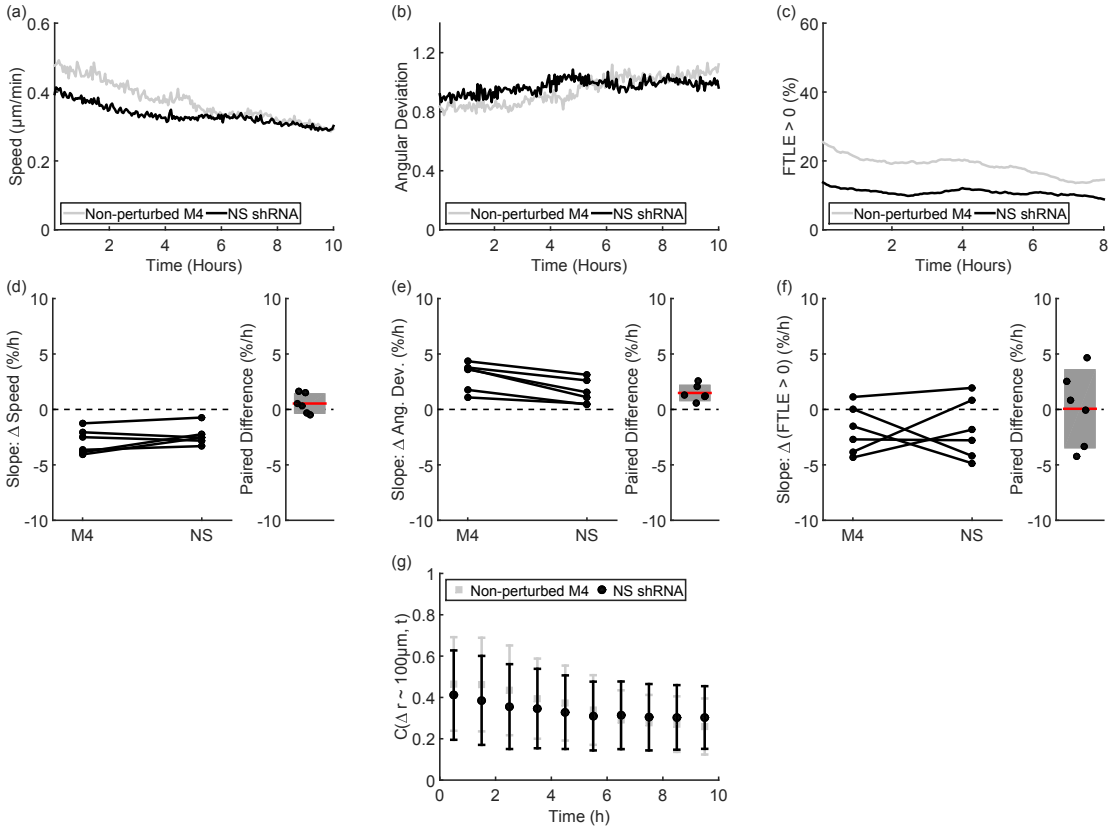

Figure 6.7: **Comparison between M4 cells and shRNA Control cells** Representative time traces of speed (a) and angular deviation (b) show no difference between the M4 cells and the nonsense (NS) shRNA control cells. The absolute value of positive FTLE values (c) from paired experiments show some changes between the non-perturbed M4 cells and the NS control but no changes in long time behavior. As shown by the experimentally paired differences between non-perturbed and NS control in the slopes of speed (d), angular deviation (e), and FTLE values (f), there is no change in long time trends. The correlations decrease over time for both cell types, as shown by the correlations in the region $90\,\mu\text{m} < \Delta r < 105\,\mu\text{m}$ (g). Error bars in ($d-g$) indicate 95% confidence intervals.

6.3.1.1 M1 E-cadherin shRNA Cell Lines

As with the comparison between parental cell lines, the M1 E-cadherin shRNA cell lines cannot be distinguished from their NS control by radial displacement or mean speed (Figure 6.8). Yet, the cells can still be distinguished by their short-time behavior—E-cadherin knockdown reduces cohesivness enough to broaden the velocity direction distribution (Figure 6.9).

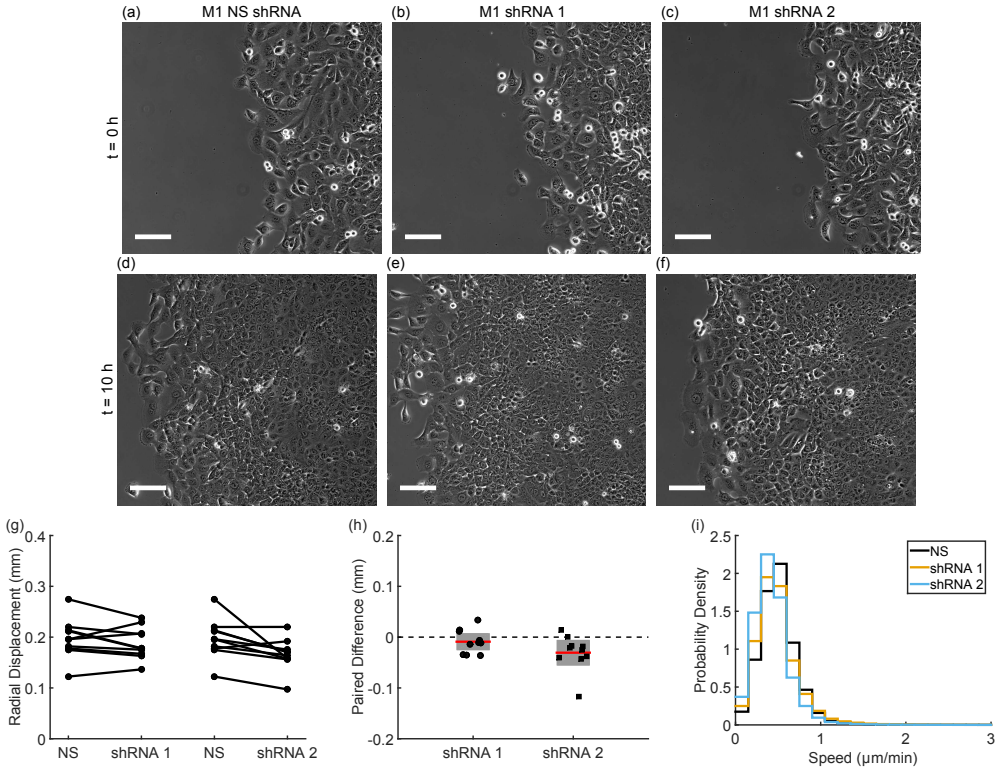

Figure 6.8: Phase-contrast images of the M1 nonsense (NS) shRNA cells (a, d) and two E-cadherin shRNA cell lines $(b, e$ and $c, f)$ show the radial migration assay at $t = 0h$ $(a\text{-}c)$ and $t = 10h$ $(d\text{-}f)$. In all images, the scale bar indicates 100 µm. The absolute value of radial displacement varies (g), but paired experiments show no trend in the difference (h). Lines pair experiments from the same day (g) and error bars indicate 95% confidence intervals (h). Speed distributions within the monolayer show similar mean speeds $(i$, cumulative from N = 10 experiments).

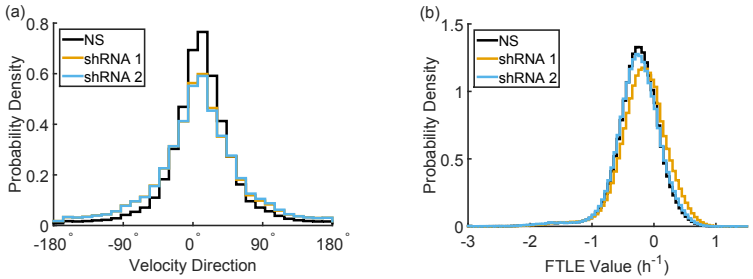

Figure 6.9: **M1 E-cadherin shRNA cells** As shown by the angle distributions in (*a*), the M1 E-cadherin shRNA cells are less directional than the nonsense (NS) shRNA cells. However, the long-time behavior represented by FTLE values (*b*) only shows a slight difference. Each distribution represents the cumulative data from N = 10 experiments and is cumulative over time and spatial location.

Migration behavior on the time scale of hours, however, remains similar to the control dynamics in all the shRNA cell lines. Speed decreases slightly over time (Figure 6.10(a)) without a strong difference between the NS control and the E-cadherin shRNA cell lines (Figure 6.10(d)). Although angular deviation is on the whole higher in the E-cadherin shRNA cell lines (Figure 6.9(a)), both cell lines show similar trends over time to the NS control (Figure 6.10(e)). The shRNA cell lines show variable increase in FTLE values (see Figure 6.9(b)) but still show a strong decrease in values over time (Figure 6.10(c)) without strong slope changes between the shRNA cell lines and the NS control (Figure 6.10(f)). Fluctuations within the knockdown cell lines continue to show a characteristic time scale on the order of three hours (Figure 6.11), as was found for the unperturbed cell lines (Figure 6.4).

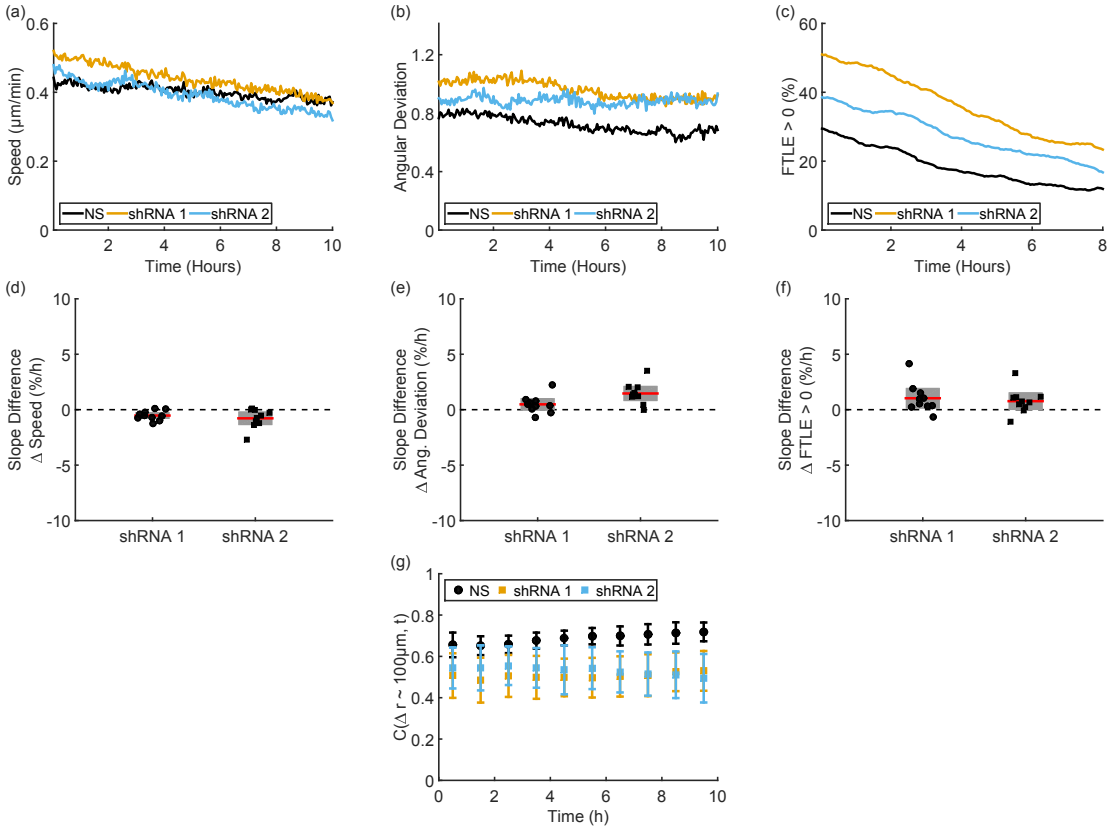

Figure 6.10: **M1 E-cadherin shRNA cells** Representative time traces of speed (a), angular deviation (b), and FTLE values (c) from paired experiments show some changes between the nonsense (NS) and E-cadherin shRNA knockdown cell types but no changes in long time behavior. As shown by the experimentally paired differences between knockdown and NS in the slopes of speed (d), angular deviation (e), and FTLE values (f), there is no change in long-time trends after E-cadherin knockdown. Although the E-cadherin shRNA cell lines show decreased correlations values compared to the NS cell line, the correlations are stable for each cell type, as shown by the correlations in the region $90\,\mu\text{m} < \Delta r < 105\,\mu\text{m}$ (g). Error bars in ($d - g$) indicate 95% confidence intervals.

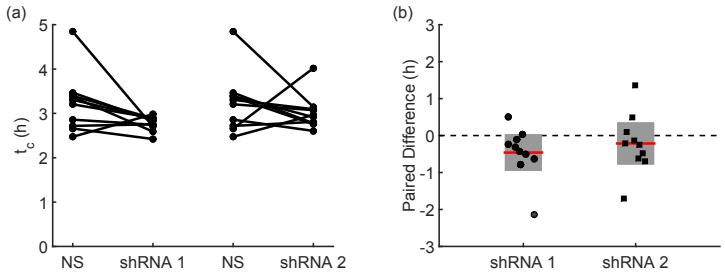

Figure 6.11: **M1 E-cadherin shRNA cells** Coarse graining the cells' PIV flow field over increasing time intervals decreases the variance (σ) of the velocity field. By fitting the variance of the velocity orthogonal to the cell migration to an exponential decay (see methods), we calculate a characteristic time scale of fluctuations in the flow. As shown by the paired values (a) and paired differences (b), the M1 E-cadherin shRNA cells show a similar characteristic time scale to the nonsense (NS) shRNA cells. Lines in (a) pair experiments performed on the same day and error bars in (b) indicate 95% confidence intervals.

A similar pattern is seen in spatial correlations over time. Although the knock-down cell lines show a slight decrease in overall correlation compared to the NS control, all M1 cell lines show a stable or slightly increasing correlation over ten hours (Figure 6.10(g)).

6.3.1.2 M4 E-cadherin shRNA Cell Lines

The M4 E-cadherin shRNA cell lines show similar speed distributions and radial displacement to the NS control (Figure 6.12). The NS cell lines already show a broad direction distribution, and the shRNA cell lines show a similar short-time behavior with wide velocity angle distributions (Figure 6.13).

Representative time traces of speed (Figure 6.14(a)) and angular deviation (Figure 6.14(b)) show similar ranges of values and confirm the similarity in behavior

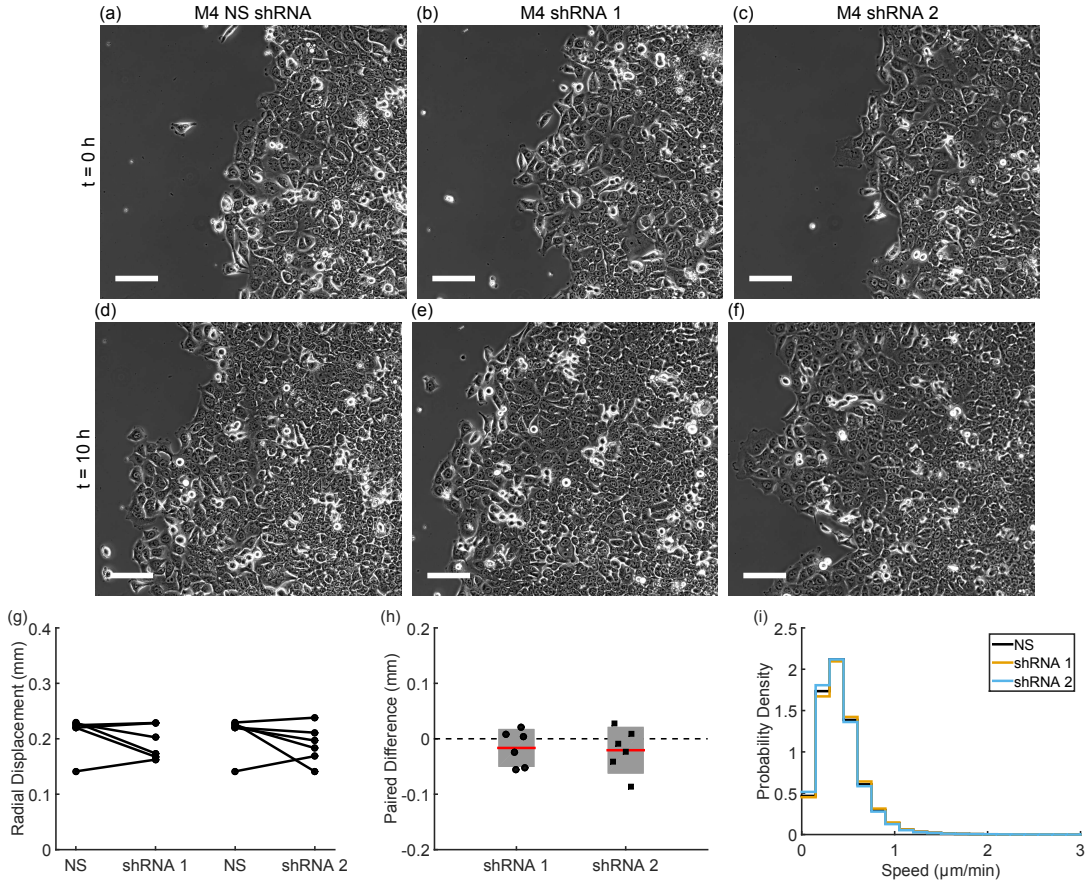

Figure 6.12: **M4 E-cadherin shRNA cells** Phase-contrast images of the M4 nonsense shRNA cells (a, d) and two E-cadherin shRNA cell lines $(b, e$ and $c, f)$ show the radial migration assay at $t = 0h$ $(a\text{-}c)$ and $t = 10h$ $(d\text{-}f)$. In all images, the scale bar indicates 100 µm. The edge of the monolayer moves at similar speeds for all cell types. The absolute value of radial displacement varies (g), but paired experiments show no trend in the difference between the cells (h). Lines in (g) pair experiments performed on the same day and error bars in (h) indicate 95% confidence intervals. The speed distributions (cumulative over time and space) within the monolayer show similar mean speeds $(i$, cumulative distributions from N = 6 experiments).

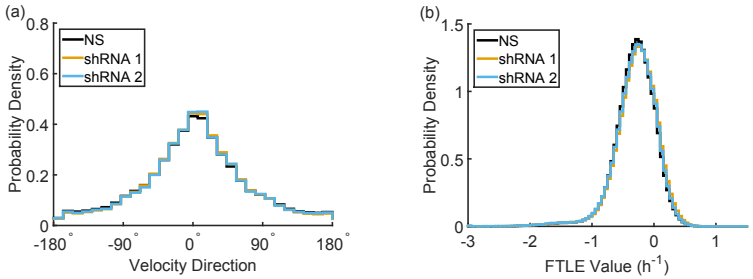

Figure 6.13: **M4 E-cadherin shRNA cells** The M4 nonsense (NS) and E-cadherin shRNA cell all show low directionality, as shown by the angle distributions in (a). The long-time behavior represented by FTLE values also shows a similar distribution (b). Each distribution represents the cumulative data from N = 6 experiments and is cumulative over time and spatial location.

on the scale of minutes. Along with positive FTLE values (Figure 6.14(c)), these metrics show similar long-time dynamics as well; the change over ten hours in all three metrics shows no difference between the E-cadherin shRNA and NS cell lines (Figure 6.14(d-f)). All M4 shRNA cell lines also show similar spatial fluctuations with a characteristic time scale of approximately two hours (Figure 6.15).

Spatial correlations in the M4 shRNA cell lines are also similar to those seen in the unperturbed M4 cells. On short distances, the M4 cells become decreasingly correlated over ten hours (Figure 6.14(g)), indicating a lack of coordinated motion even on the length scale of a few cells.

6.4 Discussion

Short-term collective behavior is important for many systems; it is often studied in the context of flocking birds or schooling fish and has also been shown to

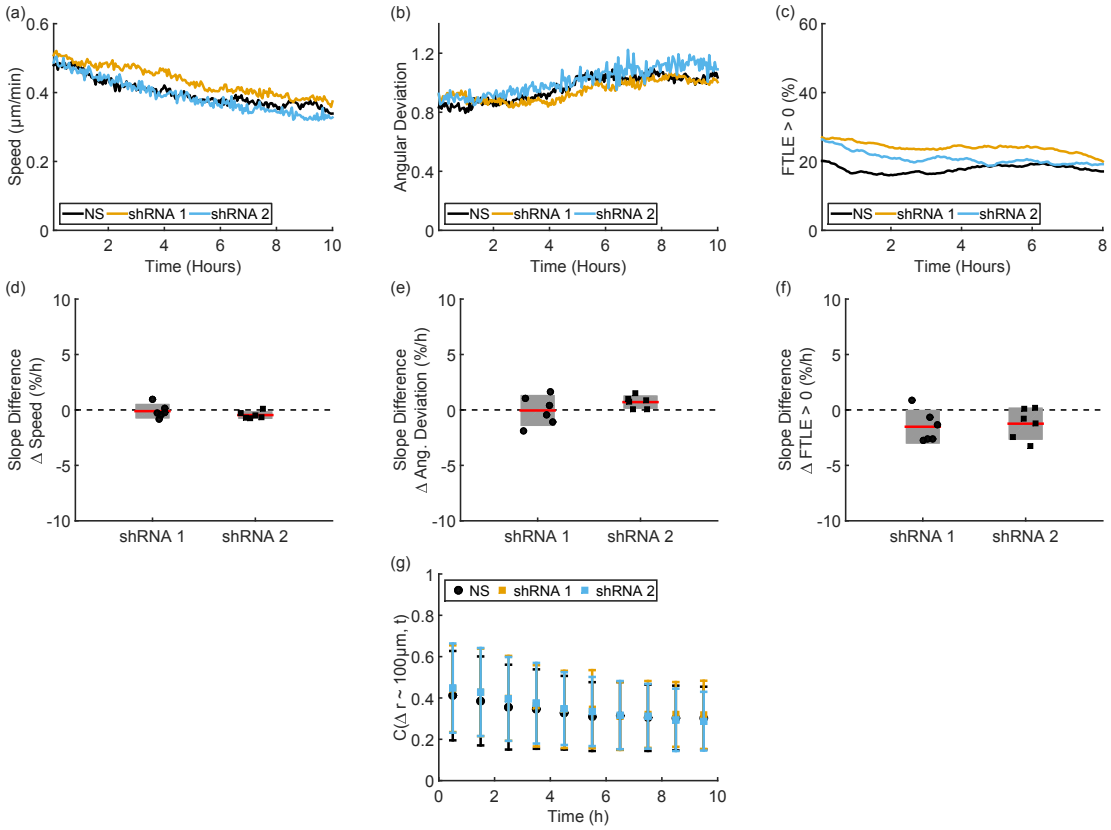

Figure 6.14: **M4 E-cadherin shRNA cells** Representative time traces of speed (a), angular deviation (b), and FTLE values (c) from paired experiments show no distinct changes between the nonsense (NS) and E-cadherin shRNA knockdown cell types. As shown by the experimentally paired differences between knockdown and NS in the slopes of speed (d), angular deviation (e), and FTLE values (f), there is no change in long-time trends after E-cadherin knockdown. The E-cadherin shRNA cell lines show similar correlation values compared to the NS cell line; (g) shows the correlation values in the region $90\,\mu\text{m} < \Delta r < 105\,\mu\text{m}$ over time. Error bars in ($d - g$) indicate 95% confidence intervals.

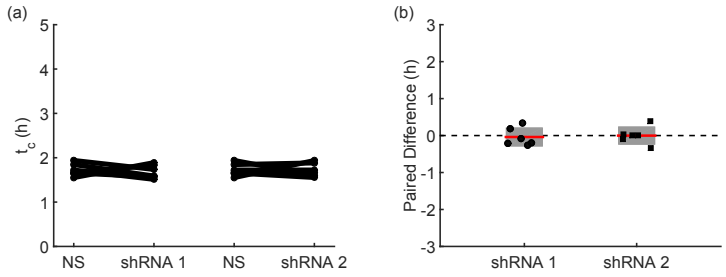

Figure 6.15: **M4 E-cadherin shRNA cells** Coarse graining the cells' PIV flow field over increasing time intervals decreases the variance (σ) of the velocity field. By fitting the variance of the velocity orthogonal to the cell migration to an exponential decay (see methods), we calculate a characteristic time scale of fluctuations in the flow. As shown by the paired values (a) and paired differences (b), the M4 E-cadherin shRNA cells show a similar characteristic time scale to the nonsense shRNA cells (NS). Lines in (a) pair experiments performed on the same day and error bars in (b) indicate 95% confidence intervals.

be of interest in epithelial cell systems during development, wound healing, and tumor cell invasion. Here we argue that assessing long-term collective behavior on the scale of hours is also necessary for understanding cell migration in the context of cancer progression. The importance of long-time behavior in metastatic systems is intuitive; strands of malignant cells can spend days or weeks invading into the surrounding tissue from the primary tumor [53]. Despite the long time scales discussed in *in vivo* studies or the time lapse that might occur between patient visits in clinical data, *in vitro* studies of collective behavior often focus on short-time dynamics such as instantaneous speed or directionality calculated over minutes or simply neglect dynamics to focus instead on the collective structure of the cells. As we have previously shown [57] and here confirm, short-time metrics can be useful in distinguishing features of the non-malignant M1 and malignant M4 migration

phenotypes. However, collective migration incorporates behaviors not captured by these short-time-scale measures—a strand of cells *in vivo* is inherently collective, but looking at the cells on short time scales does not inform us if the structure will remain the same over hours, if there will be small disturbances in the structure, or if the cells will undergo large-scale rearrangements. We have recently developed tools for the measurement of long-time collective behavior [117] that reveal other interesting features of the collective migration phenotype. FTLE values reflect the evolution of a cell sheet over longer times and show less collective order in the M4 cells (Figure 6.2). In addition, the change in FTLE values over time provides insight into the migration phenotype by revealing that the M4 cells maintain a disordered flow over time but that the M1 cells become more ordered over the course of ten hours (Figure 6.3). This same behavior can be seen in flow fluctuations (Figure 6.4) and the time evolution of spatial correlations (Figure 6.5). With multiple tools for quantifying collective behavior, we are able to provide additional understanding to the collective behavior changes observed in this cancer progression model.

These quantitative tools also allow us to investigate the role of E-cadherin, a clinically relevant cell-cell adhesion protein, in the collective migration phenotype. We find that in the non-malignant M1 cells, a reduction in E-cadherin expression results in decreased directionality. This decrease causes the M1 shRNA cell lines to resemble the M4 control cell lines when dynamics are measured on the scale of minutes. As the M4 cells already show little coordinated behavior on short time scales, we found no change in directionality for the M4 shRNA cell lines. These metrics provide interesting insight into the role of E-cadherin in collective

migration but on their own may overstate the role that E-cadherin plays in M1 migration. The long-time behavior, in fact, seems to suggest the opposite: despite the short time changes seen, the M1 E-cadherin shRNA cell lines continue to show increasing coordination over time scales of hours. Because E-cadherin is one of the main players in epithelial cell-cell adhesion, at first glance it may seem surprising that it did not have a stronger influence on the collective phenotype. This could be due to the fact that the small remaining E-cadherin expression in the shRNA cells is enough to compensate for some of the effects of E-cadherin on long-time dynamics. In addition, E-cadherin and adherens junctions are only one form of cell-cell adhesion; tight junctions, desmosomes, and gap juctions may all play a role in the collective behavior of the cell sheet. In the non-malignant M1 cells, then, it is not surprising that knockdown of a single component of the intercellular adhesome does not abolish all types of collective behavior. In fact, a recent study has shown that while E-cadherin plays a role in migration, P-cadherin is a better predictor of intercellular tension, a mechanical feature also relevant to collective migration [95]. Viewed in the wider context of cell-cell adhesion, it is not surprising then that short-time collective behavior and long-time coherent migration are regulated differently. Our results indicate that the M1 cells use E-cadherin for coordination of collective motion on time scales of minutes, yet even with decreased E-cadherin expression, the cells prefer to remain coordinated over longer time scales of hours. In contrast, the migration behavior of M4 cells, which already shows decreased collective dynamics on both time scales, is insensitive to the change in E-cadherin expression.

Because decreasing E-cadherin does not perturb the changes in dynamics seen

over hours, it is also possible that this feature of collective migration is regulated by a property other than cell-cell adhesion. In our experiments, although both cell lines were plated with the same initial cell number, by the time of imaging the cells had reached different densities. This is likely due to a combination of the cells' ability to adhere initially to the surface and the proliferation rates of each cell line. As can be seen in the time-lapse images, the M4 cells proliferate more than the M1 cells, although both proliferation rates are of the same order of magnitude. Proliferation has been previously quantified for these cell lines and was shown not to influence the overall displacement of the cell monolayer edge [57]. That result is consistent with other studies, such as the study by Poujade, et al. [61], which found that migration proceeds even upon the inhibition of cell division. Proliferation rates and density may influence collective behavior, however, and lead to changes in metrics such as those presented in this work. Investigating the role of proliferation and density using fluorescent nuclei will be an interesting direction for future research on the dynamic changes that take place during collective migration.

In further research, the investigation of both short- and long-time dynamics will be useful in determining which aspects of collective behavior are most relevant to the metastatic process. There remain many unanswered questions about cell-cell adhesion components in the malignant migration phenotype; dynamic measurements may help to determine the role that various junctions play in the changes seen during cancer progression. Determining which time scales are most predictive of malignant behavior could eventually lead to improved diagnosis and treatment options. Here we present analysis of time scales of minutes and hours, but data on the clinical time

scales of weeks and months will likely also show interesting migration dynamics. If, as we hypothesize, dynamical measurements on the scale of hours are able to predict tumor cell behavior over much longer time scales, information from simple *in vitro* studies on patient cells or perhaps future clinical imaging techniques may allow diagnosis without the need to monitor tumor growth over weeks or months.

6.5 Materials and Methods

6.5.1 Cell Culture

Normal but immortal MCF10A (M1) cells and invasive, lung colony forming MCF10CA1a (M4) cells were used in this study (Barbara Ann Karmanos Cancer Institute, Detroit, MI). M4 cells were cultured in DMEM/F12 medium supplemented with 5% horse serum (both from Invitrogen, Carlsbad, CA). M1 cells were cultured in M4 medium additionally supplemented with $10\,\mu g\,ml^{-1}$ insulin (Invitrogen), $10\,ng\,ml^{-1}$ EGF (Peprotech, Rocky Hill, NJ), $0.5\,\mu g\,ml^{-1}$ hydrocortisone, and $100\,ng\,ml^{-1}$ cholera toxin (both Sigma, St. Louis, MO). Cells were kept in a humidified atmosphere at 37 °C and 5% CO_2.

For downregulation of E-Cadherin, cells were stably infected with pGIPZ lentiviral particles coding for shRNA (V2LHS_14838, V3LHS_346823, Dharmacon, Lafayette, CO). Non-coding RNA ('nonsense') was used as a negative control. Infected cells were selected with and maintained in puromycin containing medium ($5\,\mu g\,ml^{-1}$). E-Cadherin expression levels were analyzed by Western blotting as described below.

6.5.2 Western Blots

Cells were plated in tissue culture dishes such that they were confluent after overnight culture. The cells were then lysed in a 20 mM Tris pH 7.5, 150 mM CaCl, 1 M EDTA, and 1% TritonX100 solution that was then supplemented with cOmplete Mini and PhosSTOP (Roche, Indianapolis, IN). After centrifugation (14,000 rpm, 15 minutes, 4 °C), the protein concentration of the supernatant was determined by Bradford assay (BioRad, Hercules, CA). Proteins were separated using sodium dodecyl sulfate-polyacrylamide gel electrophoresis (SDS-PAGE) and then were transferred to PVDF membranes. The membranes were blocked with 3% BSA (MP Biomedicals, Santa Ana, CA) in TBST and then incubated in primary antibody (overnight in anti-E-cadherin 1:8000 (Invitrogen) or three hours in anti-actin 1:60,000 (Chemicon)) in 0.3% TBST followed by incubation with a horseradish peroxidase (HRP) conjugated antibody (anti-mouse 1:10,000 (Pierce, Rockford, IL)) for one hour. The antigens were visualized using SuperSignal West Pico Chemiluminescent Substrate (ThermoFisher Scientific, Waltham, MA). As shown in Figure 6.16, both the M1 and M4 cells express E-cadherin, with decreased E-cadherin expression in the knockdown cell lines; actin expression is shown as a control.

6.5.3 Immunofluorescence

Cells were cultured on 12 well plates, as described in Section 6.5.4. Two hours after the culture medium was lowered to 1% horse serum, cells were fixed with 4% paraformaldehyde in PBS for 10 minutes. The cells were washed with 0.1 M

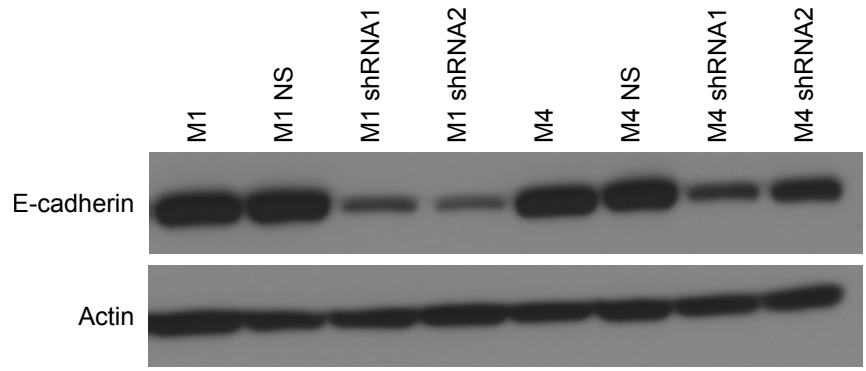

Figure 6.16: Western blot showing E-cadherin knockdown cell lines.

glycine and then permeabilized with 0.2% Triton. This was followed by blocking with 1% BSA (MP Biomedicals, Santa Ana, CA) in PBS. Cells were incubated with primary antibody (anti-E-Cadherin, 1:800 (Invitrogen)) in 0.1% BSA in PBS at 4 °C overnight followed by incubation with anti-mouse antibodies conjugated to Alexa 568 or Alexa 647 (Invitrogen). Nuclei were labeled with DAPI and the cells were imaged at 40× using a Zeiss Observer.Z1 inverse microscope.

6.5.4 Migration Assay and Microscopy

Glass bottom 12 well plates were coated with 10 µg ml^{-1} collagen IV in 50 mM HCl in a humid chamber at room temperature overnight, air dried, and stored at 4 °C until further use. Cells were plated in a 10 µL drop at a concentration of 3×10^6 cells/ml. After approximately one hour, non-adherent cells were washed off and the well was filled with medium [57]. Two hours before imaging, the medium was replaced with fresh medium modified to have a concentration of 1% horse serum. The cells were imaged overnight for a period of 10 hours on an incubator microscope at

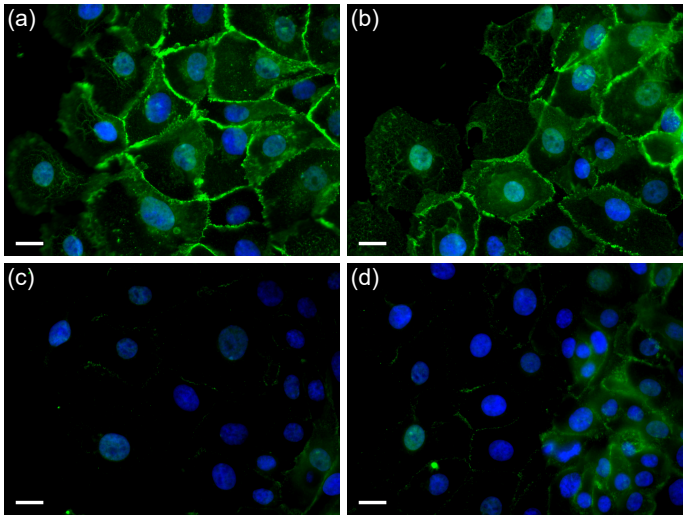

Figure 6.17: **E-cadherin in M1 cells** Immunofluorescence images of E-cadherin (green) and the nucleus (blue) for the unperturbed M1 (a), M1 nonsense (NS) shRNA (b) and E-cadherin shRNA ($c - d$) cell lines. In all images, the scale bar indicates 25 µm.

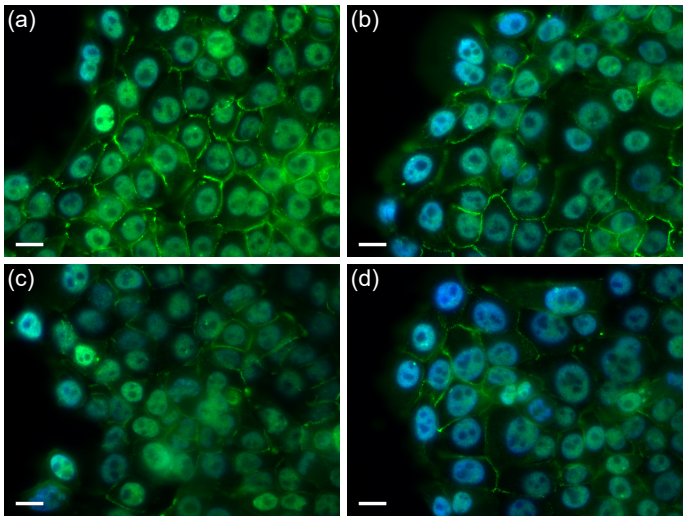

Figure 6.18: **E-cadherin in M4 cells** Immunofluorescence images of E-cadherin (green) and the nucleus (blue) for the unperturbed M4 (a), M4 nonsense (NS) shRNA (b) and E-cadherin shRNA ($c - d$) cell lines. In all images, the scale bar indicates 25 µm.

37 °C and 5% CO_2 (Zeiss Observer.Z1, Zeiss, Goettingen, Germany). An automated stage was used to collect images on both the left and right edge of the cell monolayer for each well every three minutes using a 10× phase-contrast objective.

6.5.5 Image Analysis: Particle Image Velocimetry

Particle Image Velocimetry (PIV) analysis using the MatPIV toolbox (J. Kristian Sveen, GNU general public license) for MATLAB (MathWorks, Inc.) was used to extract velocity information from time-lapse images, as previously described [117]. Multiple iterations of interrogation window sizes were used (two iterations of 64×64 pixel windows followed by two iterations of 32×32 pixel windows). At each interrogation step a 50% overlap was used; outliers were detected using a signal-to-noise filter. The resulting flow fields capture all motion within the collective cell sheet and provide motion information on a scale smaller than an individual cell. The resulting PIV vectors capture displacements on a time scale of three minutes.

The leading edge of the cell sheet was found using custom segmentation code in MATLAB. Phase-contrast images of the monolayer were passed through a Sobel filter to emphasize edges. A median filter and morphological opening were used to clean up the edge image before finding the perimeter of the resulting binary images. The edge coordinates were then found using a MATLAB implementation of Dijkstra's algorithm ("dijsktra path finder" by Sebastien PARIS, available on the MATLAB File Exchange at mathworks.com). Both the left and right edge of the monolayer were found over time, and their relative positions were determined

from the microscope stage data. Together, these two edges could be fit to a circle that determines an effective radius and center of the roughly circular monolayer over time. A schematic of these calculations is shown in Figure 6.19. Radial displacement values were calculated by subtracting the effective radius at $t = 0h$ from the effective radius at $t = 10h$.

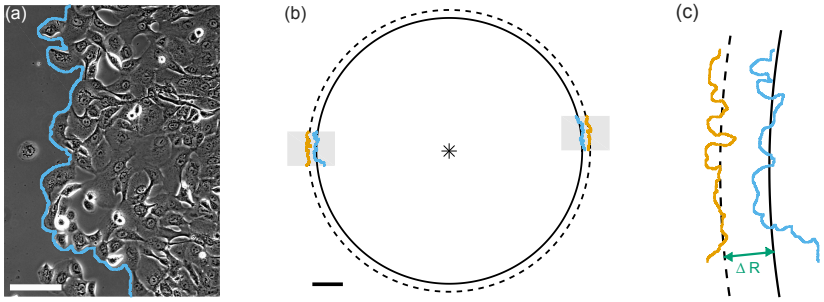

Figure 6.19: **Edge Detection and Analysis** Phase-contrast images of the cell monolayer were segmented to find the leading edge of migration, as shown by the edge overlay in (a); the scale bar indicates 100 µm. Cells or small clumps of cells that were not attached to the main monolayer were not contained within the edge. For each monolayer, images were taken of both the left and right edge of the monolayer. The imaging field of view is represented by gray rectangles in (b). The blue lines represent the segmented monolayer edge at $t = 0h$ and the orange lines represent the segmented monolayer edges at $t = 10h$. These edges are fit to a circle, shown by a solid line ($t = 0h$) or dashed line ($t = 10h$). The scale bar in (b) shows 500 µm. A close-up view of the left edge (c) shows the change in edge position over time, denoted by the radial displacement (ΔR). The monolayers have a radius of approximately 2–3 mm and a ΔR of a few hundred microns over $10h$ (see Figure 6.1).

6.5.6 Migration Analysis

Angle distributions refer to the direction of the PIV velocity vectors with respect to radial expansion; the angle of the ith velocity vector, θ_i, is given by the

inverse tangent of the velocity vector components in polar coordinates, as shown in Equation 6.1. This metric thus captures short-time behavior on a scale of three minutes.

$$\theta_i = tan^{-1}(\frac{v_{rotational}}{v_{radial}}) \tag{6.1}$$

Angular deviation was calculated as $\sqrt{2(1-z)}$ where z is defined in Equation (6.2) and N is the number of velocity vectors within the flow fields being analyzed. Angular deviation therefore ranges from zero (aligned velocity vectors) to $\sqrt{2}$ (highly uncoordinated velocity vectors).

$$z = \frac{1}{N}[(\sum_{i=1}^{N} \cos\theta_i)^2 + (\sum_{i=1}^{N} \sin\theta_i)^2]^{1/2} \tag{6.2}$$

Finite-time Lyapunov exponents (FTLEs) were calculated as previously described [117]. Briefly, FTLE values were calculated by computationally moving virtual tracer particles through the experimentally determined PIV flow field. We followed the tracer motion through the evolving PIV flow field for a deformation time of two hours. If the deformation time was long enough, the FTLE values asymptotically approach Lyapunov exponents [103]; we experimentally found that FTLE values in this system approach an asymptotic value after 2 hours. The tracer particles were initiated on the PIV grid points but were allowed to move off the grid as the flow field evolved. At the end of this time period, we calculated the logarithm of the largest eigenvalue of the Cauchy-Green strain tensor for each cluster of four tracers that were initially neighbors; this is the local FTLE value. Effectively, this quantity measures how tracer particles passively flowing in the collective cell sheet move apart from each other over time. Those tracers that move apart exponentially

are sensitive to initial conditions and indicate regions of possibly chaotic flows. As the FTLE measurements are on the length scale of the PIV flow field, these measurements include both cell body motion and subcellular motion such as membrane ruffling. Thus, the FTLE values represent the chaotic nature of the cell monolayer as a whole. By repeating this analysis for multiple starting frames of the deformation, we measure the evolution of FTLE values over time.

Fluctuation time scales were calculated from a coarse graining of the flow field as described previously [83]. The PIV flow field was averaged over increasing time intervals and the variance of the rotational velocity calculated. The variance decreases with increasing time interval and can be fit to an exponential decay to calculate a characteristic time scale (t_c) describing flow fluctuations, as was shown by Marel et al. [83]. In our work, we fit the experimental variance σ to the exponential defined in Equation 6.3. The second term of Equation 6.3 accounts for the variability due to inaccuracy in the microscope stage. The movable stage in our multi-position imaging has a finite accuracy in returning to a position; the variance this introduces can be expected to decrease with the central limit theorem. In this theorem, variance decreases with the square root of the number of samples—in our case the frame number—which introduces a term with a characteristic time scale $t_{imaging}$.

$$\sigma = Ae^{-t/t_c} + \frac{B}{\sqrt{t/t_{imaging}}} + C \tag{6.3}$$

Spatial correlations were calculated for each individual frame of the PIV flow field and then averaged over one hour to study the change in spatial correlation over

time. Correlations were calculated as

$$C(\Delta r) = \frac{\sum_{r_i} v_r(r_i) * v_r(r_i + \Delta r)}{[\sum_{r_i} v_r^2(r_i) * \sum_{r_i} v_r^2(r_i + \Delta r)]^{\frac{1}{2}}} \tag{6.4}$$

where v_r refers to radial velocity. An example of the variability over time in the correlation values is shown in Figure 6.20.

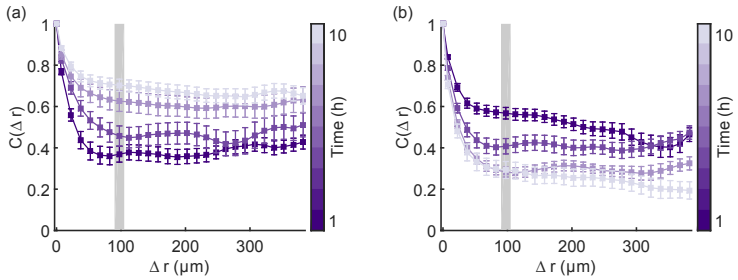

Figure 6.20: Representative spatial correlations for radial velocity of the M1 (a) and M4 (b) cell lines over time show two distinct migration phenotypes. Variation in correlation values are shown for a subset of the curves in Figure 6.5. Color indicates time with earlier hours in dark purple and the end of the experiment in light purple. Error bars indicate 95% confidence intervals.

For all figures, paired experiments are those time-lapse images that were captured on the same day from different wells of the same 12 well plate. Paired differences refer to the M1 cells subtracted from the M4 cells or the relevant nonsense (NS) shRNA cell line subtracted from the corresponding E-cadherin shRNA cell line. Error bars indicate 95% confidence intervals. Distributions are cumulative over all time frames and spatial location. Slopes, where mentioned, were calculated from a linear fit of the data.

Chapter 7: Outlook

The work presented in this thesis has focused on the dynamics of cell migration. Understanding the guidance of cell movement—whether by the underlying migration substrate or by neighboring cells—could lead to better understanding and treatment of diseases such as cancer. In Chapter 3, we showed that individual breast epithelial cells can be guided by the topography of the migration surface; when placed on ridges with features similar to collagen fibers, the cells migrated preferentially along the length of the ridges. We also found that the internal actin machinery of epithelial cells, which is involved in cell migration, is guided by the ridge structures.

To explore the collective dynamics that arise from interactions between migrating cells, we developed tools based on particle image velocimetry (PIV) to extract motion information from time lapse images of migrating cell sheets. This technique facilitated our comparison between experimental migration data and a simulation of collective migration, presented in Chapter 4. We found that collective behavior can change on the scale of a cell monolayer that contains hundreds or thousands of cells. These large-scale changes, however, do not rely on large-scale gradients or subpopulations of cells near the edge of the monolayer. We instead find that changing the activity of individual cells or manipulating the sensing of a preferred migra-

tion direction (discussed further in Section 7.2.1) can lead to increased collective behavior.

Collective behavior also includes interesting localized dynamics. In Chapter 5 we compared epithelial sheets to granular systems and found that cells are able to rearrange within the sheet at high densities, in contrast to what would be expected in inanimate systems. We also compared epithelial sheets to fluid flows and used finite time Lyapunov exponents to measure the chaotic character of the cell sheet. We further used this tool in Chapter 6 to compare the migration of non-malignant and malignant cells. We found that non-malignant cells became more collective over time while malignant cells remained uncoordinated over the ten hours of imaging. We further explored this behavior by decreasing the expression of E-cadherin, a cell-cell adhesion molecule. As discussed in Chapter 6, we found that decreasing E-cadherin expression decreased collective behavior on the short time scale, but non-malignant cells were still able to increase coordination in their motion over time.

7.1 Analysis Applications

The analysis tools we have developed are not limited to the experimental systems described in the previous chapters. PIV is a flexible analysis technique that can be used with or without fluorescent markers. PIV has some limitations, including the assumption of a continuous medium, which makes it inappropriate for use on images of individual migrating cells. There are many experimental systems, however, that follow the motion of cell monolayers. Because PIV does not rely on a

fluorescent marker, these techniques could be applied directly to time-lapse images of primary cells. These motion analysis tools could also be applied to large-scale wound healing assay data sets, such as those created in the biomedical industry.

We have already begun to use these tools to look at changes in collective behavior induced by lysophosphatidic acid (LPA) signaling. The time-lapse imaging data for this project was collected in Carole Parent's lab by Christina Stuelten. Our preliminary migration analysis indicates increased collective behavior in malignant MCF10CA1a (M4) cells upon LPA addition—the cells become slower and more directional after stimulation. These results also suggest an interesting extension of the edge detection algorithm used with our PIV analysis. Preliminary analysis of the edge dynamics in this system suggests decreased fluctuations in edge features after LPA addition, as shown in Figure 7.1.

We have also shared our analysis techniques with the Min Zhao lab at the University of California Davis School of Medicine. They have used PIV to investigate collective behavior in corneal epithelium monolayers. They find that as the monolayer migrates, the leading edge retains a higher speed than the monolayer bulk, but cells away from the leading edge become increasingly directional over time (Figure 7.2). Preliminary work in their lab suggests that calcium signaling plays a role in this collective behavior.

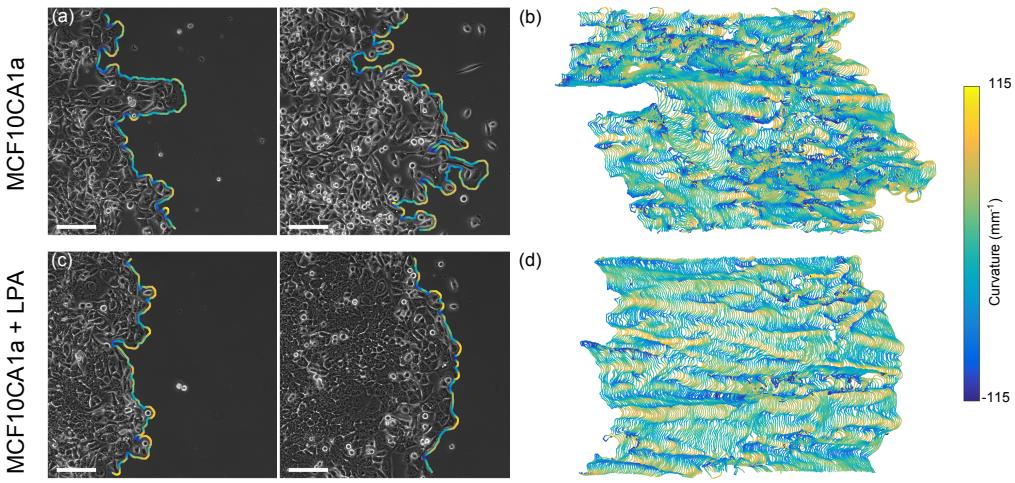

Figure 7.1: Over nine hours, the leading edge of a MCF10CA1a cell monolayer changes shape both globally and locally (a). A kymograph of the edge labeled by the local curvature shows that local features change over the course of nine hours (b). When the MCF10CA1a cells are treated with LPA, the edge morphology becomes more regular (c) and features of the edge are more clearly seen in the edge kymograph (d). The scale bar in the phase contrast images indicates 100 µm.

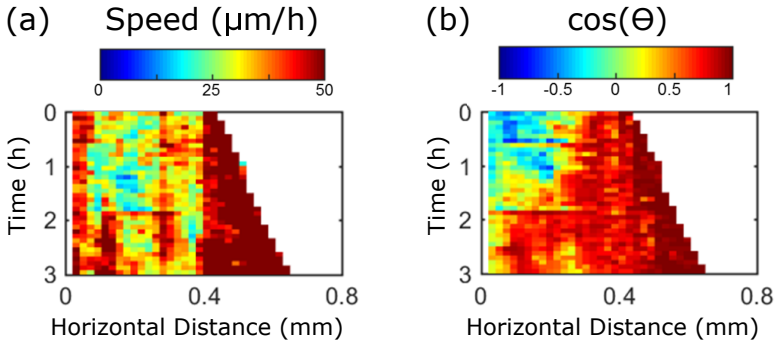

Figure 7.2: The data is this figure was taken by Yan Zhang in the Min Zhao lab at the University of California Davis School of Medicine. Kymographs of the PIV flow fields from a migrating corneal epithelium layer show higher speed at the edge of the monolayer (a) and increasing directional motion throughout the monolayer over time (b).

7.2 Connecting Individual and Collective Migration

7.2.1 Polarity

The simulations discussed in Chapter 4 suggest that the strength of biomechanical polarity within an individual cell can influence collective migration behavior. This raises the question of how to experimentally measure polarity while simultaneously probing collective behavior. Polarity has been studied in collective sheets using markers such as the location of the microtubule organizing center (MTOC) [154] or the Golgi apparatus [91] with respect to the nucleus. The localization of these markers as a signal of polarity may vary, however, due to migration conditions or the state of the cell; the MTOC has been shown to localize in front of the nucleus in some studies of leukocyte migration, but it has often been found behind the nucleus in other studies [155].

The type of polarity modeled in Chapter 4, however, does not correspond to a particular biochemical marker of polarity and instead represents the preferred direction of motion within the cell which may result from a combination of signaling pathways and mechanical inputs from the environment. In this sense, actin dynamics, such as those discussed in Chapter 3, could be used as a marker of the preferred motility direction. As discussed in Section 2.1, actin allows cells to put forth protrusions that lead to cell migration. The localization and motion of actin within a cell may therefore reflect its preferred direction of motion.

In the MCF10A cells discussed in Chapter 3, actin dynamics can be seen on time scales of seconds and minutes, but cell-size motion of the cell body occurs on a time scale of hours. This range of time scales presents challenges for imaging both actin dynamics and cell motion simultaneously. To measure localization, it may be sufficient to image actin infrequently (on a time scale comparable to cell migration) and look at large-scale changes in actin and cell shape. Although it would require more difficult imaging, fast, high-resolution imaging of actin followed by slow imaging of cell body motion could link actin dynamics to migration behavior. Cells with larger fluctuations in their actin dynamics would be expected to exhibit less persistent migration. High temporal resolution imaging of actin has the advantage of providing additional information about actin nucleation and polymerization propagation.

Such imaging could provide a comparison between polarity on the ridge structures discussed in Chapter 3 and flat substrates. It could also be used to explore differences between unperturbed cell migration on various substrates and the behavior seen when inhibitors such as latrunculin, which binds actin monomers and leads to the disruption of actin filaments, are applied to the cell. The actin dynamics and localization seen in individual cells could then be compared to collective behavior under the same conditions to probe the relationship between the observed actin polarity and collective coordination. Actin dynamics could also be imaged in cell sheets, as interactions with neighboring cells will contribute to actin dynamics. Imaging actin within cell sheets such as those described in this thesis will also pose imaging challenges; it may be difficult to determine accurate cell shapes in sheets in

which cells not only touch but also often overlap their edges. However, fluctuations of the overall actin field may still provide interesting information about polarity within the system.

7.2.2 Collective Migration and Contact Guidance

The ability to image actin dynamics within a cell sheet will also be useful in extending the work on contact guidance discussed in Chapter 3 to epithelial sheets such as those analyzed in Chapters 5 and 6. There is evidence in the literature that cell sheets can also be guided by ridge-like structures [65], but there remain questions about how such guidance changes the emergent collective dynamics of the cell sheet. Surface topography can guide the individual cells within a monolayer, but the changes it induces in actin likely also change the way in which cells interact. The PIV filtering steps described in Appendix A will need to be adapted for a background containing topographic structures, but the collective dynamics metrics developed in this thesis can otherwise be directly applied to this system for studies of changes in collective behavior.

The comparison of dynamics on flat surfaces, topography oriented in the direction of collective motion, and topography oriented perpendicular to the monolayer boundary will provide interesting insight into how cells balance the cues received from the substrate with forces exerted by neighboring cells. We have taken preliminary data on the collective response to nanotopgraphy that shows the interplay of these two forces. In these images that were taken of the same system 20 hours

apart, a MCF10A monolayer is migrating towards a set of ridged structures, highlighted by the blue lines in Figure 7.3(a). Before reaching the structures, cells at the edge of the monolayer balance a force leading to migration into the empty area with their adhesion to the cell monolayer; the resulting balance is such that cells maintain a large contact area with neighboring cells despite directional migration outwards. When the monolayer reaches the ridge structures however, the balance shifts as cells on the nanotopography receive additional cues guiding them into the empty space. Some of the cells at the edge, indicated by the blue arrows in Figure 7.3, elongate in the direction of guidance and lose some of their contact area with neighboring cells.

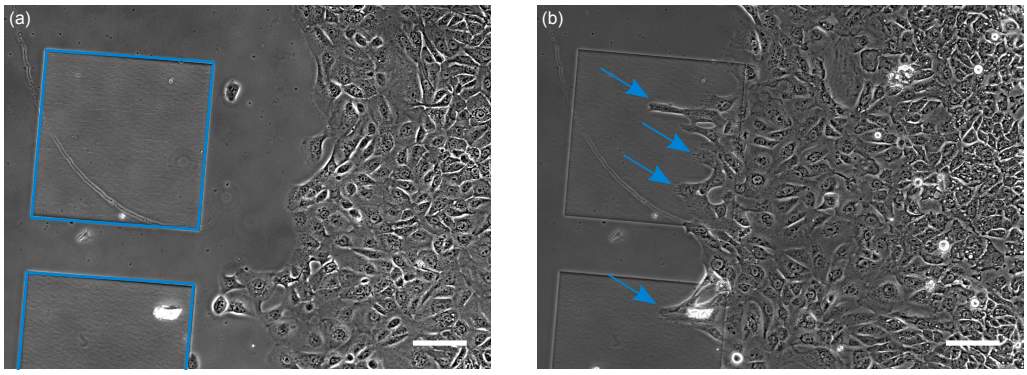

Figure 7.3: (*a*) An MCF10A cell monolayer migrates towards a set of ridge structures, outlined in blue. (*b*) Twenty hours later, the leading edge has reached the structures and individual cells begin to elongate along the ridges, as highlighted by the blue arrows. In both images, the scale bar indicates 100 µm.

The balance between surface cues and forces between neighboring cells is particularly interesting during cancer. There is evidence of changes in the collagen structure around breast tumors [10, 11], and the way in which a particular tumor

cell type prioritizes the cues in its environment may influence the route taken to metastasis. The collective dynamics of MCF10A and MCF10CA1a, which were characterized in Chapter 6, provide an interesting starting point for comparisons in collective contact guidance. This analysis could be also extended to other cell lines to explore further signatures of malignant and metastatic behavior. The image analysis and dynamical tools here could also be applied to measure the contact guidance of primary cells as a prognostic tool.

Appendix A: Particle Image Velocimetry Software Guide

This appendix describes a code suite, *PIV_main*, that was used in Chapters 4 and 6 to analyze time lapse images of cell sheets. A previous version of this code was also used in the analysis in Chapter 5. The code described in this appendix uses particle image velocimetry (PIV) to analyze time-lapse, phase-contrast images and also provides further analysis of the resulting flow fields. Some discussion of this analysis is provided in the Materials and Methods sections of Chapters 4, 5, and 6, but is included here as well for clarity.

PIV was developed in the field of fluid flows and its implementation reflects this history. The algorithm assumes a continuous medium, so images of individual cells or sheets of cells with large gaps are not appropriate for analysis by this method. The implementation described here assumes that the motion is two-dimensional, so it is also not appropriate to use this code on imaging data with three-dimensional motion. An example of images that would fail in this way is provided in the *Example_Images* folder; *2014-11-15-EcadshM1-0023_A1-C.zvi* intially shows reasonable images, but over time it develops three-dimensional structures which cannot be analyzed.

A.1 Overview and Basic Use

The code suite *PIV_main* includes a script, `main_batch_script.m`, that is optimized for processing large data sets of time-lapse images in the Zeiss microscope format (*zvi* files). The script expects the data to include both the left and right edges of a cell monolayer so that the monolayer size can be extracted. The components of this batch script are less restrictive and can be used separately for PIV calculations and further analysis on a variety of data types. This section describes the basic use of `main_batch_script.m` and describes conceptually the analysis which it contains.

The batch script has been optimized for ease of use and convenience when analyzing a specific data set type. The image file names are expected to contain a common wording which distinguishes the cell monolayers, and the file names are expected to end in 'L', 'R', or some version of 'C', 'C1', 'C2', and so forth to indicate the left, right, and center regions of the monolayer, respectively. A set of images from a single monolayer is provided in the folder *Example_Images* for use in learning this code. When the script is run, first each individual *zvi* file is run through the following:

- PIV Calculations: This step analyzes the phase-contrast images and provides flow fields as output.
- PIV Filtering: This step removes non-cell regions from flow fields near the edge of the cell monolayer.
- Edge Detection: This step segments the leading edge of the cell monolayer.

- FTLE Calculation: This step calculates the divergence of tracer particles within the PIV flow and saves the resulting FTLE values.

After these steps are complete, the script provides the user with a series of '*filter check*' images which show a comparison between the PIV filtering step and the edge detection step, discussed further in Section A.6. The remaining sections of the script pull together the edges and center of the monolayer to analyze the cell sheet as one system. The analysis includes:

- PIV Analytics: This section outputs simple metrics from the PIV files such as speed and directionality.
- PIV Time Analytics: This section outputs trends over time in the PIV files.
- FTLE Analytics: This section outputs statistics and trends in the FTLE data.
- Coarse Graining: This section calculates characteristic time and length scales in the flow, as described in [83] and used in Chapter 6.

A.1.1 Running the Batch Script

To run `main_batch_script.m`, the user is required to set a small subset of parameters. Other parameters, which may be changed for other data types, are discussed in later sections describing the individual analysis components. The parameters that must be set in the batch script are:

- `my_email`: This variable must be a valid email address in the format of string. The script sends this email address updates and error messages.

- `directories`: This variable specifices the folders in which the script will look for *zvi* files. Multiple directories can be specified and the script will sequentially analyze each folder.

- `pause_length`: This variable, measured in seconds, was added to the code to allow the user to start the code with a delay (for example, while waiting for files to transfer from a microscope system to the analysis computer).

- `frameskip`: This value tells the script how often to plot the verification images in the edge detection and filter check steps. For example, if set to 25, the code will overlay the edge on the original images every 25 frames.

- `user_firstframe` and `user_lastframe`: The later analysis steps will only include the motion information contained between the `user_firstframe` and `user_lastframe` time points of the data. The value of `user_lastframe` can be set to `inf` to analyze all available frames.

- `r_scale`: This variable sets the spatial scale of the images in µm per pixel.

- `t_scale`: This varaible sets the time scale of the time lapse imaging in minutes.

- `pos_type`: This variable is used to extract microscope stage positions from the imaging data. The stage locations are used to preserve meaningful spatial data in the analysis steps. If an Excel sheet in the Zeiss microscope format is available with position data (an example file is availble in the *Example_Images* folder), set `pos_type = 1`. If the Excel file is not available, `pos_type = 0` will extract the positions from the *zvi* files using a slower process. This part

of the code is not compatible with other data types, but it could be made so if other types of metadata were available.

- `over_write`: This variable tells the code whether to repeat analysis on data sets which have already been analyzed. If `over_write = 0`, no data will be overwritten, but if `over_write = 1`, the PIV analysis, PIV time analysis, FTLE analysis, and coarse graining calculations will be repeated and will replace any existing files.

- `T`: This variable sets the deformation time for the FTLE calculations in frames.

- `trange`: This variable sets the frame range that will be included in the FTLE calculations. It must be less than or equal to the `user_lastframe - T`.

- `parpoolName`: This variable tells MATLAB which parallel pool profile to use for calculations. If no custom profiles are available, use the value `'local'`.

A.2 PIV Calculations

The code that calculates PIV flow fields is contained within a subfolder of *PIV_main* called *PIV*. The core calculations are completed by MatPIV v1.6.1, a PIV toolbox for MATLAB developed by Johan Kristian Sveen and distributed for free under a GNU General Public License (`https://www.mn.uio.no/math/english/people/aca/jks/matpiv/`). The function `dot_matpiv5.m` parses user inputs and passes them into this toolbox. Unlike the strict assumptions built into `main_batch_script.m`, `dot_matpiv5.m` accepts a variety of image formats. The

syntax for using this function is:

```
dot_matpiv5(directory, imname, type, firstframe, lastframe,
channel, num_channel, imname2, savedir)
```

The `directory` and `imname` variables are required as they describe the images to be analyzed. The image `type` variable defaults to `'zvi'`, but will also accept multiple image *tif* files and images sequences in any MATLAB supported image file type. The variable `firstframe` defaults to 1 and `lastframe` defaults to the number of images found in the image file or sequence. If the image file or sequence of files contans multiple channels, the variables `channel` and `num_channel` can be used to select a specific set of images; both are set to default values of 1. Because these variables select a regularly spaced subset of images, they can also be used to manipulate the Δt between analysis frames. If the image type is a series of images where a second string is necessary to specify the correct files, `imname2` can be used for clarity, but the default is to set the value to `[]`. Finally, the output of `dot_matpiv5` is a *.mat* file, which is by default saved to the image directory, but the location can be changed using the optional variable `savedir`.

If images of the type `'zvi'` are specified, the subfunction `bfopen4PIV.m` is used to read the image files. This function is a modified version of the `bfopen.m` function available from the Open Microscope Environment (OME, `https://www.openmicroscopy.org`). All subfunctions and files need for use of `bfopen4PIV.m` are provided in the *PIV_main* folder.

The default variables for these inputs are hard-coded parameters listed at the

top of the function file. The function `dot_matpiv5.m` also contains four additional hard-coded parameters which are used in the image processing. The first variable, `top_cut`, removes a set number of pixels from the top of the imaging field of view. This value has been set to 50 due to an error in image recording encountered in the imaging data used in this thesis; the microscope used does not correctly record the top 50 rows of pixels of each image. For future use, modifying the code to `top_cut=0` will keep all portions of the image. The remaining parameters are used in the implementation of the MatPIV toolbox. The window sizes for the mutliple iterations of the algorithm (described further below) are set to `win1 = 64` and `win2 = 32` and the overlap of the interogation windows is set as `overlap = 0.5`.

After parsing the user inputs and loading the images, `dot_matpiv5.m` converts the images to 8-bit (as is required by the MatPIV toolbox) using the function `rescale_image.m`, which stretches the image to the full 2^8 range of an 8-bit image. The image is then run through a Sobel filter using the function `sobel.m`, which emphasizes edges and features within the phase contrast image that will effectively become the tracer particles used in traditional PIV calculations. A pair of images are then fed into `matpiv.m`, which is the main function the MatPIV toolbox. The function `matpiv.m` is used with multiple iterations of the algorithm, first with the larger window size specified by the parameter `win1` and then, using that output as a guide, the alogrithm is run again using interogation windows with size `win2`. If `overlap` is set to 0.5, the final size of of the PIV grid will be half the size of `win2`. As a rule of thumb, there should be approximately 10 tracer particles (in this case, image features) in a square region with side length `win2`, and motion should be

approximately one fourth of the window size per frame [81].

After the images are run through the function `matpiv.m`, they are filtered and interpolated using other functions from the MatPIV toolbox. The raw flow field is filtered based on the signal-to-noise ratio for each vector using `snrfilt.m`; the signal-to-noise ratio is a meaure of how strong the detected correlation was compared to other correlations considered as matches. All values less than 1.3 are removed and are interpolated back into the flow field using `naninterp.m`. All of these steps are repeated across all time consecutive pairs in the full image set; this is implemented in parallel using `parfor`, which is a function of MATLAB's parallel processing toolbox.

The final output is saved in a structure, `dot_piv`, which is subsequently saved in the `savedir` directory with the name `imnamedot_piv.mat`, where the string corresponding to `imname` is used in the filename. This file contains both the raw and signal-to-noise ratio filtered flow fields, as well as all input variables used in the processing. All of the flow fields in this file are saved in units of pixels per frame. The saved structure also retains information about the signal-to-noise ratio (`snr`) and correlation peak height (`pkh`), which can be used in assessing the quality of the PIV flow fields.

A.3 PIV Filtering

For time lapse images at the edge of the cell monolayer, there are regions of empty space within the field of view. In these regions, the PIV flow fields are neither

reliable nor interesting, so `main_batch_script.m` includes a filtering step that sets all non-cell regions of the flow field to `NaN` (not a number), which keeps them from influencing the eventual analysis of the flow fields. The function which accomplishes the filtering is `mask_and_filter.m`, of the form:

```
dot_piv_filtered = mask_and_filter(dot_piv, size_exclude,
erode_size, save_dir)
```

The first input is the structure `dot_piv`, which is the output of `dot_matpiv5.m`. The remaining outputs are optional and defaults are set within `mask_and_filter.m`. This function also hard-codes the parameter `top_cut=50`, as described in Section A.2. Information about the images is read from the metadata within the `dot_piv` structure, and the images are loaded into the function `cell_area_filter.m` within a `parfor` loop for faster processing. This function is of the form:

```
im_out = cell_area_filter(im,size_exclude,erode_size)
```

The output, `im_out`, is a binary image with value 1 at the location of cells and value 0 everywhere else. The processing in this function is based on Sobel filtering and it can be additonally cleaned up using the `size_exclude` parameter, which removes small objects in the image (default value is 1200) and `erode_size`, which erodes the image to remove objects such as out of focus features (the default is no erosion). This function can be adapted for future use by changing these parameters or by adding additional morphological operators to the processing steps.

The binary image is fed into `filter_piv_cell_area.m`, which interpolates the binary image to the size of the PIV grid. The filtered PIV flow field output is NaN

anywhere the mask is zero but retains the original PIV value in all other locations. This filtered structure, still named `dot_piv` for simplicity of future processing, is saved as `imnamedot_piv_filtered.mat`.

The filtering process is run on all monolayer edges as identified by file naming conventions in `main_batch_script.m`, and the filtered file is the version used in all further processing. It is not recommended to run the filtering on images in the center of a monolayer; `cell_area_filter.m` will attempt to distinguish an non-cell region in the image which is not there, resulting in the loss of useful flow field data.

The folder *PIV* also contains a function `plot_piv_pcolor.m`, which is not used in the batch script, but can be used to plot the PIV data. This function creates an image for each frame of the PIV data with speed shown in color under a quiver plot of the flow field. Optional inputs change the units of the plotted results as well as the color axis scale and the size of the plotted arrows (see Figure A.1).

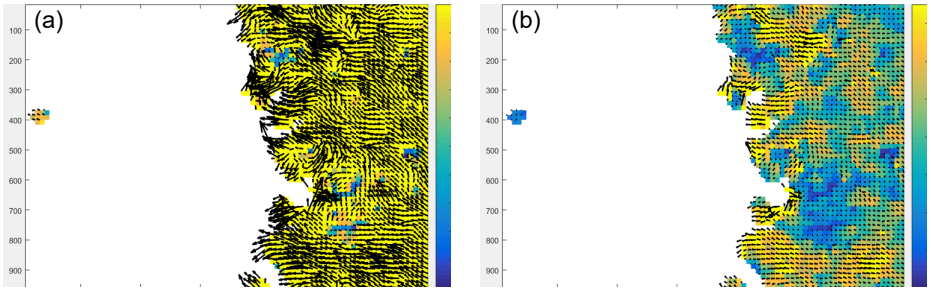

Figure A.1: Figures of the PIV flow fields from the A1-L example data were created using `plot_piv_pcolor.m`. Using the default parameters gives output in pixels per frame (a). Using additional input parameters, the data is converted to µm per minute and a better scaling is chosen for the color axis; the output of `plot_piv_pcolor(dot_piv, 0, 0.75, 0.65, 3, 20)` is shown in (b).

A.4 Edge Detection

Edge detection in the batch script uses `sheet_edger_combo.m`, which is based on an edge detection algorithm developed by a previous undergraduate student in the lab, Peter Kordell. This function is of the form:

```
edgedat = sheet_edger_combo(imname, directory, im_format,
intframe, finframe, diskrad, threshm, thresh_in, threshs,
savedir, frameskip, saveimpose)
```

The first two inputs, `imname` and `directory`, are required and specify the image file as described in previous sections. The image format must be specified using `im_format`. The first and last frames of analysis can be specified using `intframe` and `finframe`. Several of the inputs specify morpohological operatations performed on the images: `diskrad` determines the radius of the disk used to morphologically open the image (default value 12), `threshm` specifies a method for generating a mask from the image (the default is `'auto'`, which uses Otsu thresholding), `thresh_in` specifies a user defined threshhold if the `'manual'` method is selected, and `threshs` sets a bias in the thresholding of the image (the default is zero, which specifies no bias). The variable `savedir` specifies where the output file, `edgedat.mat`, will be saved, and the `frameskip` variable specifies how frequently to create an overlay image (shown in Figure A.2(a)), which is saved to the `saveimpose` directory.

Images are parsed using `sheet_edger_combo.m` and fed into `open_edger.m`, which creates a binary image similar to that described in Section A.3. This binary

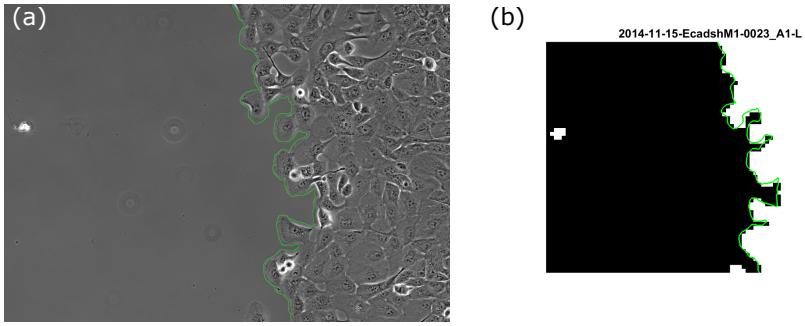

Figure A.2: (a) After the edge is segmented, the detected monolayer edge is overlaid on the original image for verification. (b) The filter check step compares the edge segmentation to the cell areas found during PIV filtering.

image is fed into `mexdijkstra.m`, which uses Dijkstra's method to find the coordinates of the edge of the monolayer (implemented using "dijsktra path finder" by Sebastien PARIS, available on the MATLAB File Exchange at mathworks.com). To use this function, before running the edge detection for the first time on a system, run `mexme_dijkstra.m` to compile the source code on your system. On occasion, the `mexdijkstra.m` function returns an empty set, in which case a more robust but slower function, `matdijkstra.m`, attempts to find the edge.

The main function, `sheet_edger_combo.m`, allows for edges not to be found in some frames (often due to debris or scattered cells) while still continuing to analyze future frames. This function stops processing if the cells have touched the far edge. This function was originally intended for globally straight edges that only traveled in the horizontal directon. Future improvements to the code could loosen these requirements and allow for vertical motion of the cells or better memory usage. It is recommended that the user check the edge overlay images saved to the `saveimpose`

folder to ensure that the processing found the actual cell edge. It should also be confirmed that the calculations did not stop early due to a bug which sometimes includes a single pixel in the edge detection that touches the far edge.

A.5 FTLE Calculations

The next processing step for `main_batch_script.m` is to calculate FTLE values from the PIV flow fields generated in the previous steps. This step uses the function `stretchg.m`, which was developed by Douglas Kelly. This function calculates the largest eigenvalue of the Cauchy-Green strain tensor for a cluster of four tracers that were initially neighbors; in this case we use the PIV grid as the starting location for the tracer particles, although the tracers may later move off the grid. The square root of this eigenvalue gives the stretching field for the input flow field, and the logrithm of the stretching field divided by the deformation time gives the finite time Lyapunov exponent [103]. After this calculation is complete, the edges of the FTLE field are set to `NaN` to remove edge effects. The FTLE values for a given directory are saved in a cell array, `ftle_all`, which is then saved as `ftle_all.mat`.

A.6 Interpreting the Filter Check Output

At this point in the processing provided by `main_batch_script.m`, MATLAB will wait for the user to confirm before continuing. When the script continues, it will create figures that show binary images of the PIV filtering mask that are overlaid with a line representing the edge dection output, as shown in Figure A.2(b). These

two images should show a similar boundary, although the PIV filtering has the resolution of the PIV grid while the edge detection has pixel level resolution. These images allow the user to screen for large regions that were removed incorrectly or remain but should have been removed. They also allow the user to screen for large regions of scattered cells outside the detected edge which may influence results.

A.7 Analysis Sections of the Batch Script

After the user has reviewed the filter check images, `main_batch_script.m` begins to analyze the PIV flow fields. This is the section of the batch script that most heavily depends on the file naming convention; the left and right edges will be used to determine a monolayer size, assuming a circular monolayer. This allows metrics to be analyzed as a function of distance from the monolayer center.

A.7.1 Basic Analytics

The first analysis is run through the function `basic_analyticsMultiC.m`. The role of `basic_analyticsMultiC.m` is to parse data inputs and set up formatting for saving the output to a Excel file summary for each directory. The calculations are accomplished by the function `piv_analyticsMultiC.m`, which is contained in the *Analytics* subfolder. This subfunction has several outputs and creates several figures; it is of the form:

```
[ang_dev, mean_speed, SEM_speed, deltaR, firstframe, lastframe]
= piv_analyticsMultiC(directory, imname, r_scale, t_scale,
```

```
user_firstframe, user_lastframe, pos_list)
```

The input variables to this function are the same as described in Section A.1.1 for `main_batch_script.m`. PIV calculations, PIV filtering, and edge detection must be run before using this function. The first output is `ang_dev`, a three element vector which reports the angular deviation for the entire monolayer, the edge of the monolayer, and the center of the monolayer. Angular deviation provides a measure of directionality spread within the sheet. The function `calc_ang_dev.m` performs the following calculation for the angular deviaton:

```
function ang_dev = calc_ang_dev(angles)
term1 = sum(cos(angles(~isnan(angles))))/numel(find(~isnan(angles)));
term2 = sum(sin(angles(~isnan(angles))))/numel(find(~isnan(angles)));
R = sqrt(term1.^2 + term2.^2);
ang_dev = sqrt(2*(1-R));
```

Similarly, `mean_speed` and `SEM_speed` are three element vectors which report the mean speed and the standard error of the mean in the same three regions. The output `deltaR` is the change in the monolayer size from the first to last frame, in µm. Although the user gives desired frame ranges in the input variables, these ranges may not be possible with the given edge detection data (for example if the cells touched the edge before the user expected). The final output variables `firstframe` and `lastframe` give the actual frame range used in the calculations.

The function `piv_analyticsMultiC.m` contains several hard-coded parameters that influence plotting styles and set cutoffs used in the analysis. These param-

eters are saved in a single structure, `param`, which is saved with the output data file. The first two entries, `param.edge_cut = 0.75` and `param.center_cut = 0.5`, set the cutoffs used for determing those regions of the sheet that are included in 'edge' and 'center' measurements; they are measured in fractions of the monolayer size, R. The function creates kymographs (Figure A.3(a,b)), and four parameters influence this plotting: `param.r_step = 50` sets the size of regions which are averaged for the kymograph, `param.numel_limit = 42` sets the minimum number of vectors needed to keep a bin in the kymograph, `param.speed_limits = [0 .7]` sets the color scale limits on the speed kymograph, and `param.cos_limits = [-1 1]` sets the color limits on the kymograph of directionality. For the direction histograms (i.e. rose plots) created by the script, `param.angle_bins = 20` sets the number of bins in the plot and `param.rose_limit = 0.25` sets the axis limit on the rose plot (Figure A.3(c)). For the plots of metrics versus radial locations (plotted versus the scaled location r/R, as described in Chapters 4 and 5), `param.R_bin_size = 0.05` sets the size of the bins in units of r/R, `param.R_bin_max = 1` sets the maximum r/R bin to plot (values greater than 1 will included scattered cells in front of the monolayer edge, which may not be desired), and `param.size_limit = 1100` sets the number of vector values needed to keep a bin in the plot.

The first task for `piv_analyticsMultiC.m` is to use the edge detection data to fit the monolayer edges to a circle, which gives the monolayer a coordinate system (see Figure 6.19 for a schematic). The function `do_edgedat_to_circleMultiC.m` outputs the center and radius of the monolayer as well as the positons of each imaging location in the monolayer. This subfunction requires either an excel file

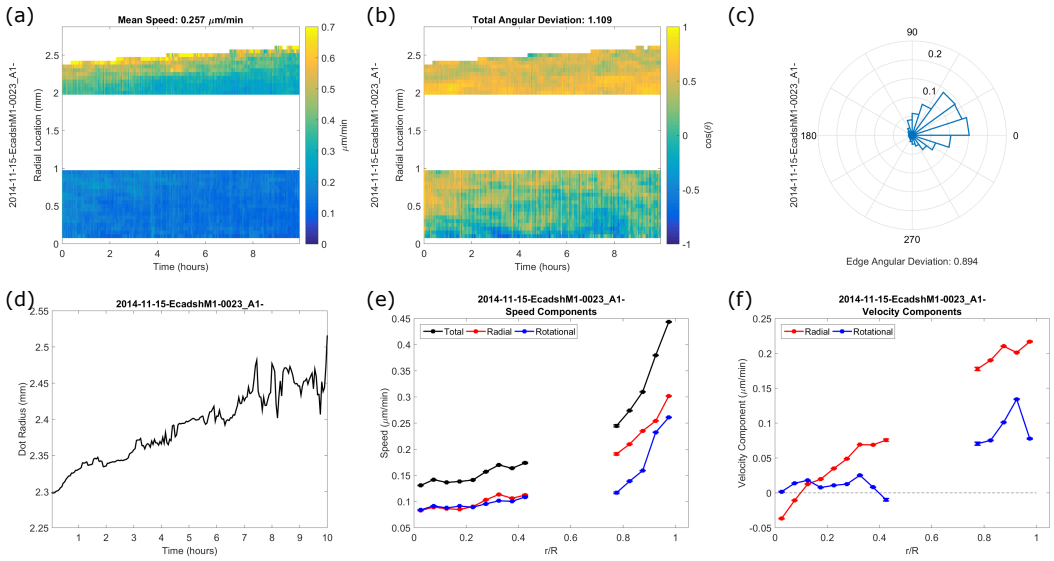

Figure A.3: The function `piv_analyticsMultiC.m` creates kymographs of speed (a) and $\cos\theta$ (b) across the imaging fields of view. Three rose plots showing velocity direction are created; the plot for the edge of the monolayer is shown in (c). Monolayer size over time is shown in (d). Radial plots of speed (e) and velocity (f) show trends in motion across the monolayer.

of positions or a *zvi* file type; future improvements could add compatability with other metadata types. The monolayer edges are fit to a circle using the subfunction `circfit.m`. In addition to the function outputs, `do_edgedat_to_circleMultiC.m` saves a file in a subdirectory made within the imaging directory (*Analytics Data*) with the file name `imname_dot_RvsT.mat` so that future analytics code does not needlessly repeat these calculations. In this case, `imname` is the image filename with the end designation of L, R, C, etc. removed (a single file is saved for each monolayer).

The circle fitting information is then fed into `do_scale_shift_MultiC.m`. This function combines the `dot_piv` structures from the left and right edges and

the center of the monolayer into a single set of flow field matrices which have been converted into units of µm per minute. Because the monolayer is assumed to be circular, many of the calculations are done on the radial velocity, `v_r`, and rotational velocity, `v_th`, which are calculated as:

```
v_r = (u.*x + v.*y)./r;

v_th = (-u.*y + v.*x)./r;
```

The first figures created by `piv_analyticsMultiC.m` are kymographs of the overall cell speed (Figure A.3(a)) and of $\cos(\theta)$ (Figure A.3(b)), where θ is defined as the angle between `v_r` and `v_th`. These figures are made with the function `plot_kymo.m`, which is also included in the *Analytics* code folder. The function then creates rose plots that show a normalized histogram of velocity directions in either the whole monolayer, the edge of the monolayer (Figure A.3(c)), or the center of the monolayer. These figures are made with the function `rose_normal2.m`, which normalizes the plots such that the area under the curve is one. The analytics function also creates a figure showing changes in the radial size of the monolayer (R) over time (Figure A.3(d)). All of these figures are saved in a subfolder in the images directory, *Analytics Figures*.

The `piv_analyticsMultiC.m` function then bins speed and velocity metrics by r/R and creates two figures showing the trends across the scale of the monolayer. One figure shows the speed values, which are always positive and indicate how much motion was detected in the radial direction, in the rotional directon, or in all directions (Figure A.3(e)). The other figure shows velocity values, which can

be negative, and as such tend to average to zero in those regions with undirected motion (Figure A.3(f)). This section saves a file to the image directory's *Analytics Data* folder with the file name `imname_vel_comp.mat`.

Finally, `piv_analyticsMultiC.m` save an additional file into the *Analytics Data* folder with the file name `imnameAnalytics.mat` which contains the function output variables as well as the parameters used in the previous calculations.

A.7.2 PIV Time Analytics

The batch script next runs `piv_analytics_timeMultiC.m` over the PIV files. This function either reads in the previously created `imname_dot_RvsT.mat` file or uses the same calculations as `piv_analyticsMultiC.m` to obtain flow fields in the monolayer reference frame. This function bins the flow fields by time and creates two figures. One figure shows overall speed as well as component velocity over time (Figure A.4(a)), while the other shows the angular deviation over time for the edge and center of the monolayer (Figure A.4(b)). These figures are saved into the same *Analytics Figures* described previously, and the binned values are saved as `imname_time_analytics.mat` in the *Analytics Data* folder.

A.7.3 FTLE Analytics

The function `run_ftle_analyticsMultiC.m` is similar to the previously described function `basic_analyticsMultiC.m` in that it parses data inputs and sets up formatting for saving an output file. The subfunction `ftle_analyticsMultiC.m`

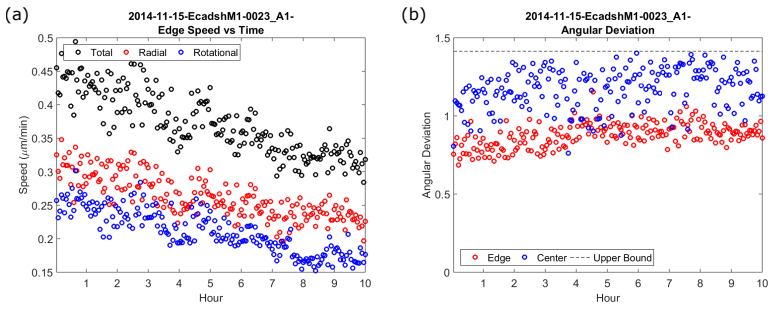

Figure A.4: The PIV time analytics code creates plots of speed (a) and angular deviation (b) over time.

completes the analysis and is of the form:

```
[mean_ftle, SEM_ftle, per_pos, firstframe, lastframe] =
ftle_analyticsMultiC(directory, imname, ftleLRC, r_scale,
t_scale, user_firstframe, user_lastframe)
```

The input variables have been previously described. The output variable `mean_ftle` is a three component vector representing the mean FTLE value for the entire monolayer, the edge of the monolayer, and the center of the monolayer. Similarly, `SEM_ftle` and `per_pos` are three element vectors which describe the standard error of the mean FTLE values and the percent of FTLE values which are positive. The percent positive values are one indication of chaotic motion.

This function includes hard coded parameters similar to those described previously. Again the cutoffs for the center and edge are set by `param.edge_cut` and `param.center_cut`. Bins for the histogram figures are set by `param.ftle_bins`. The kymograph parameters are set using `param.R_bin_size`, `param.R_bin_max`, and `param.size_limit`. Parameters for the spatial location plots are set using

param.r_step, param.numel_limit, and param.heat_limits.

The function ftle_analyticsMultiC.m uses either imname_dot_RvsT.mat or do_edgedat_to_circleMultiC.m to fit the monolayer to a circle. It then uses function do_scale_shift_ftleMultiC.m to output a combined matrix of FTLE values which have been converted to units of hours^{-1}. The analysis function uses plot_kymo.m to create a kymograph of FTLE values (Figure A.5(a)), which is saved to the *FTLE Analytics* folder in the image directory. Figures are also created showing the distribution of FTLE values at the edge, in the center, and across the entire monolayer (Figure A.5(b)). The data are binned verus r/R; both the mean value (Figure A.5(c)) and percent positive are plotted with the binned data saved as imname_ftle_vs_r.mat in the *FTLE Analytics* folder. The data are then separately binned by time, creating figures for the mean and percent postive values (Figure A.5(d)); these data are saved as imnameFTLE_time_Analytics.mat. Finally, the output data and the parameters used in analysis are saved as imnameFTLEAnalytics.mat.

A.7.4 Coarse Graining

The function run_coarse_grain_MultiC.m is used to organize files for the analysis run by coarse_grain_MultiC_sqrt.m. This function is of the form:

```
[l_c, t_c, pR, pT] = coarse_grain_MultiC_sqrt(directory, imname,
final_frame_user, r_scale, t_scale)
```

The input variables are the same as those discussed previously. The output from the function includes a characteristic length scale, l_c, and a characteristic

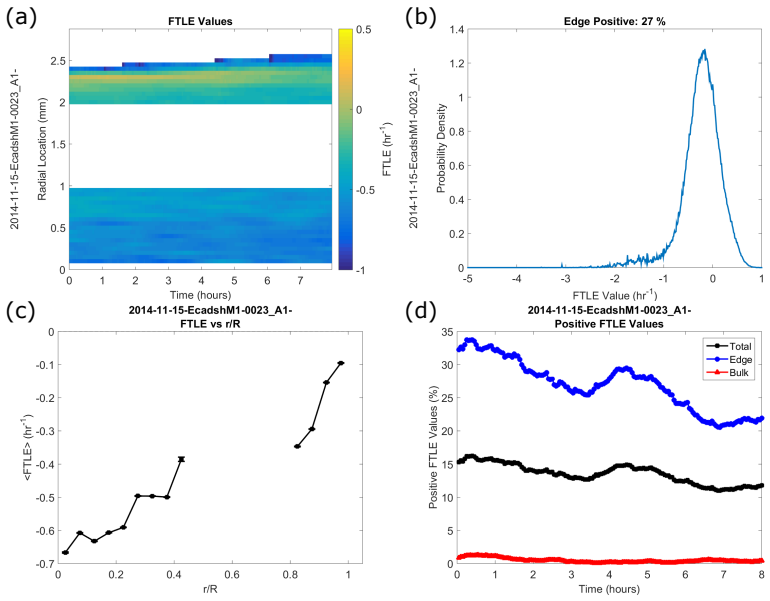

Figure A.5: The FTLE analytics code creates a kymograph of FTLE values (a). Distributions of FTLE values are also created; the distribution of values at the edge is shown in (b). FTLE values (c) and percent positive FTLE values (not shown) are plotted against radial location. Both the percent positive FTLE values (d) and average value (not shown) are also plotted versus time.

time scale, `t_c`, describing fluctations in the flow field. The variables `pR` and `pT` provide the fitting parameters used in calculating the spatial and temporal scales. Additional parameters within the `coarse_grain_MultiC_sqrt.m` function are the sizes over which the grid is spatially (`r_sizes`) and temporally (`t_sizes`) coarse grained. The parameter `edge_cut = 0.75` also is used in this function.

First, `coarse_grain_MultiC_sqrt.m` performs a spatial coarse graining. The flow fields are coarsened by the function `coarse_grain_grid_r.m`, which averages neighboring values on a grid. The rotational velocity variance is calculated and the decreasing variance is fit to an exponential with an offset. The fit uses the MATLAB

function `lsqnonlin` and a subfunction of the coarse graining file, `expweight0`, which is of the form:

```
function diff = expweight0(p,X,Y)

fitY = p(2)*exp(-X/p(1))+p(3);

raw_diff = fitY - Y;

diff = raw_diff.*sqrt(W);
```

The fit is weighted by the inverse of the time variance in the rotational velocity variance. A figure of the fit is created (Figure A.6(a)) and saved to the *Coarse Test* subfolder within the imaging directory (W in the above equation).

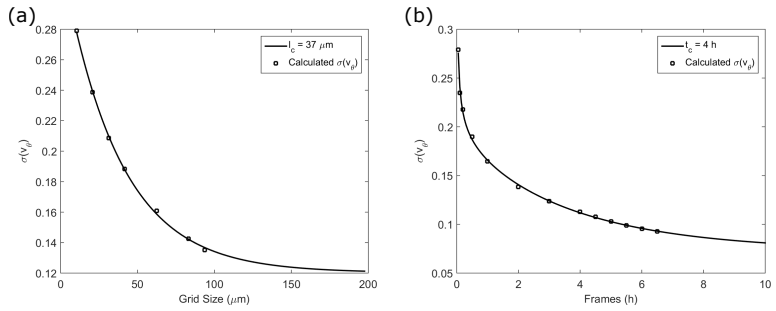

Figure A.6: Variance in the flow field decreases as it is averaged spatially (a) or over time (b), from which characteristic length and time scales of fluctuations are calculated.

The original flow fields are then coarse grained in time using the function `coarse_grain_grid_t.m`, which averages over time. A similar weighted fit using `lsqnonlin` and the rotational velocity variance is again calculated, but the fit is to an offset exponential with an additional square root term to account for central limit theorm contributions from microscope state jitter. This fitting is done using

the subfunction `sqrtexpweight`, which reads:

```
function diff = sqrtexpweight(p,X,Y)

fitY = p(2)*exp(-X/p(1)) + p(3)./sqrt(X/(t_scale/60)) + p(4);

raw_diff = fitY - Y;

diff = raw_diff.*sqrt(W);
```

A figure of this fit (Figure A.6(b)) is also saved to the *Coarse Test* folder. The fitted data, the fitting parameters, and function input parameters are all saved to the *Coarse Test* folder in a file `imname_coarse_data.mat`. This is the final analysis step included in `main_batch_script.m`.

A.8 Other Analysis Scripts

The *PIV_main* folder also contains batch scripts, discussed here, which provide additional information about the PIV flow fields.

A.8.1 Distribution Figures

The script `batch_plot_piv_time_hist.m` organizes data and input parameters for use by the function `plot_piv_time_hist.m`. This function creates data files that can be used to look at distributions of speed and velocity direction, such as those shown in Chapter 6. The batch requires the input of `directories`, `r_scale`, `t_scale`, `firstframe`, and `user_lastframe`, which are used as in the previous sections. The function `plot_piv_time_hist.m` contains the additional parameters `param.edge_cut` and `param.center_cut`, which were described in Section A.7.1.

The script also uses `param.speed_bins` and `param.ang_bins` as the bins in the distribution plots. The code also bins the distributions by time to look for dynamic trends and `param.time_bin` sets the size of these bins.

The flow fields from the left, right, and center of the monolayer are combined as described previously. The speed and velocity angles are binned using the previously described parameters, and a figure for each showing the change in the distributions over time is saved to the imaging directory subfolder *PIV Hist* (see Figure A.7(a)). The speed and angle matrices from the combined monolayer are saved for those values in the edge region; this file is `imnamePIV_edge.mat`, which is saved in the *PIV Hist* folder.

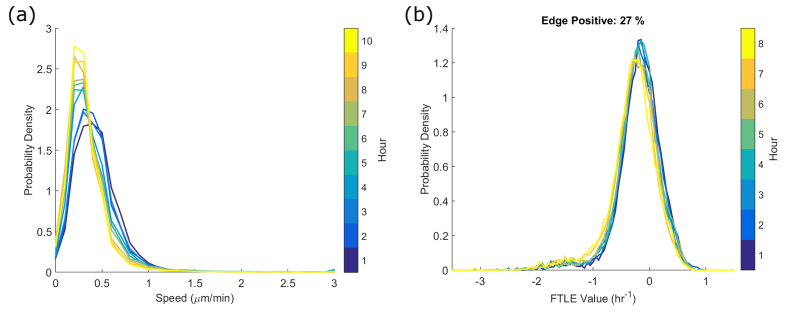

Figure A.7: Speed distributions over time as created by `batch_plot_piv_time_hist.m` are shown in (*a*). The distribution of FTLE values shown in (*b*) was created using `batch_ftle_hist.m`.

A similar batch script, `batch_ftle_hist.m` creates distributions and figures for the FTLE values using the function `ftle_time_hist_MultiC.m`. This function creates distribution figures for the center, edge, and entire monolayer using `plot_ftle_pdf_time.m` (see Figure A.7(b)). These figures are saved within the *FTLE Analytics* folder, as is the data file `imnameFTLE_edge.mat`.

A.8.2 Spatial Correlations

Additional code to calculate spatial correlations is included in the *Correlations* folder. The script `batch_piv_spatial_corr.m` organizes data and inputs to calculate spatial correlations from PIV flow fields; all user parameters in this script have been described previously. This batch script calls `piv_corr_r_NaNnorm.m`, which has standard input parameters. The function also uses the hard-coded `param.edge_cut` and `param.center_cut` variables described previously. An additional parameter, `max_dist`, sets the maximum distance at which correlations are calculated (in µm); it can be set to `inf` to use as much data as the image allows, but this is not recommended. The processing is relatively slow, and at larger distances, the statistics of the correlation decrease. After combining data from the imaging fields of view into single flow field variables, the data are passed into `correlatePIV_r_NaNnorm.m`, which is of the form:

```
correlatePIV_r_NaNnorm(piv_values, x, y, t_scale, r_scale,
sub_mean, lastframe, max_dist, savedir, title_text)
```

The variable `piv_values` is a matrix containing the metric of interest to be correlated—`piv_corr_r_NaNnorm.m` runs three separate correlations on speed, radial velocity, and rotational velocity. Additional correlations can be simply added within this function. The variables `x` and `y` set the locations of the matrix entries in `piv_values`; these variables should already be in units of µm. The variable `t_scale` allows the data to be binned by time and is in units of minutes. The variable `sub_mean` allows the user to choose whether to subtract the mean; a value of 0 (the

default) does not subtract the mean. The `lastframe` and `max_dist` variables give time and spatial limits to the data analyzed. The correlation figures and data files are saved to the folder `savedir`. The optional variable `title_text` adds a title to the figures (in `piv_corr_r_NaNnorm.m`, this title is used to label the metric analyzed). The additional parameters `ylim_to_use` (axis limit of the plots), `r_bin_size` (bin size of the correlations), and `time_bin` (bin size for time trends in the correlation) are set within the `correlatePIV_r_NaNnorm.m` function.

The function first calculates all possible distances using the given `x` and `y` matrices. The correlations are calculated by sptatial bin and plots are created of the mean correlation as well as the time trend in the correlations (Figure A.8). The correlation data is saved to a file specified by the `savedir` variable.

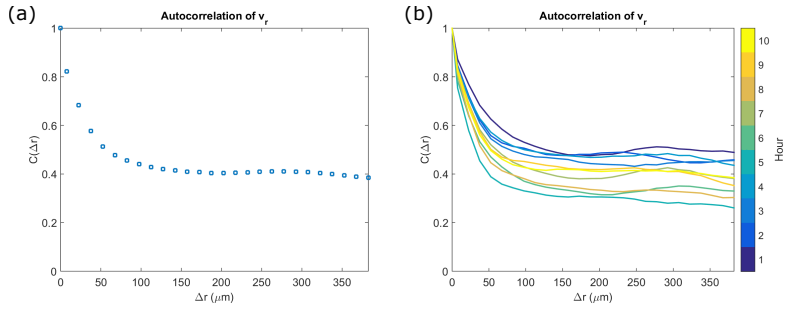

Figure A.8: Figures of the time-averaged spatial correlation of radial velocity (a) and time trends in this correlation (b) are created using `batch_piv_spatial_corr.m`. Similar figures for speed and rotational velocity are also created (not shown).

Bibliography

[1] American Cancer Society. *Cancer Facts & Figures 2016*. American Cancer Society, Atlanta, 2016.

[2] Scott Valastyan and Robert A. Weinberg. Tumor metastasis: molecular insights and evolving paradigms. *Cell*, 147(2):275–292, 2011.

[3] Jennie Dusheck. Oncology: Getting physical. *Nature*, 491(7425):S50–S51, 2012.

[4] David B. Agus and Franziska Michor. The sciences converge to fight cancer. *Nature Physics*, 8(11):773–774, 2012.

[5] Franziska Michor, Jan T. Liphardt, Mauro Ferrari, and Jonathan Widom. What does physics have to do with cancer? *Nature Reviews Cancer*, 11(9):657–670, 2011.

[6] Matthias L. Zorn, Anna-Kristina Marel, Felix J. Segerer, and Joachim O. Rädler. Phenomenological approaches to collective behavior in epithelial cell migration. *Biochimica et Biophysica Acta (BBA) - Molecular Cell Research*, 1853(11, Part B):3143 – 3152, 2015.

[7] Robert W. Style, Yonglu Che, Su Ji Park, Byung Mook Weon, Jung Ho Je, Callen Hyland, Guy K. German, Michael P. Power, Larry A. Wilen, John S. Wettlaufer, and Eric R. Dufresne. Patterning droplets with durotaxis. *Proceedings of the National Academy of Sciences*, 110(31):12541–12544, 2013.

[8] Guillaume Charras and Erik Sahai. Physical influences of the extracellular environment on cell migration. *Nature Reviews Molecular Cell Biology*, 15(12):813–824, 2014.

[9] Dennis E. Discher, Paul Janmey, and Yu-Li Wang. Tissue cells feel and respond to the stiffness of their substrate. *Science*, 310(5751):1139–1143, 2005.

[10] Paolo P. Provenzano, Kevin W. Eliceiri, Jay M. Campbell, David R. Inman, John G. White, and Patricia J. Keely. Collagen reorganization at the tumor-stromal interface facilitates local invasion. *BMC medicine*, 4(1):38, 2006.

[11] Matthew W. Conklin, Jens C. Eickhoff, Kristin M. Riching, Carolyn A. Pehlke, Kevin W. Eliceiri, Paolo P. Provenzano, Andreas Friedl, and Patricia J. Keely. Aligned collagen is a prognostic signature for survival in human breast carcinoma. *The American Journal of Pathology*, 178(3):1221–1232, 2011.

[12] Peter Friedl and Darren Gilmour. Collective cell migration in morphogenesis, regeneration and cancer. *Nature Reviews Molecular Cell Biology*, 10(7):445–457, 2009.

[13] Peter Friedl, Joseph Locker, Erik Sahai, and Jeffrey E. Segall. Classifying collective cancer cell invasion. *Nature Cell Biology*, 14(8):777–783, 2012.

[14] Nicola Aceto, Aditya Bardia, David T. Miyamoto, Maria C. Donaldson, Ben S. Wittner, Joel A. Spencer, Min Yu, Adam Pely, Amanda Engstrom, Huili Zhu, Brian W. Brannigan, Ravi Kapur, Shannon L. Stott, Toshi Shioda, Sridhar Ramaswamy, David T. Ting, Charles P. Lin, Mehmet Toner, Daniel A. Haber, and Shyamala Maheswaran. Circulating Tumor Cell Clusters Are Oligoclonal Precursors of Breast Cancer Metastasis. *Cell*, 158(5):1110–1122, 2014.

[15] Kevin J. Cheung, Veena Padmanaban, Vanesa Silvestri, Koen Schipper, Joshua D. Cohen, Amanda N. Fairchild, Michael A. Gorin, James E. Verdone, Kenneth J. Pienta, Joel S. Bader, and Andrew J. Ewald. Polyclonal breast cancer metastases arise from collective dissemination of keratin 14-expressing tumor cell clusters. *Proceedings of the National Academy of Sciences*, 113(7):E854–E863, 2016.

[16] Markus Basan, Jens Elgeti, Edouard Hannezo, Wouter-Jan Rappel, and Herbert Levine. Alignment of cellular motility forces with tissue flow as a mechanism for efficient wound healing. *Proceedings of the National Academy of Sciences*, 110(7):2452–2459, 2013.

[17] Raghu Kalluri and Robert A. Weinberg. The basics of epithelial-mesenchymal transition. *The Journal of Clinical Investigation*, 119(6):1420–1428, 2009.

[18] Douglas Hanahan and Robert A. Weinberg. Hallmarks of Cancer: the Next Generation. *Cell*, 144(5):646–674, 2011.

[19] Anna Bagorda, Vassil A. Mihaylov, and Carole A. Parent. Chemotaxis: moving forward and holding on to the past. *Thrombosis and Haemostasis*, 95(1):12–21, 2006.

[20] Cornelis J. Weijer. Collective cell migration in development. *Journal of Cell Science*, 122(18):3215–3223, 2009.

[21] Eric Theveneau and Roberto Mayor. Neural crest delamination and migration: From epithelium-to-mesenchyme transition to collective cell migration. *Developmental Biology*, 366(1):34–54, 2012.

[22] Paul Martin. Wound Healing — Aiming for Perfect Skin Regeneration. *Science*, 276(5309):75–81, 1997.

[23] Tim Lämmermann, Philippe V. Afonso, Bastian R. Angermann, Ji Ming Wang, Wolfgang Kastenmüller, Carole A. Parent, and Ronald N. Germain. Neutrophil swarms require LTB4 and integrins at sites of cell death in vivo. *Nature*, 498(7454):371–375, 2013.

[24] Peter Friedl and Katarina Wolf. Tumour-cell invasion and migration: diversity and escape mechanisms. *Nature Reviews Cancer*, 3(5):362–374, 2003.

[25] Pieta K. Mattila and Pekka Lappalainen. Filopodia: molecular architecture and cellular functions. *Nature Reviews Molecular Cell Biology*, 9(6):446–454, 2008.

[26] Martin Bergert, Stanley D. Chandradoss, Ravi A. Desai, and Ewa Paluch. Cell mechanics control rapid transitions between blebs and lamellipodia during migration. *Proceedings of the National Academy of Sciences*, 109(36):14434–14439, 2012.

[27] Kimberly M. Stroka, Hongyuan Jiang, Shih-Hsun Chen, Ziqiu Tong, Denis Wirtz, Sean X. Sun, and Konstantinos Konstantopoulos. Water Permeation Drives Tumor Cell Migration in Confined Microenvironments. *Cell*, 157(3):611–623, 2014.

[28] Xiaoyu Sun, Meghan K. Driscoll, Can Guven, Satarupa Das, Carole A. Parent, John T. Fourkas, and Wolfgang Losert. Asymmetric nanotopography biases cytoskeletal dynamics and promotes unidirectional cell guidance. *Proceedings of the National Academy of Sciences*, 112(41):12557–12562, 2015.

[29] Daniel A. Fletcher and R. Dyche Mullins. Cell mechanics and the cytoskeleton. *Nature*, 463(7280):485–492, 2010.

[30] Thomas D. Pollard and John A. Cooper. Actin, a Central Player in Cell Shape and Movement. *Science*, 326(5957):1208–1212, 2009.

[31] Jun Allard and Alex Mogilner. Traveling waves in actin dynamics and cell motility. *Current Opinion in Cell Biology*, 25(1):107–115, 2013.

[32] Paolo Maiuri, Jean-François Rupprecht, Stefan Wieser, Verena Ruprecht, Olivier Bénichou, Nicolas Carpi, Mathieu Coppey, Simon de Beco, Nir S. Gov, Carl-Philippe Heisenberg, Carolina Lage Crespo, Franziska Lautenschlaeger, Maël Le Berre, Mathew Lennon-Dumenil, Ana-Maria Raab, Hawa-Racine

Thiam, Mathieu Piel, Michael Sixt, and Raphaël Voituriez. Actin Flows Mediate a Universal Coupling between Cell Speed and Cell Persistence. *Cell*, 161(2):374–386, 2015.

[33] Charlotte Guetta-Terrier, Pascale Monzo, Jie Zhu, Hongyan Long, Lakshmi Venkatraman, Yue Zhou, PeiPei Wang, Sing Yian Chew, Alex Mogilner, Benoit Ladoux, and Nils C. Gauthier. Protrusive waves guide 3D cell migration along nanofibers. *The Journal of Cell Biology*, 211(3):683–701, 2015.

[34] Marco Antunes, Telmo Pereira, João V Cordeiro, Luis Almeida, and Antonio Jacinto. Coordinated waves of actomyosin flow and apical cell constriction immediately after wounding. *The Journal of Cell Biology*, 202(2):365–379, 2013.

[35] Bartlomiej Waclaw, Ivana Bozic, Meredith E. Pittman, Ralph H. Hruban, Bert Vogelstein, and Martin A. Nowak. A spatial model predicts that dispersal and cell turnover limit intratumour heterogeneity. *Nature*, 525(7568):261–264, 2015.

[36] Michael J. Mitchell and Michael R. King. Fluid shear stress sensitizes cancer cells to receptor-mediated apoptosis via trimeric death receptors. *New Journal of Physics*, 15(1):015008, 2013.

[37] Mingyang Lu, Mohit Kumar Jolly, Herbert Levine, José N. Onuchic, and Eshel Ben-Jacob. MicroRNA-based regulation of epithelial-hybrid-mesenchymal fate determination. *Proceedings of the National Academy of Sciences*, 110(45):18144–18149, 2013.

[38] Thomas Brabletz. To differentiate or not — routes towards metastasis. *Nature Reviews Cancer*, 12(6):425–436, 2012.

[39] Jingyu Zhang, Xiao-Jun Tian, Hang Zhang, Yue Teng, Ruoyan Li, Fan Bai, Subbiah Elankumaran, and Jianhua Xing. TGF-β-induced epithelial-to-mesenchymal transition proceeds through stepwise activation of multiple feedback loops. *Science Signaling*, 7(345):ra91, 2014.

[40] Jeff H. Tsai, Joana Liu Donaher, Danielle A. Murphy, Sandra Chau, and Jing Yang. Spatiotemporal regulation of epithelial-mesenchymal transition is essential for squamous cell carcinoma metastasis. *Cancer Cell*, 22(6):725–736, 2012.

[41] Herbert D. Soule, Terry M. Maloney, Sandra R. Wolman, Ward D. Peterson Jr., Richard Brenz, Charles M. Mcgrath, Jose Russo, Robert J. Pauley, Richard F. Jones, and S. C. Brooks. Isolation and Characterization of a Spontaneously Immortalized Human Breast Epithelial Cell Line, MCF-10. *Cancer Research*, 50(18):6075–6086, 1990.

[42] Fred R. Miller, Herbert D. Soule, Larry Tait, Robert J. Pauley, Sandra R. Wolman, Peter J. Dawson, and Gloria H. Heppner. Xenograft Model of Progressive Human Proliferative Breast Disease. *Journal of the National Cancer Institute*, 85(21):1725–1732, 1993.

[43] Peter J. Dawson, Sandra R. Wolman, Larry Tait, Gloria H. Heppner, and Fred R. Miller. MCF10AT: a model for the evolution of cancer from proliferative breast disease. *The American Journal of Pathology*, 148(1):313–319, 1996.

[44] Mitsutaka Kadota, Howard H. Yang, Bianca Gomez, Misako Sato, Robert J. Clifford, Daoud Meerzaman, Barbara K. Dunn, Lalage M. Wakefield, and Maxwell P. Lee. Delineating genetic alterations for tumor progression in the MCF10A series of breast cancer cell lines. *PLoS One*, 5(2):e9201, 2010.

[45] Patrick G. Shaw, Raghothama Chaerkady, Tao Wang, Shauna Vasilatos, Yi Huang, Bennett Van Houten, Akhilesh Pandey, and Nancy E. Davidson. Integrated proteomic and metabolic analysis of breast cancer progression. *PLoS One*, 8(9):e76220, 2013.

[46] Steven J. Santner, Peter J. Dawson, Larry Tait, Herbert D. Soule, James Eliason, Anwar N. Mohamed, Sandra R. Wolman, Gloria H. Heppner, and Fred R. Miller. Malignant MCF10CA1 cell lines derived from premalignant human breast epithelial MCF10AT cells. *Breast Cancer Research and Treatment*, 65(2):101–110, 2001.

[47] Sanjay Kumar and Valerie M. Weaver. Mechanics, malignancy, and metastasis: the force journey of a tumor cell. *Cancer Metastasis Reviews*, 28(1–2):113–127, 2009.

[48] Pengfei Lu, Valerie M. Weaver, and Zena Werb. The extracellular matrix: a dynamic niche in cancer progression. *The Journal of Cell Biology*, 196(4):395–406, 2012.

[49] Melda Tozluoğlu, Alexander L. Tournier, Robert P. Jenkins, Steven Hooper, Paul A. Bates, and Erik Sahai. Matrix geometry determines optimal cancer cell migration strategy and modulates response to interventions. *Nature Cell Biology*, 15(7):751–762, 2013.

[50] Andrew D. Doyle, Francis W. Wang, Kazue Matsumoto, and Kenneth M. Yamada. One-dimensional topography underlies three-dimensional fibrillar cell migration. *The Journal of Cell Biology*, 184(4):481–490, 2009.

[51] Andrew A. Bridges, Maximilian S. Jentzsch, Patrick W. Oakes, Patricia Occhipinti, and Amy S. Gladfelter. Micron-scale plasma membrane curvature is recognized by the septin cytoskeleton. *The Journal of Cell Biology*, 213(1):23–32, 2016.

[52] Meghan K. Driscoll, Xiaoyu Sun, Can Guven, John T. Fourkas, and Wolfgang Losert. Cellular Contact Guidance through Dynamic Sensing of Nanotopography. *ACS Nano*, 8(4):3546–3555, 2014.

[53] Stephanie Alexander, Gudrun E. Koehl, Markus Hirschberg, Edward K. Geissler, and Peter Friedl. Dynamic imaging of cancer growth and invasion: a modified skin-fold chamber model. *Histochemistry and Cell Biology*, 130(6):1147–1154, 2008.

[54] Kevin J. Cheung, Edward Gabrielson, Zena Werb, and Andrew J. Ewald. Collective Invasion in Breast Cancer Requires a Conserved Basal Epithelial Program. *Cell*, 155(7):1639–1651, 2013.

[55] Chun-Chi Liang, Ann Y. Park, and Jun-Lin Guan. In vitro scratch assay: a convenient and inexpensive method for analysis of cell migration in vitro. *Nature Protocols*, 2(2):329–333, 2007.

[56] Djordje L. Nikolić, Alistair N. Boettiger, Dafna Bar-Sagi, Jeffrey D. Carbeck, and Stanislav Y. Shvartsman. Role of boundary conditions in an experimental model of epithelial wound healing. *American Journal of Physiology Cell Physiology*, 291(1):C68–C75, 2006.

[57] Michael C. Weiger, Vidya Vedham, Christina H. Stuelten, Karen Shou, Mark Herrera, Misako Sato, Wolfgang Losert, and Carole A. Parent. Real-Time Motion Analysis Reveals Cell Directionality as an Indicator of Breast Cancer Progression. *PLoS One*, 8(3):e58859, 2013.

[58] Xavier Serra-Picamal, Vito Conte, Romaric Vincent, Ester Anon, Dhananjay T. Tambe, Elsa Bazellières, James P. Butler, Jeffrey J. Fredberg, and Xavier Trepat. Mechanical waves during tissue expansion. *Nature Physics*, 8(8):628–634, 2012.

[59] Aaron. S. Meyer, Shannon K. Hughes-Alford, Jennifer E. Kay, Amalchi Castillo, Alan Wells, Frank B. Gertler, and Douglas A. Lauffenburger. 2D protrusion but not motility predicts growth factor-induced cancer cell migration in 3D collagen. *The Journal of Cell Biology*, 197(6):721–729, 2012.

[60] Rizwan Farooqui and Gabriel Fenteany. Multiple rows of cells behind an epithelial wound edge extend cryptic lamellipodia to collectively drive cell-sheet movement. *Journal of Cell Science*, 118(Pt 1):51–63, 2005.

[61] Mathieu Poujade, Erwan Grasland-Mongrain, A. Hertzog, J. Jouanneau, Philippe Chavrier, Benoît Ladoux, Axel Buguin, and Pascal Silberzan. Collective migration of an epithelial monolayer in response to a model wound. *Proceedings of the National Academy of Sciences*, 104(41):15988–15993, 2007.

[62] Thomas E. Angelini, Edouard Hannezo, Xavier Trepat, Jeffrey J. Fredberg, and David A. Weitz. Cell Migration Driven by Cooperative Substrate Deformation Patterns. *Physical Review Letters*, 104(16):168104, 2010.

[63] Claudio G. Rolli, Hidekazu Nakayama, Kazuo Yamaguchi, Joachim P. Spatz, Ralf Kemkemer, and Jun Nakanishi. Switchable adhesive substrates: Revealing geometry dependence in collective cell behavior. *Biomaterials*, 33(8):2409–2418, 2011.

[64] Felix J Segerer, Florian Thürof, Alicia Piera Alberola, Erwin Frey, and Joachim Oskar Rädler. Emergence and Persistence of Collective Cell Migration on Small Circular Micropatterns. *Physical Review Letters*, 22:228102, 2015.

[65] Camila Londono, M. Jimena Loureiro, Benjamin Slater, Petra B. Lücker, John Soleas, Suthamathy Sathananthan, J. Stewart Aitchison, Alexandre J. Kabla, and Alison P. McGuigan. Nonautonomous contact guidance signaling during collective cell migration. *Proceedings of the National Academy of Sciences*, 111(5):1807–1812, 2014.

[66] Tamás Vicsek and Anna Zafiris. Collective motion. *Physics Reports*, 517(3-4):71–410, 2012.

[67] François Graner and James A. Glazier. Simulation of biological cell sorting using a two-dimensional extended Potts model. *Physical Review Letters*, 69(13):2013–2016, 1992.

[68] Jakob Löber, Falko Ziebert, and Igor S Aranson. Collisions of deformable cells lead to collective migration. *Scientific Reports*, 5:9172, 2015.

[69] Shirley Mark, Roie Shlomovitz, Nir S. Gov, Mathieu Poujade, Erwan Grasland-Mongrain, and Pascal Silberzan. Physical model of the dynamic instability in an expanding cell culture. *Biophysical Journal*, 98(3):361–370, 2010.

[70] Marco Salm and Len M. Pismen. Chemical and mechanical signaling in epithelial spreading. *Physical Biology*, 9(2):026009, 2012.

[71] Alberto Puliafito, Lars Hufnagel, Pierre Neveu, Sebastian J. Streichan, Alex Sigal, D. Kuchnir Fygenson, and Boris I. Shraiman. Collective and single cell behavior in epithelial contact inhibition. *Proceedings of the National Academy of Sciences*, 109(3):739–744, 2012.

[72] Xavier Trepat and Jeffrey J. Fredberg. Plithotaxis and emergent dynamics in collective cellular migration. *Trends in Cell Biology*, 21(11):638–646, 2011.

[73] Dapeng Bi, J. H. Lopez, J. M. Schwarz, and M. Lisa Manning. A density-independent rigidity transition in biological tissues. *Nature Physics*, 11(12):1074–1079, 2015.

[74] Andrea J. Liu and Sidney R. Nagel. Nonlinear dynamics: Jamming is not just cool any more. *Nature*, 396(6706):21–22, 1998.

[75] Monirosadat Sadati, Nader Taheri Qazvini, Ramaswamy Krishnan, Chan Young Park, and Jeffrey J. Fredberg. Collective migration and cell jamming. *Differentiation*, 86(3):121–125, 2013.

[76] Guillaume Duclos, S. Garcia, H. G. Yevick, and Pascal Silberzan. Perfect nematic order in confined monolayers of spindle-shaped cells. *Soft Matter*, 10(14):2346–2353, 2014.

[77] Thomas E. Angelini, Edouard Hannezo, Xavier Trepat, Manuel Marquez, Jeffrey J. Fredberg, and David A. Weitz. Glass-like dynamics of collective cell migration. *Proceedings of the National Academy of Sciences*, 108(12):4714–4719, 2011.

[78] Simon Garcia, Edouard Hannezo, Jens Elgeti, Jean-François Joanny, Pascal Silberzan, and Nir S. Gov. Physics of active jamming during collective cellular motion in a monolayer. *Proceedings of the National Academy of Sciences*, 112(50):15314–15319, 2015.

[79] Jin-Ah Park, Jae Hun Kim, Dapeng Bi, Jennifer A. Mitchel, Nader Taheri Qazvini, Kelan Tantisira, Chan Young Park, Maureen McGill, Sae-Hoon Kim, Bomi Gweon, Jacob Notbohm, Robert Steward Jr., Stephanie Burger, Scott H. Randell, Alvin T. Kho, Dhananjay T. Tambe, Corey Hardin, Stephanie A. Shore, Elliot Israel, David A. Weitz, Daniel J. Tschumperlin, Elizabeth P. Henske, Scott T. Weiss, M. Lisa Manning, James P. Butler, Jeffrey M. Drazen, and Jeffrey J. Fredberg. Unjamming and cell shape in the asthmatic airway epithelium. *Nature Materials*, 14(10):1040–1048, 2015.

[80] Dapeng Bi, Xingbo Yang, M. Cristina Marchetti, and M. Lisa Manning. Motility-Driven Glass and Jamming Transitions in Biological Tissues. *Physical Review X*, 6(2):021011, 2016.

[81] Ronald J. Adrian and Jerry Westerweel. *Particle Image Velocimetry*. Cambridge University Press, 2010.

[82] Maxime Deforet, Maria Carla Parrini, Laurence Petitjean, Marco Biondini, Axel Buguin, Jacques Camonis, and Pascal Silberzan. Automated velocity mapping of migrating cell populations (AVeMap). *Nature Methods*, 9(11):1081–1083, 2012.

[83] Anna-Kristina Marel, Matthias L. Zorn, Christoph Klingner, Roland Wedlich-Söldner, Erwin Frey, and Joachim O. Rädler. Flow and Diffusion in Channel-Guided Cell Migration. *Biophysical Journal*, 107(5):1054–1064, 2014.

[84] Benjamin Slater, Camila Londono, and Alison P. McGuigan. An algorithm to quantify correlated collective cell migration behavior. *BioTechniques*, 54(2):87–92, 2013.

[85] Meng-Horng Lee, Pei-Hsun Wu, Jack Rory Staunton, Robert Ros, Gregory D. Longmore, and Denis Wirtz. Mismatch in Mechanical and Adhesive Properties Induces Pulsating Cancer Cell Migration in Epithelial Monolayer. *Biophysical Journal*, 102(12):2731–2741, 2012.

[86] Laurence Petitjean, M. Reffay, Erwan Grasland-Mongrain, Mathieu Poujade, Benoît Ladoux, Axel Buguin, and Pascal Silberzan. Velocity fields in a collectively migrating epithelium. *Biophysical Journal*, 98(9):1790–1800, 2010.

[87] Steven M. Zehnder, Marina K. Wiatt, Juan M. Uruena, Alison C. Dunn, W. Gregory Sawyer, and Thomas E. Angelini. Multicellular density fluctuations in epithelial monolayers. *Physical Review E*, 92(3):032729, 2015.

[88] Sri Ram Krishna Vedula, Man Chun Leong, Tan Lei Lai, Pascal Hersen, Alexandre J. Kabla, Chwee Teck Lim, and Benoît Ladoux. Emerging modes of collective cell migration induced by geometrical constraints. *Proceedings of the National Academy of Sciences*, 109(32):12974–12979, 2012.

[89] Anna-Kristina Marel, Nils Podewitz, Matthias L. Zorn, Joachim Oskar Rädler, and Jens Elgeti. Alignment of cell division axes in directed epithelial cell migration. *New Journal of Physics*, 16(11):115005, 2014.

[90] Grégory Beaune, Tomita Vasilica Stirbat, Nada Khalifat, Olivier Cochet-Escartin, Simon Garcia, Vasily Valérïévitch Gurchenkov, Michael P. Murrell, Sylvie Dufour, Damien Cuvelier, and Françoise Brochard-Wyart. How cells flow in the spreading of cellular aggregates. *Proceedings of the National Academy of Sciences*, 111(22):8055–8060, 2014.

[91] Mei Rosa Ng, Achim Besser, Gaudenz Danuser, and Joan S. Brugge. Substrate stiffness regulates cadherin-dependent collective migration through myosin-II contractility. *The Journal of Cell Biology*, 199(3):545–563, 2012.

[92] Robert W. Style, Rostislav Boltyanskiy, Guy K. German, Callen Hyland, Christopher W. MacMinn, Aaron F. Mertz, Larry A. Wilen, Ye Xu, and Eric R. Dufresne. Traction force microscopy in physics and biology. *Soft Matter*, 10(23):4047, 2014.

[93] Dhananjay T. Tambe, C. Corey Hardin, Thomas E. Angelini, Kavitha Rajendran, Chan Young Park, Xavier Serra-Picamal, Enhua H. Zhou, Muhammad H. Zaman, James P. Butler, David A. Weitz, Jeffrey J. Fredberg, and Xavier Trepat. Collective cell guidance by cooperative intercellular forces. *Nature Materials*, 10(6):469–475, 2011.

[94] Jae Hun Kim, Xavier Serra-Picamal, Dhananjay T. Tambe, Enhua H. Zhou, Chan Young Park, Monirosadat Sadati, Jin-Ah Park, Ramaswamy Krishnan, Bomi Gweon, Emil Millet, James P. Butler, Xavier Trepat, and Jeffrey J. Fredberg. Propulsion and navigation within the advancing monolayer sheet. *Nature Materials*, 12(9):856–863, 2013.

[95] Elsa Bazellières, Vito Conte, Alberto Elosgui-Artola, Xavier Serra-Picamal, María Bintanel-Morcillo, Pere Roca-Cusachs, José J. Muñoz, Marta Sales-Pardo, Roger Guimerà, and Xavier Trepat. Control of cell-cell forces and collective cell dynamics by the intercellular adhesome. *Nature Cell Biology*, 17(4):409–420, 2014.

[96] Kenechukwu David Nnetu, Melanie Knorr, Josef Käs, and Mareike Zink. The impact of jamming on boundaries of collectively moving weak-interacting cells. *New Journal of Physics*, 14(11):115012, 2012.

[97] Brian Utter and R.P. Behringer. Experimental Measures of Affine and Nonaffine Deformation in Granular Shear. *Physical Review Letters*, 100(20):208302, 2008.

[98] Qi Wen, Anindita Basu, Paul A. Janmey, and Arjun G. Yodh. Non-affine deformations in polymer hydrogels. *Soft Matter*, 8(31):8039–8049, 2012.

[99] Dapeng Bi, Jorge H. Lopez, J. M. Schwarz, and M. Lisa Manning. Energy barriers and cell migration in densely packed tissues. *Soft Matter*, 10(12):1885–1890, 2014.

[100] Dandan Chen, Denis Semwogerere, Jun Sato, Victor Breedveld, and Eric R. Weeks. Microscopic structural relaxation in a sheared supercooled colloidal liquid. *Physical Review E*, 81:011403, 2010.

[101] V. Chikkadi and P. Schall. Nonaffine measures of particle displacements in sheared colloidal glasses. *Physical Review E*, 85(3):031402, 2012.

[102] N. Murdoch, B. Rozitis, K. Nordstrom, S. F. Green, P. Michel, T.-L. de Lophem, and Wolfgang Losert. Granular Convection in Microgravity. *Physical Review Letters*, 110(1):018307, 2013.

[103] Shawn C. Shadden, Francois Lekien, and Jerrold E. Marsden. Definition and properties of Lagrangian coherent structures from finite-time Lyapunov exponents in two-dimensional aperiodic flows. *Physica D: Nonlinear Phenomena*, 212(3-4):271–304, 2005.

[104] Greg A. Voth, George Haller, and J. P. Gollub. Experimental Measurements of Stretching Fields in Fluid Mixing. *Physical Review Letters*, 88(25):254501, 2002.

[105] Thomas Peacock and George Haller. Lagrangian coherent structures: The hidden skeleton of fluid flows. *Physics Today*, 66(2):41, 2013.

[106] Venkat Maruthamuthu, Yvonne Aratyn-Schaus, and Margaret L. Gardel. Conserved F-actin dynamics and force transmission at cell adhesions. *Current Opinion in Cell Biology*, 22(5):583–588, 2010.

[107] Malcolm S. Steinberg. Mechanism of tissue reconstruction by dissociated cells, II: Time-course of events. *Science*, 137(3532):762–763, 1962.

[108] Ramsey A. Foty and Malcolm S. Steinberg. The differential adhesion hypothesis: a direct evaluation. *Developmental Biology*, 278(1):255–263, 2005.

[109] Jeffery D. Amack and M. Lisa Manning. Knowing the Boundaries: Extending the Differential Adhesion Hypothesis in Embryonic Cell Sorting. *Science*, 338(6104):212–215, 2012.

[110] Steve Pawlizak, Anatol W. Fritsch, Steffen Grosser, Dave Ahrens, Tobias Thalheim, Stefanie Riedel, Tobias R. Kießling, Linda Oswald, Mareike Zink, M. Lisa Manning, and Josef A. Käs. Testing the differential adhesion hypothesis across the epithelial-mesenchymal transition. *New Journal of Physics*, 17(8):083049, 2015.

[111] Jean-Léon Maître and Carl-Philipp Heisenberg. Three Functions of Cadherins in Cell Adhesion. *Current Biology*, 23(14):R626–R633, 2013.

[112] Clare M. Isacke and Michael A. Horton. *The adhesion molecule factsbook*. Academic Press, second edition, 2000.

[113] F. van Roy and G. Berx. The cell-cell adhesion molecule E-cadherin. *Cellular and Molecular Life Science*, 65(23):3756–3788, 2008.

[114] Emad A. Rakha, Maysa E. El-Sayed, Andrew R. Green, Andrew H. S. Lee, John F. Robertson, and Ian O. Ellis. Prognostic markers in triple-negative breast cancer. *Cancer*, 109(1):25–32, 2007.

[115] Hiroshi Oka, Hitoshi Shiozaki, Kenji Kobayashi, Masatoshi Inoue, Hideaki Tahara, Tetsurou Kobayashi, Yuuichi Takatsuka, Norihisa Matsuyoshi, Shinji Hirano, Masatoshi Takeichi, and Takesada Mori. Expression of E-cadherin cell adhesion molecules in human breast cancer tissues and its relationship to metastasis. *Cancer Research*, 53(7):1696–1701, 1993.

[116] Ruth Heimann, Fusheng Lan, Russell McBride, and Samuel Hellman. Separating Favorable from Unfavorable Prognostic Markers in Breast Cancer: The Role of E-Cadherin. *Cancer Research*, 60(2):298–304, 2000.

[117] Rachel M. Lee, Douglas H. Kelley, Kerstin N. Nordstrom, Nicholas T. Ouellette, and Wolfgang Losert. Quantifying stretching and rearrangement in epithelial sheet migration. *New Journal of Physics*, 15(2):025036, 2013.

[118] Paul W. Kriebel, Valarie A. Barr, and Carole A. Parent. Adenylyl Cyclase Localization Regulates Streaming during Chemotaxis. *Cell*, 112(4):549–560, 2003.

[119] Ryan J. Petrie, Andrew D. Doyle, and Kenneth M. Yamada. Random versus directionally persistent cell migration. *Nature Reviews Molecular Cell Biology*, 10(8):538–549, 2009.

[120] A. S. G. Curtis and Malini Varde. Control of Cell Behavior: Topological Factors. *Journal of the National Cancer Institute*, 33:15–26, 1964.

[121] G.A. Dunn and J.P. Heath. A new hypothesis of contact guidance in tissue cells. *Experimental Cell Research*, 101(1):1–14, 1976.

[122] X.F. Walboomers, H.J.E. Croes, L.A. Ginsel, and J.A. Jansen. Growth behavior of fibroblasts on microgrooved polystyrene. *Biomaterials*, 19(20):1861–1868, 1998.

[123] K. A. Diehl, John D. Foley, P. F. Nealey, and C. J. Murphy. Nanoscale topography modulates corneal epithelial cell migration. *Journal of Biomedical Materials Research Part A*, 75(3):603–611, 2005.

[124] Joshua Zimmerberg and Stuart McLaughlin. Membrane Curvature: How BAR Domains Bend Bilayers. *Current Biology*, 14(6):R250–R252, 2004.

[125] Erik Meijering, Oleh Dzyubachyk, and Ihor Smal. Methods for Cell and Particle Tracking. In *Methods in Enzymology*, volume 504, pages 183–200. Academic Press, 2012.

[126] Ester Anon, Xavier Serra-Picamal, Pascal Hersen, Nils C. Gauthier, Michael P. Sheetz, Xavier Trepat, and Benoît Ladoux. Cell crawling mediates collective cell migration to close undamaged epithelial gaps. *Proceedings of the National Academy of Sciences*, 109(27):10891–10896, 2012.

[127] Maurizio Ventre, Carlo Fortunato Natale, Carmela Rianna, and Paolo Antonio Netti. Topographic cell instructive patterns to control cell adhesion, polarization and migration. *Journal of The Royal Society Interface*, 11(100):20140687, 2014.

[128] Juliane Zimmermann, Ryan L. Hayes, Markus Basan, José N. Onuchic, Wouter-Jan Rappel, and Herbert Levine. Intercellular Stress Reconstitution from Traction Force Data. *Biophysical Journal*, 107(3):548–554, 2014.

[129] Markus Basan, Jacques Prost, Jean-François Joanny, and Jens Elgeti. Dissipative particle dynamics simulations for biological tissues: rheology and competition. *Physical Biology*, 8(2):026014, 2011.

[130] Guy B. Blanchard, Sughashini Murugesu, Richard J. Adams, Alfonso Martinez-Arias, and Nicole Gorfinkiel. Cytoskeletal dynamics and supracellular organisation of cell shape fluctuations during dorsal closure. *Development*, 137(16):2743–2752, 2010.

[131] Philip Vitorino, Mark Hammer, Jongmin Kim, and Tobias Meyer. A steering model of endothelial sheet migration recapitulates monolayer integrity and directed collective migration. *Molecular and Cellular Biology*, 31(2):342–350, 2011.

[132] Indrajyoti Indra, Vishnu Undyala, Casey Kandow, Umadevi Thirumurthi, Micah Dembo, and Karen A. Beningo. An in vitro correlation of mechanical forces and metastatic capacity. *Physical Biology*, 8:015015, 2011.

[133] A. Szabó, K. Varga, T. Garay, B. Hegeds, and András Czirók. Invasion from a cell aggregate-the roles of active cell motion and mechanical equilibrium. *Physical Biology*, 9(1):016010, 2012.

[134] Olivia du Roure, Alexandre Saez, Axel Buguin, Robert H. Austin, Philippe Chavrier, Pascal Silberzan, and Benoît Ladoux. Force mapping in epithelial cell migration. *Proceedings of the National Academy of Sciences*, 102(7):2390–2395, 2005.

[135] Alexandre Saez, Ester Anon, Marion Ghibaudo, Olivia du Roure, J-M. Di Meglio, Pascal Hersen, Pascal Silberzan, Axel Buguin, and Benoît Ladoux. Traction forces exerted by epithelial cell sheets. *Journal of Physics: Condensed Matter*, 22(19):194119, 2010.

[136] Xavier Trepat, Michael R. Wasserman, Thomas E. Angelini, Emil Millet, David A. Weitz, James P. Butler, and Jeffrey J. Fredberg. Physical forces during collective cell migration. *Nature Physics*, 5(6):426–430, 2009.

[137] Tatiana Omelchenko and Alan Hall. Myosin-IXA Regulates Collective Epithelial Cell Migration by Targeting RhoGAP Activity to Cell-Cell Junctions. *Current Biology*, 22(4):278–288, 2012.

[138] Gregory F. Weber, Maureen A. Bjerke, and Douglas W. DeSimone. A Mechanoresponsive Cadherin-Keratin Complex Directs Polarized Protrusive Behavior and Collective Cell Migration. *Developmental Cell*, 22(1):104–115, 2012.

[139] Jin-Hong Kim, Lawrence J. Dooling, and Anand R. Asthagiri. Intercellular mechanotransduction during multicellular morphodynamics. *Journal of the Royal Society Interface*, 7:S341–S350, 2010.

[140] Michael Murrell, Roger D. Kamm, and Paul Matsudaira. Substrate viscosity enhances correlation in epithelial sheet movement. *Biophysical Journal*, 101(2):297–306, 2011.

[141] Kenechukwu David Nnetu, Melanie Knorr, Dan Strehle, Mareike Zink, and Josef A. Käs. Directed persistent motion maintains sheet integrity during multi-cellular spreading and migration. *Soft Matter*, 8:6913–6921, 2012.

[142] B. Szabó, G. J. Szöllösi, B. Gönci, Zs. Jurányi, D. Selmeczi, and Tamás Vicsek. Phase transition in the collective migration of tissue cells: Experiment and model. *Physical Review E*, 74(6):061908, 2006.

[143] Kang Li, Eric D. Miller, Mei Chen, Takeo Kanade, Lee E. Weiss, and Phil G. Campbell. Cell population tracking and lineage construction with spatiotemporal context. *Medical Image Analysis*, 12(5):546–566, 2008.

[144] George Haller and G. Yuan. Lagrangian coherent structures and mixing in two-dimensional turbulence. *Physica D: Nonlinear Phenomena*, 147:352–370, 2000.

[145] M. L. Falk and J. S. Langer. Dynamics of viscoplastic deformation in amorphous solids. *Physical Review E*, 57(6):7192–7205, 1998.

[146] Lou Kondic, X. Fang, Wolfgang Losert, C. S. O'Hern, and R. P. Behringer. Microstructure evolution during impact on granular matter. *Physical Review E*, 85:011305, 2012.

[147] Douglas H. Kelley and Nicholas T. Ouellette. Separating stretching from folding in fluid mixing. *Nature Physics*, 7(6):477–480, 2011.

[148] Wouter G. Ellenbroek, Martin van Hecke, and Wim van Saarloos. Jammed frictionless disks: Connecting local and global response. *Physical Review E*, 80(6):061307, 2009.

[149] Douglas H. Kelley and Nicholas T. Ouellette. Using particle tracking to measure flow instabilities in an undergraduate laboratory experiment. *American Journal of Physics*, 79(3):267–273, 2011.

[150] Nicholas T. Ouellette, Haitao Xu, and Eberhard Bodenschatz. A quantitative study of three-dimensional Lagrangian particle tracking algorithms. *Experiments in Fluids*, 40(2):301–313, 2006.

[151] Rachel M. Lee, Christina H. Stuelten, Carole A. Parent, and Wolfgang Losert. Collective cell migration over long time scales reveals distinct phenotypes. *Convergent Science Physical Oncology*, 2(2):025001, 2016.

[152] Paolo P. Provenzano, Kevin W. Eliceiri, and Patricia J. Keely. Shining new light on 3D cell motility and the metastatic process. *Trends in Cell Biology*, 19(11):638–648, 2009.

[153] Ian Y. Wong, Sarah Javaid, Elisabeth A. Wong, Sinem Perk, Daniel A. Haber, Mehmet Toner, and Daniel Irimia. Collective and individual migration following the epithelial-mesenchymal transition. *Nature Materials*, 13(11):1063–1071, 2014.

[154] M. Reffay, Laurence Petitjean, S. Coscoy, Erwan Grasland-Mongrain, F. Amblard, Axel Buguin, and Pascal Silberzan. Orientation and Polarity in Collectively Migrating Cell Structures: Statics and Dynamics. *Biophysical Journal*, 100(11):2566–2575, 2011.

[155] Sa Kan Yoo, Pui-ying Lam, Mark R. Eichelberg, Lauren Zasadil, William M. Bement, and Anna Huttenlocher. The role of microtubules in neutrophil polarity and migration in live zebrafish. *Journal of Cell Science*, 125(23):5702–5710, 2012.